Thermal Pumping of Light-Emitting Diodes

by

Dodd Gray

Submitted to the Department of Electrical Engineering and Computer Science
in partial fulfillment of the requirements for the degree of

Master of Engineering in Electrical Engineering and Computer Science

at the

MASSACHUSETTS INSTITUTE OF TECHNOLOGY

August 2011

Author .....
Department of Electrical Engineering and Computer Science
August 22, 2011

Certified by .....
Rajeev Ram
Professor
Thesis Supervisor

Accepted by .....
Prof. Dennis Freeman
Chairman, Masters of Engineering Thesis Committee

Thermal Pumping of Light-Emitting Diodes

by

Dodd Gray

Submitted to the Department of Electrical Engineering and Computer Science
on August 22, 2011, in partial fulfillment of the
requirements for the degree of
Master of Engineering in Electrical Engineering and Computer Science

Abstract

The work presented here is a study of thermally enhanced injection in light-emitting diodes (LEDs). This effect, which we refer to as "thermal pumping", results from Peltier energy exchange from the lattice to charge carriers when current is injected into an LED. For an applied voltage V such that $qV < \langle \hbar\omega \rangle$, where q is the electron charge and $\langle \hbar\omega \rangle$ is the average emitted photon energy, thermal pumping can greatly enhance the wall plug efficiency of an LED. Thermal pumping can even give rise to LED wall plug efficiency greater than one, which corresponds to electroluminescent cooling of the diode lattice. Thermal pumping and electroluminescent cooling will be studied through numerical modeling and experiment. Our results include the first ever experimental demonstration of electroluminescent cooling in an LED. Finally we use the intuition gained from the study of thermal pumping to design an LED for maximized optical power output with 100% wall plug efficiency.

Thesis Supervisor: Rajeev Ram
Title: Professor

Acknowledgments

I owe special thanks to Rajeev Ram, who has been my research advisor for the past two years. I never would have imagined that I could learn as much as I have during my time in his research group. His technical expertise, creativity, wisdom and patience not only made this learning process possible, they also made it very enjoyable.

It would be an understatement to say that Parthi Santhanam was essential to my development as a researcher. His ability to explain complex physics in simple and intuitive terms never ceases to amaze me. His passion for sharing scientific knowledge and understanding is truly inspiring, and his sense of humor ensured that no matter how frustrated or stuck we were, research was always fun. I could not have hoped for a better research partner and friend all rolled up into one.

I cannot thank the Physical Optics and Electronics group enough for creating such a wonderful research environment. Evelyn, Harry, Jason, Joe, Karan, Katey, Kevin, Krishna, Matthew, Reja, Shireen (that's right, alphabetical order), thank you for putting up with my dumb questions and dumb jokes (both of which were ceaseless). I miss working with all of you all already. I hope we can get together again soon.

I would never have gotten here without the support I've received from my friends and family. The list of close friends and family members to whom I owe thanks is far too long to put here, but you know who you are.

Mackenzie, I couldn't have done this without you. Thank you for sticking with me.

Lastly Mom, Dad, Rosie, this one's for you.

Contents

List of Figures

List of Tables

Chapter 1

Introduction

In recent years, light-emitting diodes (LEDs) have entered applications ranging from communications and sensing to consumer goods, and have even begun to penetrate the enormous general-purpose lighting market. LED efficiency is often a major concern for designers of these devices. Thermal management is another. Before an LED is fabricated, simulation tools are used to predict and optimize the electrical and optical characteristics based on material properties, geometry, doping and operating conditions.

One of the most important performance metrics for LEDs is wall-plug efficiency η. Wall-plug efficiency gives the ratio of optical power emitted by an LED to the electrical power it consumes, set by the voltage across and the current through the device [7]:

$$\eta = \frac{L}{IV} \tag{1.1}$$

where L is the total optical output power, V is the applied voltage and I is the current. Generally this ratio is dependent not only on the materials and geometry of an LED, but also on the electrical bias conditions and temperature. The wall-plug efficiency η is determined by the feeding efficiency η_f and the quantum efficiency η_Q:

$$\eta = \eta_f \eta_Q \tag{1.2}$$

Quantum efficiency η_Q compares the rate of electron injection to the rate of photon

emission and feeding efficiency η_f compares the energy carried by each photon emitted from the LED to the electrical work done on each electron passed through the device [7].

$$\eta_Q = \frac{I}{q} \cdot \left[\frac{L}{\langle \hbar\omega \rangle}\right]^{-1} \tag{1.3}$$

$$\eta_f = \frac{\langle \hbar\omega \rangle}{qV} \tag{1.4}$$

where $\langle \hbar\omega \rangle$ is the average photon energy of the output light and q is electron charge. The η values achieved in state-of-the-art LEDs vary widely with the spectrum and brightness required by the applications for which the LEDs are developed. Gallium Nitride- (GaN-) based blue and near ultraviolet LEDs, which are of great interest for general purpose lighting applications, have been demonstrated with $\eta \approx 35\%$ and $\eta_Q \approx 36\%$ at 6Wcm^{-2} optical output and $\eta \approx 25\%$ and $\eta_Q \approx 32\%$ at 35Wcm^{-2} optical output [8]. Deep ultraviolet LEDs on the other hand, which have more niche applications in medicine and manufacturing, have only been demonstrated with $\eta \approx 1\%$ and $\eta_Q \approx 1.2\%$ at 360mWcm^{-2} [9, 10]. Near-Infrared LEDs based on Indium Gallium Arsenide (InGaAs), which are useful for sensing and short range communication, have been demonstrated with $\eta \approx 48\%$ and $\eta_Q \approx 50\%$ at 1.6Wcm^{-2} [11]. Mid-infrared LEDs based on Gallium Antimonide (GaSb) and Indium Arsenide (InAs), which are useful for gas analysis by absorption spectroscopy, have been demonstrated with $\eta \approx 1\%$ and $\eta_Q \approx 1\%$ at 0.3mWcm^{-2} [12]. The notable trend seen across the entire spectrum of LED development is that $\eta \approx \eta_Q$ with $\eta_f \leq 1$. In every case mentioned above η is limited by η_Q as a result of either poor conversion of injected current into photons within the LED or poor extraction of photons from the device. These limits often result from material growth and processing constraints, and improvements to these limits usually result from novel LED geometries, surface treatments and growth techniques.

A fundamentally different approach to improving η in LEDs is to increase η_f. While η_Q has a fundamental limit of 100%, η_f can actually exceed 100% and has no

fundamental limit [13]. This is a result of the fact that the electrical work done per electron in an LED qV can be arbitrarily small, while the average energy of emitted photons $\langle \hbar\omega \rangle$ is set by the band gap energy of the semiconductor in the active region of the LED and thus is approximately fixed. When $qV < \langle \hbar\omega \rangle$ ($\eta_f > 1$), light emission results from thermoelectrically assisted injection of carriers into the active region. More specifically, electrons gain energy from the lattice through Peltier exchange before entering the active region where they lose energy by emitting photons. The photons emitted carry away both the electrical energy qV and the Peltier heat the injected electron absorbed from the lattice [14]. This thermal pumping effect even permits LED operation with output light power exceeding input electrical power, causing net cooling of the device [15]. This is referred to in the literature as electroluminescent cooling [6, 13], electroluminescence refrigeration [16, 17], opto-thermionic cooling [18, 19], and thermo-photonic cooling [20].

In this thesis we will seek to examine thermal pumping of LEDs and electroluminescent cooling through numerical modeling and experiment, and to explore possible applications to LED design. Experimental demonstration of electroluminescent cooling has never before been demonstrated [13], although there are some ongoing efforts to do so [21]. Modeling of these effects in optoelectronic devices is also a new application space for commercial device simulation software.

In Section 1.1 applications of LEDs will be presented. The principle of operation of an LED and a more in-depth explanation of thermal pumping and electroluminescent cooling in LEDs will be presented in Section 1.2. Methods of experimental LED characterization and numerical modeling that will be used to study these effects will be presented in Section 1.3. A summary of Chapter 1 and an overview of this thesis will be presented in Section 1.4.

1.1 Applications of Incoherent Light Generation

Broad spectrum incoherent light is required for a wide range of sensing applications. Useful information about a system or environment can be surmised by collection of

incoherent light and analysis of its intensity, spectrum and direction. Understanding how light interacts with matter through absorption, emission, reflection, fluorescence, etc. allows us to use collected incoherent light to measure quantities like position, temperature, velocity and chemical composition, among other things. The most important and ubiquitous example of sensing with incoherent radiation is sight. Humans and other animals use vision to collect useful information about their environments and even for communication. There are also many man-made systems that sense using incoherent light. These measurement systems are not limited to the visible spectrum; information can be gathered with light of wavelengths ranging twelve orders of magnitude, from angstroms (x-ray absorption imaging) to 100m (HF band radar and radio telescopes).

Light must be generated for a measurement when the incoherent light naturally present in a system is insufficient for gathering useful information. The spectrum and intensity of light generated for measurement should be suited to excite light-matter interactions that are dynamic functions of the quantities to be measured. Thus it is of interest to consider sources of incoherent light and to understand how to control light generation, not just in terms of spectrum and intensity but also spatially and temporally.

1.1.1 Electrical Modulation of Incoherent Sources

For applications related to sensing or communication, the ability to modulate the power of an incoherent light source is beneficial. In general power density of noise present at low frequencies is large in electronic systems with amplification due to flicker or $^1/_f$ noise [5]. Thus incoherent sources that can be modulated at high frequencies are can often improve the signal-to-noise-ratio (SNR) of systems for sensing and communication. Sources of incoherent light which rely on the filtered blackbody radition of a heated element are limited to very slow modulation frequencies by long thermal time constants associated with raising and lowering the temperature of a massive object. On the other hand modulation of incoherent light output from LEDs is limited by relatively short time constants associated with electron injection

and relaxation. Thus LEDs can be modulated at much higher frequencies and have potential for use in sensing and communication in the presence of significant noise. One example of such an application is lock-in absorption spectroscopy, which will be discussed in depth in Chapter 3 of this thesis.

1.2 Light-Emitting Diodes

LEDs are semiconductor devices that emit incoherent radiation when an electrical current is passed through them. This radiation is a result of electron transitions from occupied conduction band states to unoccupied valance band states of the semiconductor that makes up the LED. This process, known as recombination takes place near the interface of a region with a high concentration of electron-accepting impurities (a p-doped region) and a region with a high concentration of electron-donating impurities (an n-doped region). Such an interface is known as a p-n junction. Electrons transitioning from conduction band states to valence band states must release energy approximately equal to the band gap of the semiconductor. Recombination is said to be radiative when this energy is emitted in the form of a photon, and this mechanism is the basis of light generation in LEDs. This process is depicted in Figure 1-1.

LEDs are often made up of several semiconductor layers with varied band gap energies and doping levels. One purpose of these layers is to confine conduction band electrons to a region where they are likely to encounter an unoccupied valence band state (a hole) and undergo radiative recombination. This confinement region where light is generated is known as the active region of the LED.

The energy of each photon emitted as a result of radiative recombination in an LED is associated with a momentum-conserving electronic transition near the band-edge of the semiconductor in the active region. The energy of each photon is approximately equal to the active region band gap energy. As a result, the incoherent light emitted by an LED falls in a relatively narrow band of wavelengths near the wavelength that corresponds to the band gap energy. In general the bandwidth of

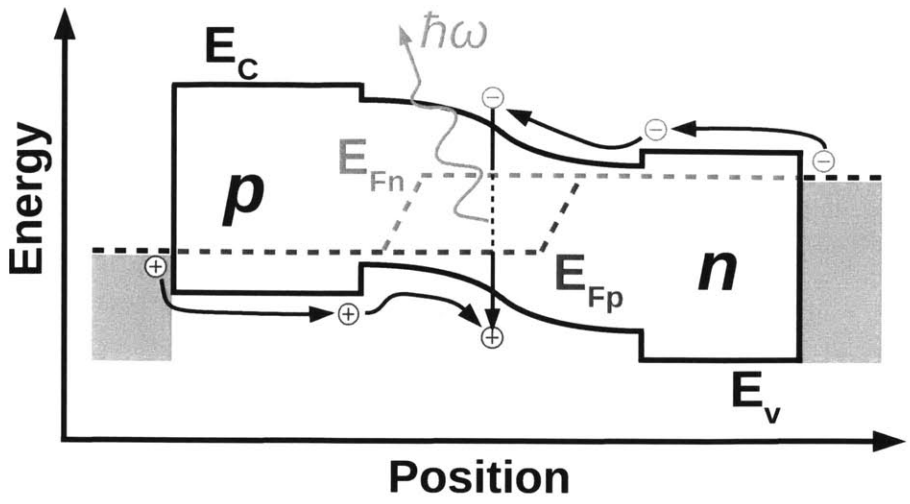

Figure 1-1: Cartoon depiction of an electron and hole being injected into the active region of an LED where they recombine to emit a photon with energy $\hbar\omega$. The conduction band state occupied by an electron is represented by the blue circle with "-" inside to denote negative charge. The unoccupied valence band state (the hole) is represented by a blue circle with a "+" to indicate its apparent positive charge. E_C and E_V denote the conduction band edge and valence band edge energies respectively, which are the upper and lower boundaries of the energy band gap in which electrons in a semiconductor cannot exist. E_Fn and E_Fp denote the Fermi energies of electrons and holes respectively, above which the probability of occupancy of a given state is less than 50%. The (p) and (n) labels indicate regions rich with electron-accepting and electron-donating impurities respectively. The center region has a smaller band gap than the two outer regions, indicating a different material composition. The gray regions on either side of the junction indicate metal contacts which do not have a band gap.

light associated with radiative electron-hole recombination corresponds to a spread in photon energy on the order of k_BT, where k_B is the Boltzmann constant and T is the temperature of the active region in Kelvin.

1.2.1 LED Quantum Efficiency

The quantum efficiency η_Q of an LED can be subdivided into two consituent efficiencies, the internal quantum efficiency (IQE) η_{IQE} and the extraction efficiency $\eta_{extraction}$. The following discussion of these efficiencies and what determines them will closely follow Chapters 2 and 3 of *Light Emitting Diodes* by Schubert [7].

$$\eta_Q = \eta_{IQE}\eta_{extraction} \tag{1.5}$$

The IQE η_{IQE} is defined as the ratio of the number of photons leaving the active region of an LED per second to the total number of electrons that are injected into the device per second. Extraction efficiency, $\eta_{extraction}$, is the ratio of the number of photons leaving the active region per second to the number of photons emitted from the LED per second. To consider η_{IQE} we must further subdivide η_{IQE} into two more efficiencies, the recombination efficiency η_{rec} and the efficiency of photon escape from the active region η_{act}. The recombination efficiency η_{rec} is defined as the ratio of the rate of radiative electron-hole recombination in the active region to the total rate of electron-hole recombination in the active region.

LEDs are usually modeled as having three types of recombination in the bulk of the active region. These are Shockley-Read-Hall (SRH), bimolecular and Auger recombination. SRH recombination occurs an electron (hole) encounters an occupied (occupied) localized state inside the energy band gap associated with an impurity in the semiconductor crystal (known as a 'trap state') and 'falls' into it. Bimolecular recombination occurs when an electron encounters a hole and they recombine by emitting a photon. Auger recombination occurs when carrier concentrations are so high that electrons interact with electrons or holes interact with holes. In an Auger process two or more charge carriers of the same type scatter off of one another, causing at least one to undergo an interband transition after transfering momentum to the other(s) [22]. Trap-based SRH recombination can also happen at material interfaces. This is known as surface SRH recombination. In most cases bimolecular recombination is the only one of these types that causes photon emission. The rates of these three types of recombination R_{SRH}, R_{bimol} and R_{Aug} in $cm^{-3}s^{-1}$ and $R_{SRH,surf}$ in $cm^{-2}s^{-1}$ can be calculated as follows [7]:

$$R_{SRH} = \frac{np - n_{\mathrm{i}}^2}{\tau_{\mathrm{SRH,h,0}}\left(\frac{T}{300}\right)^{-\frac{3}{2}}(n + n_{\mathrm{i}}) + \tau_{\mathrm{SRH,e,0}}\left(\frac{T}{300}\right)^{-\frac{3}{2}}} \tag{1.6}$$

$$R_{bimol} = B_0\left(\frac{T}{300}\right)^{-\frac{3}{2}}\left(\frac{E_{\mathrm{gap}}}{E_{\mathrm{gap,0}}}\right)^2(np - n_{\mathrm{i}}^2) \tag{1.7}$$

$$R_{Aug} = C(n + p)(np - n_{\mathrm{i}}^2) \tag{1.8}$$

$$R_{SRH,surf} = = \frac{np - n_{\mathrm{i}}^2}{v_{\mathrm{surf}}(n + p + 2n_{\mathrm{i}})} \tag{1.9}$$

where n and p are the electron and hole concentrations in cm^{-3}, n_i is the equilibrium concentration of electrons and holes in an undoped material T is the lattice temperature, $\tau_{SRH,i,0}$ is an SRH recombination lifetime in seconds that encapsulates the density of trap states and the strength of their interactions with carriers, B_0 is a bimolecular recombination coefficient describing the strength of electron-hole interactions at 300°K, E_{gap} is the band gap energy, $E_{\mathrm{gap,0}}$ is the band gap energy at 300°K, C is a coefficient that encapsulates the many-body physics of Auger interactions in a given material and v_{surf} is a surface recombination velocity that encapsulates the density of traps on a surface and the strength of their interactions with electrons and holes to relate electron and hole densities to surface SRH rates. We assume both carrier populations are in the Boltzmann limit and calculate the intrinsic carrier concentration n_i as [5]

$$n_{\mathrm{i}} = \sqrt{N_{\mathrm{C}}N_{\mathrm{V}}}e^{\frac{-E_{\mathrm{gap}}}{k_{\mathrm{B}}T}} \tag{1.10}$$

where N_{C} and N_{V} are the densities of states near the conduction and valence band edges, respectively. We note that N_{C}, N_{V} and other mentioned material parameters such as C have polynomial temperature dependencies, but that the exponential temperature dependence of n_{i} dominates the temperature dependences of all of these recombination rates (and thus of η_{rec}). We can now calculate η_{rec}:

$$\eta_{rec} = \frac{\int_{V_{act}} R_{bimol}dV}{\int_{V_{dev}}(R_{SRH} + R_{bimol} + R_{Aug}dV + \int_A R_{SRH,surf}dA} \tag{1.11}$$

where the integral in the numerator is over the volume of the active region (V_{act}) and the integrals in the denominator are over the entire volume of the device (V_{dev}) and total surface area A relevant to surface SRH recombination.

Comparing the descriptions of the various recombination mechanisms and the equations describing their rates, we see a correspondence between the number of carriers involved in a process and the power law dependence of the rate of that process on carrier concentrations. SRH processes that only involve one carrier and a trap are approximately proportional to $n+p$. Bimolecular processes which involve one electron and one hole are proportional to np. Auger processes which involve two electrons and one hole or two holes and one electron are proportional to n^2p or np^2 respectively. We note that higher order Auger processes are not considered here. With this intuition we can infer that at low or highly asymmetric carrier concentrations SRH recombination should dominate, that bimolecular processes should become more important if both carrier concentrations are significantly out of equalibrium, and that Auger processes begin to dominate if the carrier concentrations are increased further.

To properly calculate η_{IQE} we must consider the case in which an emitted photon is re-absorbed before escaping the active region, leading to another electron-hole pair that subsequently recombine to emit another photon that may escape the active region. We also must consider that this sequence of events, known as photon recycling, can happen arbitrarily many times [13]. Thus we calculate η_{IQE}:

$$\begin{aligned}
\eta_{IQE} &= \eta_{rec}\eta_{act} + \eta_{rec}(1-\eta_{act})\eta_{rec}\eta_{act} + \eta_{rec}[(1-\eta_{act})\eta_{rec}]^2\eta_{act} + \dots \\
&= \eta_{rec}\eta_{act}\sum_{n=0}^{\infty}[(1-\eta_{act})\eta_{rec}]^n \\
&= \frac{\eta_{rec}\eta_{act}}{1-(1-\eta_{act})\eta_{rec}}
\end{aligned} \tag{1.12}$$

Considering Equations 1.2, 1.5 and 1.12 we can write η as

$$\eta = \frac{\eta_f\eta_{extraction}\eta_{rec}\eta_{act}}{1-(1-\eta_{act})\eta_{rec}} \tag{1.13}$$

We note that this includes the assumption that emitted photons that are absorbed outside of the active region do not contribute electron-hole pairs that could contribute to subsequent light emission. If non-radiative recombination dominates in the active region ($\eta_{rec} \ll 1$) or almost all emitted photons escape the active region ($\eta_{act} \approx 1$) then $\eta_{rec}(1 - \eta_{act}) \ll 1$ and we can write

$$\eta \approx \eta_f \eta_{extraction} \eta_{rec} \eta_{act} \tag{1.14}$$

All of these efficiencies can be predicted directly from simulations in the CAD modeling software discussed below. Wall-plug efficiency η and quantum efficiency η_Q can be experimentally verified using data from the electrical and optical characterization techniques. Internal quantum efficiency η_{IQE} can be directly measured using laser-induced photoluminescence in an unbiased LED[23]. In some cases the extraction efficiency of LED geometries can be directly measured using photo-excitation combined with photodetection[24]. In other cases $\eta_{extraction}$ can only be estimated using material absorption parameters and LED geometry. Established analytical models exist for this technique [25]. Many modern LEDs emit from quantum-confined active regions with thicknesses much smaller than the wavelength of the emitted photons [26, 27], and thus $\eta_{act} \approx 1$. Driven by the goal of entering the general purpose lighting market, a great deal of reasearch has been done (and is ongoing) to improve the achievable values of $\eta_{extraction}$ and η_{rec} in GaN-based LEDs [26]. As a result the highest reported $\eta_{extraction}$ and η_{IQE} values are usually found in these devices. GaN-based LEDs emitting in the visible and UV spectra have been demonstrated with η_{IQE} values above 75% and $\eta_{extraction}$ values above 80%[27, 28, 23].

1.2.2 Thermal Pumping and Electroluminescent Cooling in LEDs

The quantum efficiency η_Q of an LED and of its constituent efficiencies discussed above have a maximum value of 1. The feeding efficiency η_f on the other hand does not. For this reason, from a thermodynamics standpoint η_f is more accurately

described as a coefficient of performance for a heat pump. When the voltage bias V across an LED is small enough that $qV < \langle \hbar\omega \rangle$, then $\eta_f > 1$. It is easy to see that if $\eta_f > \eta_{EQE}^{-1}$ then $\eta > 1$. In this situation the coefficient of performance of an LED has overcome all inefficiency in the device and the LED operates as a heat pump. Put another way, when wall plug efficiency η exceeds unity then conservation of energy requires electrically driven light emission to be accompanied by net absorption of heat from the ambient environment.

The study of electroluminescent cooling stretches back six decades. As early as 1951, Lehovec et al. speculated on the role of thermo-electric heat exchange in SiC LEDs [29]. The authors were motivated by their observation of light emission with average photon energy $\langle \hbar\omega \rangle$ on the order of the electrical input energy per electron, given by the product of the electrons charge q and the bias voltage V. Then beginning with Jan Tauc in 1957 [14], a body of literature theoretically establishing the thermodynamic consistency of electro-luminescent cooling and exploring its limits began to emerge [15]. In fact, although net cooling had not been experimentally demonstrated, in 1959 a US Patent was granted for a refrigeration device based on the principle [30].

In 1964, Dousmanis et al. demonstrated that a GaAs diode could produce electroluminescence with an average photon energy 3% greater than qV [31]. Still, net cooling was not achieved due to non-radiative recombination [32] and the authors concluded that the fraction of current resulting in escaping photons, typically called the external quantum efficiency or simply quantum efficiency η_Q, must be large to observe net cooling.

Then in 1985, Berdahl derived [32] that the radiant heat pumping power of semiconductor diodes decreased exponentially with the ratio of the diode materials bandgap E_{gap} to the thermal energy $k_B T$.

In the last decade, several modeling and design efforts have aimed to raise η_Q toward unity by maximizing the fraction of recombination that is radiative [6, 13, 19] and employing photon recycling to improve photon extraction [6, 13, 16]. Efforts to observe electroluminescent cooling with η near 100% continue to be active [20].

Since η_f clearly diverges as the applied voltage approaches zero, it is of interest to consider the value of η_Q in the same limit. For a diode in the low-bias limit we assume that all current density results from bimolecular and bulk SRH recombination in the active region of the device [5] and that the electron and hole concentrations n and p approach an equilibrium value of n_i (if the active region is not doped). Auger recombination is neglected because we assume that carrier concentrations near equilibrium are too small for it to be significant. We also assume that $\eta_{extraction}$ is independent of voltage bias and that $\eta_{rec}(1-\eta_{act}) \ll 1$ so that photon recycling is insignificant. Using Equations 1.5, 1.6, 1.7, 1.11, 1.10 and 1.12, η_Q is shown to approach a finite value as the applied voltage V approaches 0:

$$\begin{aligned}
\lim_{V\to 0}\eta_Q &= \frac{\eta_{extraction}R_{bimol}}{R_{SRH}+R_{bimol}} \\
&= \frac{\eta_{extraction}\eta_{act}B}{[4n_i\tau_{SRH}]^{-1}+\eta_{act}B} \\
&= \frac{4\eta_{extraction}\eta_{act}B\tau_{SRH}n_i}{1+4\eta_{act}B\tau_{SRH}n_i} \\
&\approx 4\eta_{extraction}\eta_{act}B\tau_{SRH}n_i \quad (4\eta_{act}B\tau_{SRH}n_i \ll 1) \\
&= 4\eta_{extraction}\eta_{act}B_0\tau_{SRH}\sqrt{N_VN_C}e^{\frac{-E_{gap}}{2k_BT}} \qquad (1.15)
\end{aligned}$$

Note that we have done this calculation using B_0 to calculate the bimolecular recombination rate which is only valid at 300°K, but that the temperature dependence of $\lim_{V\to 0}\eta_Q$ is dominated by the exponential dependence of n_i. Since η_Q approaches a finite value at zero bias while η_f diverges, η must also diverge as the applied voltage approaches zero [13]. Note that this indicates that EL cooling occurs in all LEDs for a small enough applied voltage. Under the same assumptions we can readily approximate the voltage, current density and emitted light power density in this limit when $\eta = 1$. The voltage $V_{\eta=1}$ is approximated by setting $\eta_f = \eta_Q^{-1}$:

$$V_{\eta=1} = \frac{\langle\hbar\omega\rangle}{q}\eta_Q \tag{1.16}$$

$$\approx \frac{\langle\hbar\omega\rangle 4\eta_{extraction}B_0\tau_{SRH}\sqrt{N_V N_C}e^{\frac{-E_{gap}}{2k_BT}}}{q} \tag{1.17}$$

Current density $J_{\eta=1}$ is approximated by

$$\begin{aligned} J_{\eta=1} &\approx qtR_{SRH} \\ &\approx \frac{qt}{4n_i\tau_{SRH}}(np - n_i^2) \\ &= \frac{qt}{4n_i\tau_{SRH}}n_i^2(e^{\frac{qV}{k_BT}} - 1) \\ &= \frac{qt}{4n_i\tau_{SRH}}N_V N_C e^{\frac{-E_{gap}}{k_BT}}(e^{\frac{qV_{\eta=1}}{k_BT}} - 1) \\ &\approx \frac{qW}{4n_i\tau_{SRH}}N_V N_C e^{\frac{-E_{gap}}{k_BT}}(\frac{qV_{\eta=1}}{k_BT}) \\ &= \frac{\langle\hbar\omega\rangle}{k_BT}\eta_{extraction}qtB_0(N_V N_C e^{\frac{-E_{gap}}{k_BT}})^{\frac{3}{2}} \end{aligned} \tag{1.18}$$

where t is the thickness of the active region and non-radiative SRH recombination is assumed to dominate and occur uniformly over this width. Note that we have taken the Taylor approximation for the exponential dependence on applied voltage under the assumption that $V_{\eta=1}$ is on the order of k_BT. Finally, light power density $L_{\eta=1}$ is calculated to be

$$\begin{aligned} L_{\eta=1} &\approx \eta_{extraction}\langle\hbar\omega\rangle tR_{bimol} \\ &= \eta_{extraction}\langle\hbar\omega\rangle tB_0 N_V N_C e^{\frac{-E_{gap}}{k_BT}}(e^{\frac{qV_{\eta=1}}{k_BT}} - 1) \\ &\approx \eta_{extraction}\langle\hbar\omega\rangle tB_0 N_V N_C e^{\frac{-E_{gap}}{k_BT}}(\frac{qV_{\eta=1}}{k_BT}) \\ &= \frac{\eta_{extraction}^2\langle\hbar\omega\rangle^2 B_0^2 t(N_V N_C e^{\frac{-E_{gap}}{k_BT}})^{\frac{3}{2}}}{k_BT} \end{aligned} \tag{1.19}$$

Examining Equation 1.19 we see that $L_{\eta=1}$ decreases exponentially as a function of the ratio of band gap to thermal energy, $\frac{3E_{gap}}{2k_BT}$. This dependence results from the proportionality of $L_{\eta=1}$ to the cube of the intrinsic carrier concentration n_i. We also see from Equation 1.15 that the low bias minimum IQE is proportional to n_i and thus also increases exponentially as the ratio $\frac{E_g}{k_BT}$ is reduced. These relationships indicate that the effect of thermal pumping should be most apparent in LEDs with small active region band gaps at high temperature.

Thermal pumping of an LED can also be described in terms of Peltier heat transfer at a p-n junction. Following Pipe's description of Peltier heat transfer in a p-n diode in Section 2.5.2 of [33], we can calculate the light power density pumped out of the lattice and into the optical field L_{pump} in terms of $\Pi_{p,h}$ and $\Pi_{n,e}$, which are the Peltier coefficients of the holes on the p-doped side and electrons on the n-doped side of the LED. These Peltier coefficients are just averages of the energies per unit charge of the majority carriers on either side of the diode weighted by the relative contribution of the carriers to conduction as a function of energy [33, 34]. We find that for an applied current density J

$$L_{pump} = \eta_Q J(\Pi_{p,h} + \Pi_{n,e}) \tag{1.20}$$

and that total light emission L should be the sum of L_{pump} and the emitted light due to electrical work qV, L_{work}

$$\begin{aligned} L &= L_{work} + L_{pump} \\ &= \eta_Q J(\Pi_{p,h} + \Pi_{n,e} + V) \qquad (1.21) \\ &= \eta_Q J\langle\hbar\omega\rangle \qquad (1.22) \end{aligned}$$

We note that Equation 1.22 is simply a restatement of our previous definition of η_Q and that Equations 1.20 and 1.21 are valid only for a p-n homojunction in which

all recombination occurs away from the contacts. Although most LEDs incorporate heterojunctions, we can still use these equations to get an intution for how Peltier heat contributes to light emission from an LED. In Chapter 2 we will numerically model thermal pumping in an LED without making these approximations.

1.3 Tools for Studying LEDs

In this thesis thermal pumping and electroluminescent cooling in LEDs will be studied with numerical modeling and experiment. Numerical modeling should give an intuition for microscopic charge and energy transport dynamics and their connection to easily measured device characteristics, while experimental LED characterization will be useful for comparison with modeling results and validation of the intuition they give us.

LEDs can be experimentally characterized using a few simple techniques. The electrical characteristics can be measured using a power supply and multimeter or a parameter analyzer. If an LED is packaged with a lens so that the emission pattern is partially collimated, then placing the LED in close proximity to a relatively large area photodetector can allow for free-space light power measurement with reasonable light collection efficiency. If an LED emits light over a large solid angle then an integrating sphere can be used to collect and analyze the power and spectrum of light output from an LED[35]. These measurements can be used to determine the relationship between light output power and voltage (L-V) or current (L-I) bias, and also to determine the wall-plug efficiency and EQE of the device. If the light power becomes small compared to noise measured by the detector, it is also possible to modulate the light signal and perform a phase and frequency sensitive measurement to greatly improve signal to noise ratio. This technique, known as lock-in measurement, is explained in Chapter 3.

Designers of solid state electronic and optoelectronic devices such as diodes, transistors, LEDs and lasers in industry and academia use technology computer aided design (TCAD) finite-element modeling tools such as Silvaco ATLAS^{TM}, Crosslight

APSYS^{TM}and Synopsis Sentaurus^{TM}to simulate the electrical, optical and thermal characteristics of their devices under specified bias and boundary conditions[36, 37]. In a finite-element model a device is broken in many small elements, partial differential equations describing relevant physics are approximated as difference equations, boundary conditions are specified and numerical steady-state solutions to the difference equations are solved for iteratively. These software packages are useful both for gaining a general intuition for the physical processes that are important to device operation and for fine tuning and optimizing a device.

In this thesis we will study charge and energy transport phenomena in an LED using Synopsis Sentaurus^{TM}TCAD. While Sentaurus is most commonly used to model complimentary-metal-oxide-semiconductor (CMOS) electronics in 1, 2 or 3 dimensions, it is a very general purpose tool for modeling charge and energy transport in semiconductor devices. Sentaurus even has a host of tools for modeling light generation, propagation and absorption in optoelectronic devices such as LEDs, lasers and photodiodes [38]. In particular we have chosen to use Sentaurus for this investigation because it includes the Stratton model for hydrodynamic charge and energy transport model in semiconductors [38, 39, 40], which accounts for the energy flux through the electrons, holes and lattice separately. This will be useful for modeling Peltier exchange in an LED.

1.3.1 Hydrodynamic Charge and Energy Transport

A hydrodynamic charge and energy tranport model includes the k^0, k^1 and k^2 moments of the Boltzmann transport equation to account for tranfer and conservation of charge, momentum and energy respectively [39]. Time-independent versions of these balance equations are solved in this framework to model steady-state behavior. The following discussion of the hydrodynamic model follows Chapter 5 of *Fundamentals of Carrier Transport* by Lundstrom [39] as well as the *Sentaurus User Guide* [38].

To begin with we define the electron, hole and lattice temperatures as they are used in this model. The electron and hole temperatures T_e and T_h are defined using the average thermal kinetic energy of the carriers w_e and w_h, assuming that each

population is a non-interacting gas in three dimensions

$$w_e = \frac{3}{2}k_B T_e \tag{1.23}$$

$$w_h = \frac{3}{2}k_B T_h \tag{1.24}$$

while the lattice temperature T_l describes the thermal occupation of the phonon modes in the lattice that determine its heat capacity:

$$W_l = c_l T_l \tag{1.25}$$

To begin with, electrostatics are modeled with Poisson's Equation

$$\nabla^2 \phi = \frac{\rho}{\epsilon} = \frac{-q}{\epsilon}(p - n + N_D - N_A), \tag{1.26}$$

where ϕ is the electrostatic potential, q is the electron charge magnitude, ϵ is the static dielectric constant of the semiconductor, p and n are the hole and electron densities and N_D and N_A are ionized donor and acceptor densities. The continuity equations describe charge carrier flux into and out of a differential volume of semiconductor:

$$\nabla \cdot \vec{J_e} = \frac{q}{\epsilon} R_{net} \tag{1.27}$$

$$\nabla \cdot \vec{J_h} = -\frac{q}{\epsilon} R_{net} \tag{1.28}$$

where J_e and J_h are the electron and hole current densities respectively and R_{net} is the net recombination rate in $\mathrm{cm^{-3}s^{-1}}$ (this term is negative for net generation). The momentum balance equations gives us the electron and hole current densities in separate drift, density-gradient-diffusion and temperature-gradient-diffusion components:

$$\vec{J_e} = -q\mu_e(n\nabla E_C + kT_e\nabla n + \lambda_e k_B n\nabla T_e) \quad (1.29)$$

$$\vec{J_h} = -q\mu_h(p\nabla E_V + kT_p\nabla p + \lambda_h k_B n\nabla T_h) \quad (1.30)$$

where μ_e and μ_h are the electron and hole mobilities, E_C and E_V are the conduction and valence band edge energies, and λ_e and λ_h are correction factors accounting for energy flux through degenerate carrier populations. According to Fermi-Dirac statistics [41]

$$\lambda_e = \frac{F_{\frac{1}{2}}\left(\frac{E_C - E_{Fn}}{k_B T_e}\right)}{F_{-\frac{1}{2}}\left(\frac{E_C - E_{Fn}}{k_B T_e}\right)} \quad (1.31)$$

$$\lambda_h = \frac{F_{\frac{1}{2}}\left(\frac{E_{Fp} - E_V}{k_B T_h}\right)}{F_{-\frac{1}{2}}\left(\frac{E_{Fp} - E_V}{k_B T_h}\right)} \quad (1.32)$$

where E_{Fn} and E_{Fp} are the electron and hole quasi-Fermi energies and F_i represents a Fermi integral of order i. The energy balance equations describe the carrier-mediated energy flux into and out of a differential volume of the semiconductor:

$$\nabla \cdot \vec{S_e} = \vec{J_e} \cdot \nabla E_C - \frac{3}{2}k_B\left[T_e R_{net} - \frac{T_e - T_l}{\tau_e}\right] \quad (1.33)$$

$$\nabla \cdot \vec{S_h} = \vec{J_h} \cdot \nabla E_V - \frac{3}{2}k_B\left[T_h R_{net} - \frac{T_h - T_l}{\tau_h}\right] \quad (1.34)$$

where τ_e and tau_h are energy relaxation times associated with the electrons and holes respectively. We note that these equations encode Peltier heat exchange between the lattice and the charge carriers. As electrons flow along a positive gradient in E_C or holes flow along a negative gradient in E_V energy, a negative acomponent is added to the divergence of their energy fluxes denoting a decrease in average carrier energy. This leads to a steady state temperature lower than that of the lattice and thus

net energy absportion from the lattice, accounted for by the energy relaxation term on the right hand side of 1.33 and 1.34. Equations 1.33 and 1.34 are accompanied by the energy balance equation for the lattice, which acocunts for heating due to electron-phonon scattering and recombination:

$$\nabla \cdot \vec{S}_l = \left[\frac{3}{2}k_B(T_e + T_h) + E_{gap}\right] R_{net} + \frac{3}{2}k_B \left[\frac{T_e - T_l}{\tau_e} + \frac{T_h - T_l}{\tau_h}\right] \tag{1.35}$$

We note here that Equations 1.33, 1.34 and 1.35 are only valid in the Boltzmann limit, and that Sentaurus does not include a correction for the average kinetic energy of degenerate charge carriers according to Fermi-Dirac statistics [41]. The electron- and hole-mediated energy fluxes are calculated according to the Stratton model for hydrodynamic flow [40]:

$$\vec{S}_e = -\frac{5r\lambda_e}{2}\left[\frac{k_B T_e}{q}\vec{J}_e + \frac{k_B^2 n \mu_e T_e}{q}\nabla T_e\right] \tag{1.36}$$

$$\vec{S}_h = \frac{5r\lambda_h}{2}\left[\frac{k_B T_h}{q}\vec{J}_h - \frac{k_B^2 p \mu_h T_h}{q}\nabla T_h\right] \tag{1.37}$$

where r is a material parameter that encodes the power-law dependence of the scattering rate $\frac{1}{\tau}$ on carrier energy E [34, 39]:

$$\frac{1}{\tau_i} \sim E^{\frac{5}{2}(1-r_i)} \tag{1.38}$$

Finally, energy flux through the lattice is described the the familiar heat equation

$$\vec{S}_l = -\kappa \nabla T_l \tag{1.39}$$

where κ is the lattice thermal conductivity.

1.4 Chapter Summary and Thesis Outline

In Section 1 we defined the wall plug efficiency η of an LED and the phenomenon of electroluminescent cooling. Motivation for studying the effects of thermal pumping in LEDs and a brief overview of previous work on the subject was given. In Section 1.1 various applications of incoherent light sources were discussed. In Section 1.2 we discussed the microscopic physical processes that give rise to light emission in LEDs, how they determine device efficiency and how they can give rise to thermal pumping and electroluminescent cooling. Finally in Section 1.3 we discussed the experimental and numerical modeling techniques that will be used in this thesis to investigate thermal pumping and electroluminescent cooling in LEDs in the following Chapters.

Chapter 2 will describe the modeling of thermoelectric pumping effects in a model system. The model will be built step by step and simulated device characteristics will be presented compared with experiment. Predictions of EL cooling in these simulations will be highlighted and discussed.

In Chapter 3 a method based on lock-in amplification for precisely measuring the electrical and optical characteristics of an LED will be presented. The noise limitations of our measurement system will be given. Experimental results including evidence of EL cooling and demonstration of an efficient radiation source for mid-IR spectroscopy systems will be presented and again compared with Sentaurus modeling results.

Chapter 4 will describe the design and modeling of thermally-pumped LEDs. Devices optimized for high-temperature, high-power operation and devices optimized for room-temperature, low-power operation will be considered. A new high-temperature packaging scheme for LEDs will be presented along with predictions of the power efficiencies that could be achieved by a thermally-pumped LED packaged in this way. Potential applications of this technology will be discussed.

In Chapter 5 a summary of this work will be presented along with conclusions and suggestions for future work on the subject will be given.

Chapter 2

LED Modeling and Characterization

A real world model system is needed to study thermal pumping and electroluminescent cooling in LEDs. It is desirable that the system is accessible for both simulation and experimentation. Sufficient information about the materials and structure of the device is required for the development of a reasonable numerical model. Experimental study of the thermal pumping of LEDs involves characterization of electrical and optical device properties such as voltage (V), current (I) and light power (L), as functions of the diode temperature (T). As discussed in Chapter 1, these macroscopic device characteristics can be predicted by modeling microscopic carrier and energy transport dynamics with Sentaurus. Comparison of simulated and experimentally measured device characteristics can be used to test the validity of the model.

In Section 2.1 a prototypical system for studying thermal pumping in LEDs will be introduced. In Section 2.2 a numerical model for charge and energy transport in an LED will be built up step by step using Sentaurus Device. In Section 2.3 simulated L-I-V-T characteristics for our LED will be given and an apparatus for experimentally measuring these characteristics will be introduced. Results of experimental device characterization with this apparatus will be given and compared with simulation results. In Section 2.4 the possibility of demonstrating improved LED efficiency due to thermal pumping and the challenges involved will be discussed. Conclusions and

a summary of this Chapter will be given in Section 2.5.

2.1 A Prototypical System

As discussed in Chapter 1, the theory describing EL cooling suggests that the prominence of the effect decreases exponentially with the ratio of the band gap energy of the material in the active region to the thermal energy in the active region $\frac{E_g}{k_B T}$. Thus an LED with a small active region band gap (corresponding to long wavelength electroluminescence) that can survive to high temperature would be ideal for studying thermal pumping in LEDs. In most conventional applications, LEDs are operated at high bias where device performance deteriorates as temperature increases, and thus are not packaged to withstand high temperatures. This thesis will focus on the study of thermal pumping in a GaSb/$In_{.15}Ga_{.85}As_{.13}Sb_{.87}$ double-heterojunction *p-i-n* LED [3]. The device consists of a 2.5-4μ thick, "nominally undoped"[2] layer of GaSb/$In_{.15}Ga_{.85}As_{.13}Sb_{.87}$ and a 3-5μ thick *p+*-GaSb layer grown on an *n*-GaSb substrate. The doping levels of the *p+*-GaSb and *n*-GaSb were $N_A = .5 - 1 \cdot 10^{18}$ cm^{-3} and $N_D = 4 \cdot 10^{17}$ cm^{-3}, respectively. The LED is similar to those described in [2] and [1]. These publications give information about the device structure, which is useful for modeling. The LED was grown by liquid-phase epitaxy (LPE) on an n-GaSb substrate, etched into a mesa structure 280μm in diameter [42], metalized with contacts, flip-chip bonded to a semi-insulating Si mounting pad, and packaged with a Si lens inside a threaded M5x0.5 can. Note that the uncertainty in the epitaxial layer thicknesses and doping levels are a result of the uncertainties associated with liquid phase growth. The LED is a commercial device distributed by Ioffe LED, Ltd., a company affiliated with the Mid-IR Diode Opto-pair Group (MIRDOG) at the Ioffe Physico-Technical Institute in St. Petersburg, Russia. The part number of the device is LED21Sr. Figures 2-1, 2-2 and 2-3 are included from [1], [2] and [3] to give an idea of the LED geometry.

Before we can study thermal pumping in the LED21Sr, we must first develop a general model for charge and energy transport through an LED that can self-

consistently account for the the Peltier exchange that should give rise to thermal pumping effects and ultimately electroluminescent cooling. This task is undertaken in Section 2.2.

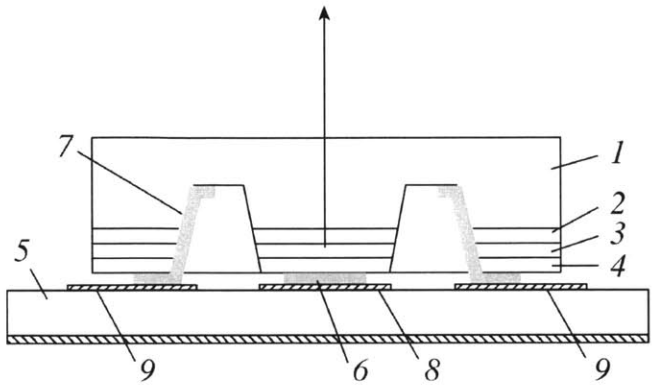

Figure 2-1: Diagram showing the flip-chip mesa structure used by Ioffe LED, Ltd. for the LED21Sr and other devices.. The labsls show (1) the n-GaSb substrate, (2) the n-GaInAsSb layer, (3) the p-GaInAsSb layer, (4) the p+-GaSb layer, (5) the silicon carrier, (6) the anode contact, and (7) the U-shaped cathode contact. (8) and (9) are the contact pads on the silicon carrier[1]. Note that although separate n- and p-GaInAsSb layers are labeled in this Figure, these layers were not intentionally doped and the density of dopants in this region is not known.

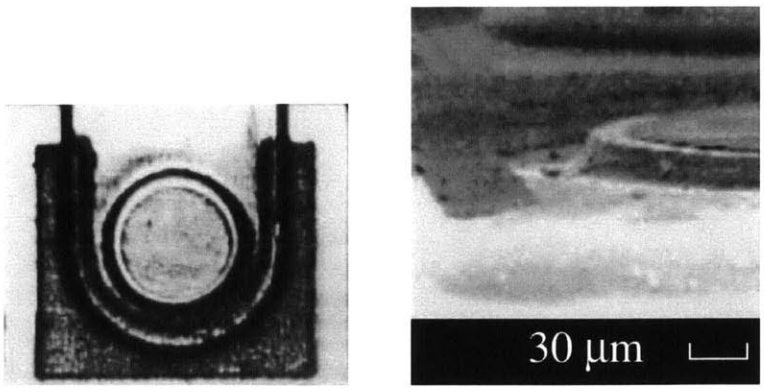

(a) (b)

Figure 2-2: Photographs showing the mesa structure of the LED21Sr from the top (a) and side (b) (from [2]).

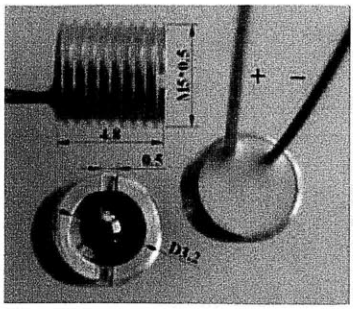

Figure 2-3: Photograph of the packaged LED21Sr (from [3]).

2.2 Modeling Peltier Heat Transfer

The model for thermal pumping in LEDs will be built in four steps. First, charge and energy transfer will be modeled in the simplest possible device, a resistor. Next, a *p-n* junction in which almost all minority carriers recombine before diffusing to the contacts will be modeled. A *p-i-n* junction in which most minority carriers diffuse to the contacts before recombining will be modeled next to demonstrate the importance of boundary conditions and energy transfer at contacts. Finally, a double-heterojunction *p-i-n* diode resembling the LED discussed in the previous Section will be modeled. This step-by-step approach should emphasize the importance of various attributes of LEDs to charge and energy transport and prepare us to study a real system through numerical simulation.

Because we are building towards a model for a device in the InAs/GaSb material system, the devices modeled in this Section will modeled in the same material system for the sake of simplicity and continuity. The first three devices will all be modeled as GaSb, and the fourth device will be modeled as GaSb and $In_{.15}Ga_{.85}As_{.13}Sb_{.87}$ (the alloy composition given for the active region of the LEDs discussed in the previous Section). The material parameters used for these two materials and their sources are given in Table 2.1 and equations for which these parameters are most relevant are given in Table 2.2.

Material Parameter	Symbol	$Ga_{.85}In_{.15}As_{.13}Sb_{.87}$ value at 300K	GaSb value at 300K
Band gap	$E_{gap,0}$	0.583 eV[43]	0.726 eV[44]
Temperature dependent band gap narrowing parameter	α	$3.78{\cdot}10^{-4}$ eV·K^{-1} [44]	$3.78{\cdot}10^{-4}$ eV·K^{-1} [44]
N-type band gap narrowing parameters	A_N	n/a	$13.6{\cdot}10^{-9}$ eV·cm[45]
	B_N	n/a	$1.66{\cdot}10^{-7}$ eV·cm$^{\frac{4}{3}}$[45]
	C_N	n/a	$1.19{\cdot}10^{-10}$ eV·cm$^{\frac{2}{3}}$[45]
P-type band gap narrowing parameters	A_P	n/a	$8.07{\cdot}10^{-9}$ eV·cm[45]
	B_P	n/a	$2.8{\cdot}10^{-7}$ eV·cm$^{\frac{4}{3}}$[45]
	C_P	n/a	$4.12{\cdot}10^{-12}$ eV·cm$^{\frac{2}{3}}$[45]
Electron SRH lifetime	$\tau_{SRH,e,0}$	95 ns†	10 ns[46]
Hole SRH lifetime	$\tau_{SRH,h,0}$	95 ns†	600 ns[46]
Surface SRH recombination velocity	v_{surf}	1900 cm·s^{-1} [47]	
Radiative recombination coefficient	B_0	$3{\cdot}10^{-11}$ cm^3 s^{-1}[48]	$8.5{\cdot}10^{-11}$ cm^3 s^{-1}[46]
Auger recombination coefficient	C	$2.3{\cdot}10^{-28}$ cm^6 s^{-1}[47]	$5{\cdot}10^{-30}$ cm^6 s^{-1}[46]
Electron mobility	$\mu_{e,0}$	5000 cm^2 V^{-1} s^{-1}[49]	3150 cm^2 V^{-1} s^{-1}[46]
Electron mobility temperature exponent	γ_e	1.9[50]	0.9[51]
Hole mobility	$\mu_{h,0}$	850 cm^2 V^{-1} s^{-1}[52]	640 cm^2 V^{-1} s^{-1}[46]
Hole mobility temperature exponent	γ_h	2.3[50]	1.5[46]
Conduction band effective density of states	$N_{c,0}$	$1.9{\cdot}10^{17}$ cm^{-3}[53]	$2.1{\cdot}10^{17}$ cm^{-3}[54]
Valence band effective density of states	$N_{v,0}$	$1.5{\cdot}10^{19}$ cm^{-3}[53]	$1.8{\cdot}10^{19}$ cm^{-3}[54]
Lattice thermal conductivity	κ	0.14 W cm^{-1} K^{-1}[55]	0.3 W cm^{-1} K^{-1}[55]
Static dielectric constant	ϵ	15.64[53]	15.7[54]
Series Resistance	R	0.779Ω†	
Light Collection Efficiency	η_{col}	24.5%†	

Table 2.1: Material parameter values used for numerical modeling and sources for each.

2.2.1 A Resistor

To begin we will model charge and energy transfer in an (n)-doped GaSb resistor with a donor density of 10^{16} cm^{-3}. A resistor is a useful first case study in charge and energy

Model	Formula	Units
Band Gap	$E_{\text{gap}} = E_{\text{gap,0}} - \alpha(T-300) - A_{\text{i}}N_{\text{i}}^{\frac{1}{3}} - B_{\text{i}}N_{\text{i}}^{\frac{1}{4}} - C_{\text{i}}N_{\text{i}}^{\frac{1}{2}}$	eV
Effective densities of states	$N_{\text{i}} = N_{\text{i,0}}\left(\frac{T}{300}\right)^{\frac{3}{2}}$	cm^{-3}
Electron mobility	$\mu_{\text{e}} = \mu_{\text{e,0}}\left(\frac{T}{300}\right)^{-\gamma_{\text{e}}}$	$\text{cm}^2\,\text{V}^{-1}\,\text{s}^{-1}$
Hole mobility	$\mu_{\text{h}} = \mu_{\text{h,0}}\left(\frac{T}{300}\right)^{-\gamma_{\text{h}}}$	$\text{cm}^2\,\text{V}^{-1}\,\text{s}^{-1}$
SRH recombination rate	$R_{\text{SRH}} = \frac{np-n_{\text{i}}^2}{\tau_{\text{SRH,h,0}}\left(\frac{T}{300}\right)^{-\frac{3}{2}}(n+n_{\text{i}})+\tau_{\text{SRH,e,0}}\left(\frac{T}{300}\right)^{-\frac{3}{2}}(p+n_{\text{i}})}$	$\text{cm}^{-3}\,\text{s}^{-1}$
Surface SRH recombination rate	$R_{\text{SRH,surf}} = \frac{np-n_{\text{i}}^2}{v_{\text{surf}}(n+p+2n_{\text{i}})}$	$\text{cm}^{-2}\,\text{s}^{-1}$
Bimolecular recombination rate	$R_{\text{rad}} = B_0\left(\frac{T}{300}\right)^{-\frac{3}{2}}\left(\frac{E_{\text{gap}}}{E_{\text{gap,0}}}\right)^2(np-n_{\text{i}}^2)$	$\text{cm}^{-3}\,\text{s}^{-1}$
Auger recombination rate	$R_{\text{Aug}} = C(n+p)(np-n_{\text{i}}^2)$	$\text{cm}^{-3}\,\text{s}^{-1}$

Table 2.2: Equations used to calculate band gap narrowing, carrier mobilities and recombination rates as functions of carrier density, dopant density, lattice temperature and the material parameters given in Table 2.1.

transport because it isolates charge transfer due to drift and energy transfer from the carriers to the lattice by the Joule heating. A constant doping profile dictates that neither majority nor minority carrier density diffusion should contribute to the current density. The chemical potential $\mu = E_C - E_{Fn}$ remains constant and the electron and hole quasi-Fermi energies are equal throughout the device. When a voltage is applied to the resistor the same constant gradient appears in the conduction band edge energy and Fermi energy, as depicted in Figure 2-1. As electrons flow down the potential energy gradient across the device they gain kinetic energy. This gain in kinetic energy gain appears as the first term on the right-hand-side of Equation 1.33 for electrons:

$$\nabla \cdot \vec{S}_e = \vec{J}_e \cdot \nabla E_C - \frac{3}{2}k_B\left[T_e R_{net} - \frac{T_e - T_l}{\tau_e}\right]$$

This kinetic energy is then lost to the lattice through collisions. The energy relaxation time describes the rate at which this energy transfer occurs on average. In GaSb the energy relaxation time is taken to be 1.5 picoseconds for electrons and holes [56]. In later steps the same energy relaxation time will be used for GaInAsSb

because experimental data about carrier energy relaxation in this material is not presently available. Once this energy is transfered to the lattice it is conducted out as heat, as described by Equation 1.39:

$$\vec{S}_l = -\kappa \nabla T_l$$

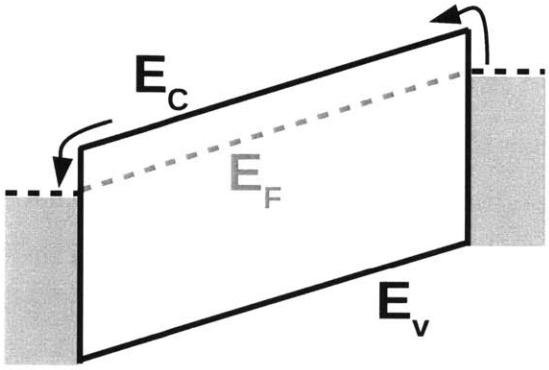

Figure 2-4: Band diagram of an n-doped resistor showing the relative energies of the conduction band edge the conduction band edge E_{C}, the Fermi level E_{F} and the valence band edge E_{V}. The black arrows indicate Peltier energy exchange at the contacts.

Peltier heat transfer at the contacts is depicted in 2-4 by black arrows. The arrow on the right indicates the change in average conduction energy that occurs as electrons pass from a metal where conduction almost exactly the Fermi energy on average, to semiconductor where conduction must occur at energies above the Conduction Band edge. Electrons traversing this junction first lose energy as a result of this change and then subsequently absorb energy from the lattice to re-equilibrate. Thus cooling occurs as majority carriers enter a device the contacts. The arrow on the left indicates the opposite process, where carriers lose the extra conduction energy and heat the lattice. The magnitude of Peltier cooling where electrons enter this resistor should be equal to that of the Peltier heating that occurs when the electrons since the difference in conduction energy is the same at both interfaces. Thus the net contribution of these two processes to energy transfer into or out of the device should be zero.

Sentaurus does not have a model for Peltier energy exchange across metal-semiconductor interfaces. However by examining how conduction energy changes as carriers enter

and leave the device through the contacts we can directly calculate what this energy exchange should be. Calculating Peltier exchange that should be present at the contacts allows us to confirm conservation of energy in a given model, but it does not permit self-consistent coupling of carrier and lattice energy flux and temperature profiles to recombination and current density calculations. In this model lattice heat transfer out of the resistor matches input electrical work exactly, indicating that energy is conserved. This occurs because the difference between metal and semiconductor conduction energy is the same at both contacts since the resistor is uniformly doped throughout. Thus the Peltier exchange that occurs as electrons enter this resistor is equal and opposite to that which occurs when they leave on the other side, and the two contributions cancel. This will not be true of the devices modeled in later steps. We note that although energy conservation holds in this device, the missing energy source and sink corresponding to Peltier exchange at the contacts affects the calculated steady state energy flux and temperature distributions.

The results of the simulation or a resistor are shown in Figure 2-5. As we expect for a resistor, the band diagram has a constant gradient and simulated the current-voltage characteristic is linear. The temperature distribution is parabolic, indicative of uniform energy dissipation from the electrons to the lattice. The energy flow distribution shows that the electrons carry in approximately the same amount of energy that they carry out, while the lattice is conducting heat away from the center of the resistor. The lack of heat flow out of the device through the electrons indicates that the lattice thermal conductivity is much larger than that of the electrons. We note that there is a small steady-state difference in the temperature of the electrons and that of the lattice across the device. The non-zero energy relaxation time that couples electron kinetic energy density gained by flowing down a potential gradient to lattice heat. Finally the electrical power input is equal to the heat power flowing out of t he device for all bias conditions. Thus we have demonstrated complete transfer of work done on the electrons to lattice heat.

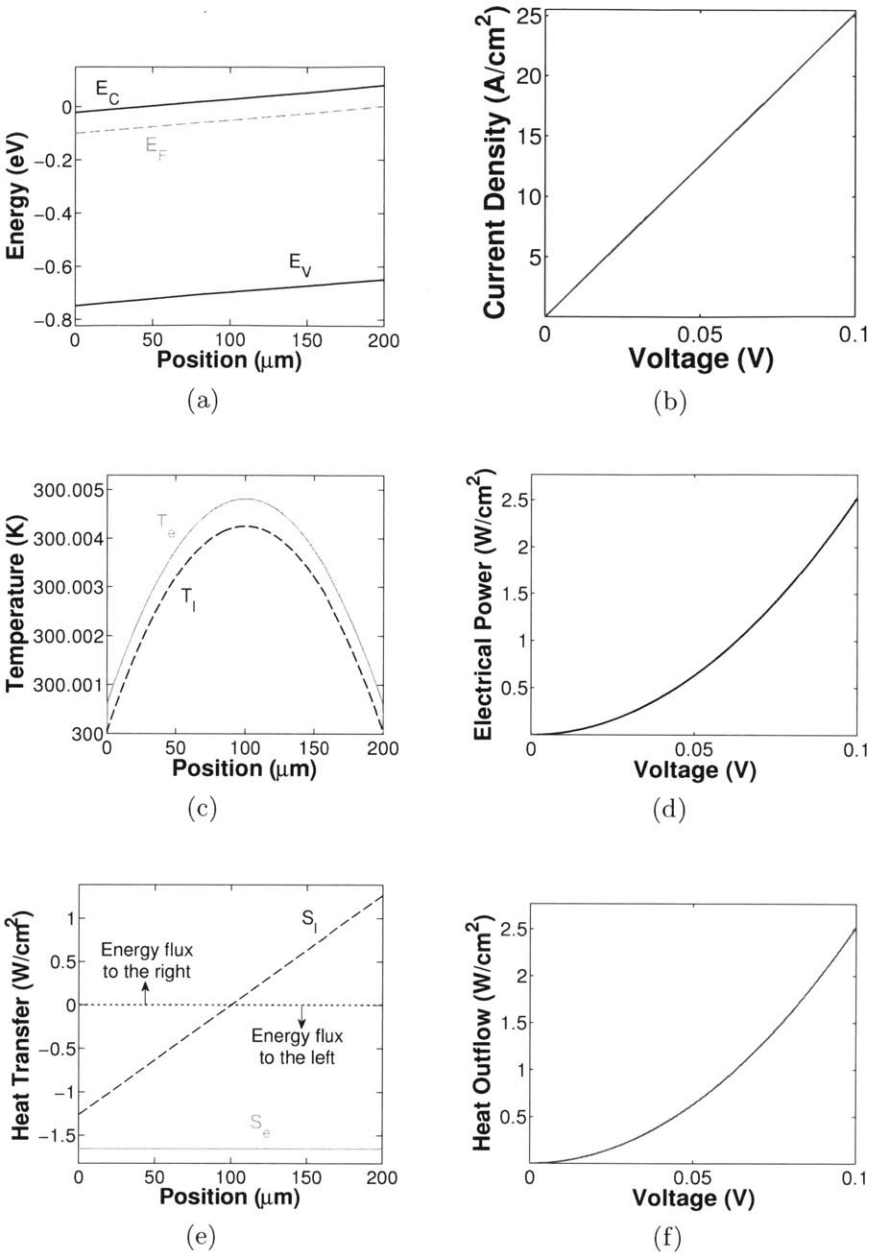

Figure 2-5: Simulated resistor 100mV bias in 300°K ambient. (a) Band diagram indicating the spatial profiles of the relative energies of the conduction band edge E_{C}, the Fermi level E_{F} and the valence band edge E_{V}, (b) simulated J-V curve, (c) spatial profile of the electron temperature T_{e} and lattice temperature T_{l}, (d) electrical work as a function of applied voltage bias, (e) spatial profile of energy flux through the lattice $\vec{S}_{\mathrm{l}}$ and electrons $\vec{S}_{\mathrm{e}}$, and (f) net heat flux out of the resistor through the lattice.

2.2.2 A *p*-*n* Junction in the Long-Base Limit

We now turn to the *p*-*n* junction. The charge and energy transport characteristics of this device are different than those of a resistor in a few important ways. First since placing a *p* doped region next to an *n* doped region creates a large spatial gradient in carrier density, we know that carrier-density-gradient-driven diffusion will determine current. We also see that diffusing minority carriers will flow across a band-edge gradient near the junction that will give rise to Peltier cooling. Similar to the resistor, Peltier cooling should occur when carriers enter the semiconductor. In this case however, the Peltier exchange that occurs if a carrier diffuses to the opposite contact should account for the both energy gained upon entering the semiconductor as well as the energy gained from the band edge gradient at the junction. If carriers do not diffuse to the opposite contact but instead recombines somewhere in the device, then energy equal to the sum of the electron and hole carrier energies and the band gap energy the band gap energy is released either in the form of a phonon or a photon [33]. Phonons contribute to the energy density in the lattice while photons contribute to the energy density of the electromagnetic field. In the case of net recombination energy will leave the device through both of these media. For the sake of simplicity we will first model a *p*-*n* junction in which the vast majority of minority carriers recombine before reaching the contact, a regime known as the long-base limit. Also only one form of non-radiative Shockley-Read-Hall (SRH) recombination will be modeled. The relevant energy transfer pathways in this device are depicted in Figure 2-6.

Plots depicting this modeled diode are presented in Figure 2-7 and the simulated electrical and thermal characteristics are given in Figure 2-8. Almost all carriers recombine very near the *p*-*n* interface the electron and hole quasi-Fermi levels come back into equilibrium away from the contacts. We see that holes and electrons carry energy toward the junction from the *p*- and *n*-side contacts respectively, and that the lattice conducts heat away from the junction once it is released by electron-hole recombination. We notice however that simulated lattice heat flow out of the device

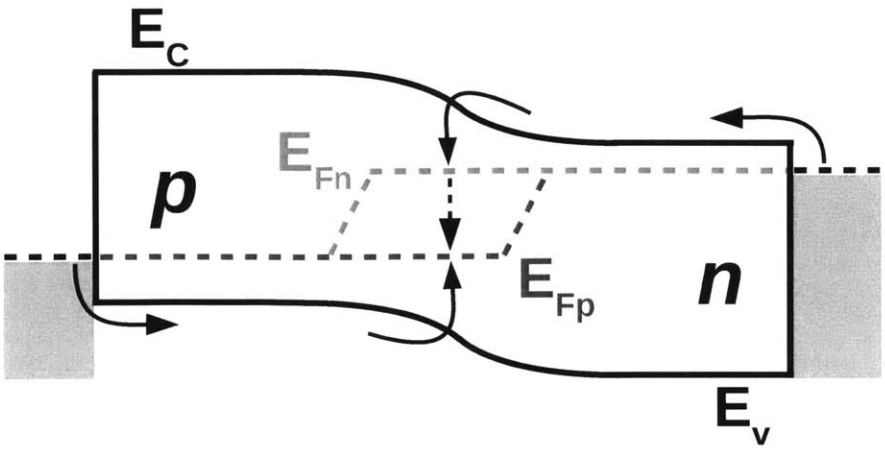

Figure 2-6: Long p-n junction. The curved black arrows again indicate Peltier exchange. The vertical arrows near the junction of the device indicate energy transfer during recombination event. The solid vertical arrows indicate the contribution of energy gained from Peltier exchange to the emitted phonon or photon and the dashed verticle arrow indicates the contribution of work done by the applied electric potential gradient.

is larger than the electrical power dissipated. This is because the Peltier energy exchange at at the contacts depicted in Figure 2-6 is not included in this model. Following Chapter 2 of *Bipolar Thermoelectric Devices* by Pipe [33], the cooling occurring at the contacts should be:

$$\begin{aligned} Q_{contacts} &= Q_{pcontact} + Q_{ncontact} \\ &\approx J(\Delta\Pi_p + \Delta\Pi_n) \\ &= J[(\frac{E_{Fp} - E_V}{q} + \Pi_{h,p}) + (\frac{E_C - E_{Fn}}{q} + \Pi_{e,n})] \end{aligned} \tag{2.1}$$

where we assume that only majority carriers contribute to Peltier exchange at each contact because the diode is in the long base limit. This assumption is checked by calculating the difference between the electrical work done and the heat flux out of the diode and dividing by current:

$$(\Pi_{pcontact} + \Pi_{ncontact}) = \frac{Q_{out} - JV}{J} \tag{2.2}$$

We expect that the missing heat should account for the energy differences between the Fermi levels and band edges at the contacts as well as the increase in average kinetic energy carriers experience when entering passing from a metal with a symmetric density of states to a semiconductor where the density states is highly asymmetric near the band edges [34, 39].

$$(\Pi_{pcontact}+\Pi_{ncontact}) = [E_{Fp}-E_V]_{pcontact}+[E_C-E_{Fn}]_{ncontact}+\frac{5}{2}(r_e\lambda_e+r_h\lambda_h)k_BT \quad (2.3)$$

where the last term on the right hand side of Equation 2.3 gives the summed average kinetic energies of electrons and holes associated with conduction. We recall from Equation 1.38 that r_i is related to the power law dependence on energy scattering of the scattering rate for a given carrier species.

$$\frac{1}{\tau_i} \sim E^{\frac{5}{2}(1-r_i)}$$

and from Equations 1.31 and 1.32 that λ_e and λ_h represent correction factors for the average energy of conducting carriers outside of the Boltzmann limit.

$$\lambda_e = \frac{F_{\frac{1}{2}}\left(\frac{E_C-E_{Fn}}{k_BT_e}\right)}{F_{-\frac{1}{2}}\left(\frac{E_C-E_{Fn}}{k_BT_e}\right)}$$

$$\lambda_h = \frac{F_{\frac{1}{2}}\left(\frac{E_{Fp}-E_V}{k_BT_h}\right)}{F_{-\frac{1}{2}}\left(\frac{E_{Fp}-E_V}{k_BT_h}\right)}$$

The value of $\Pi_{pcontact}+\Pi_{ncontact}$ calculated from the simulated device characteristics according to Equation 2.2 is plotted in Figure 2-8. This value is independent of the applied voltage bias and equal to exactly the analytical prediction given by Equation 2.3. Thus we have shown that we can track energy transfer in a *p-n* junction in the long base limit with the exception of the Peltier cooling that should occur when majority carriers enter the device at the contacts.

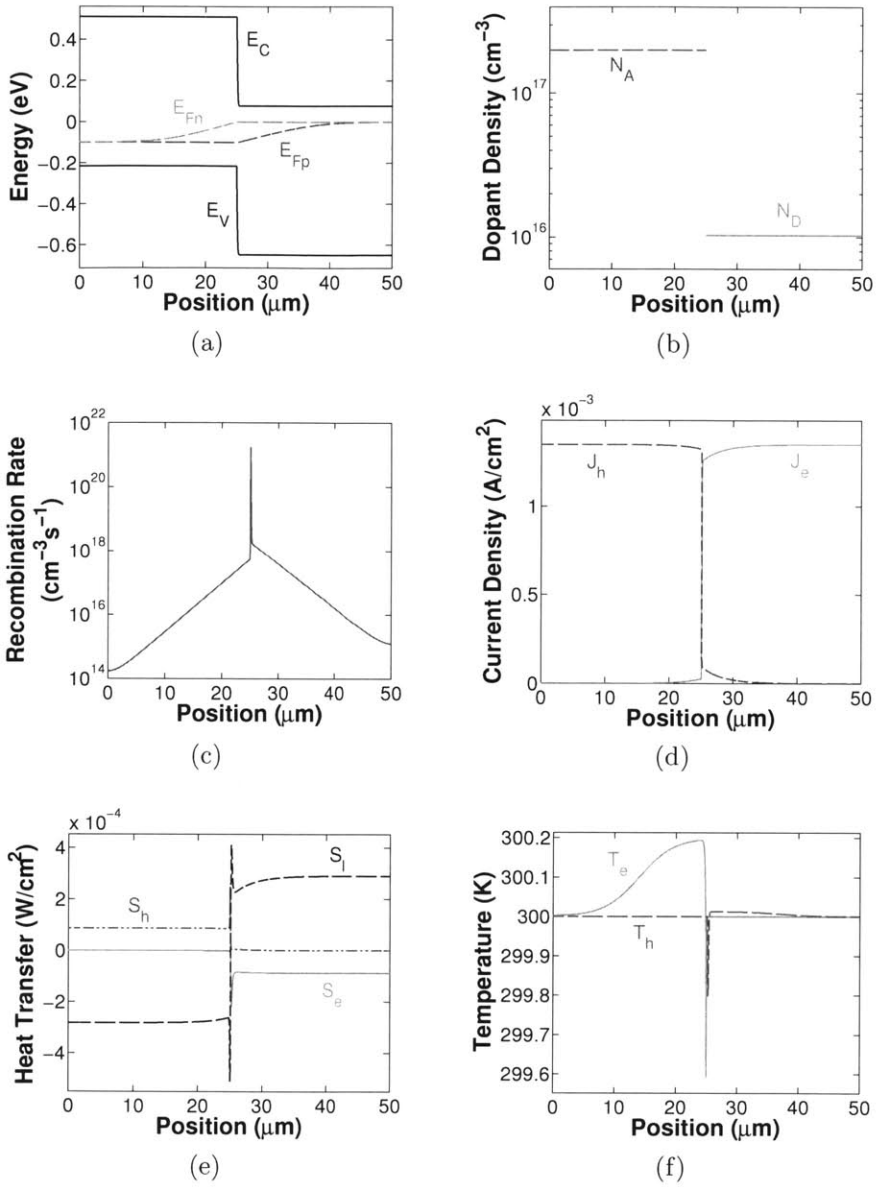

Figure 2-7: Spatial profiles of a simulated p-n junction in the long base limit at 100mV bias in 300°K ambient. (a) Band diagram indicating the relative energies of the conduction band edge E_{C}, the electron Fermi level E_{Fn}, the hole Fermi level E_{Fp} and the valence band edge E_{V}, (b) donor (N_{D}) and acceptor (N_{A}) dopant densities, (c) SRH recombination rate, (d) electron and hole current densities J_{e} and J_{h} (c) electron and hole temperatures T_{e} and T_{h}, (e) energy flux through the lattice $\vec{S}_{\mathrm{l}}$, electrons $\vec{S}_{\mathrm{e}}$ and holes $\vec{S}_{\mathrm{h}}$.

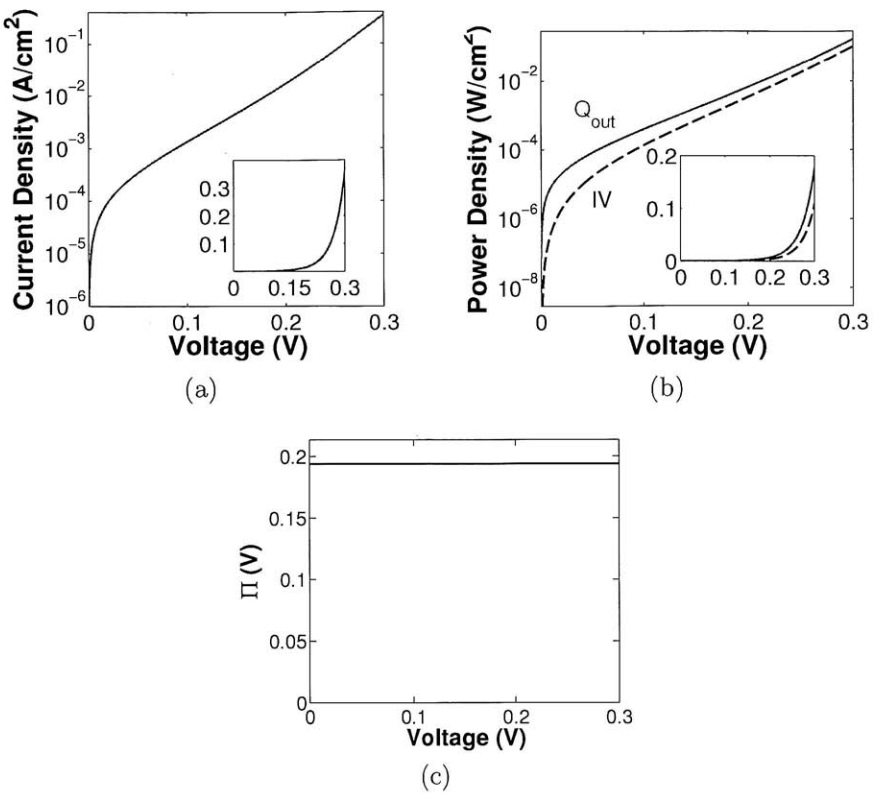

Figure 2-8: Simulated device characteristics of a p-n junction in the long base limit in 300°K ambient. (a) simulated J-V characteristic plotted on a semi-logarithmic scale and on a linear scale in the inset, (b) Input electrical work IV and heat flow out Q_{out} as a function of applied voltage on a semi-logarithmic scale and on a linear scale in the inset, (c) calculated combined Peltier coefficient at contacts.

2.2.3 A *p-i-n* Junction in the Short-Base Limit

Next, we move our diode out of the long-base limit to see how minority carriers diffusing all the way to the contacts affect the model for energy transfer in the diode. This is accomplished by shortening the length of the entire diode and increasing the carrier lifetime associated with SRH recombination. We also add a longer transition region between the p and n sides. The purpose of this is merely to further resemble the structure of the LED that we eventually intend to model. As depicted in Figure 2-9, Peltier energy transfer occurs both when carriers enter this device and when they leave. In this device minority carriers that diffuse all the way to the contact undergo surface recombination and lose energy equal to the Peltier heat they absorbed while traversing the diode plus the applied potential difference. This energy transfer is not

accounted for in the hydrodynamic model of Sentaurus. Thus carriers that traverse the entire diode appear to remove heat from the lattice that is never re-deposited.

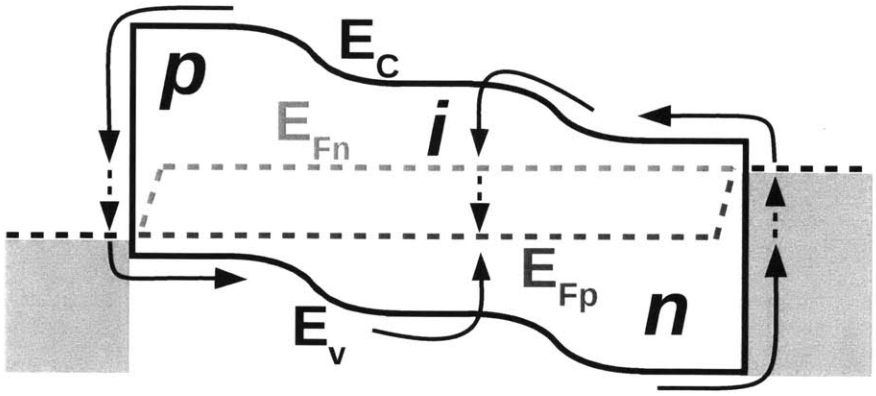

Figure 2-9: Short *p-i-n* junction. Arrows indicate energy exchange as in Figure 2-6. Because this diode is not in the long-base limit some minority carriers diffuse to the contacts before recombining.

The simulation results for this *p-i-n structure* are presented in Figure 2-10. We see that significant minority carrier current reaches the contacts. Otherwise the properties of energy transport across this diode look fairly similar to those across the *p-n* junction. We can see that the majority of bulk SRH recombination happens in the intrinsic region, and that a significant portion of the heat transfered to the lattice by this recombination is reabsorbed by the holes at the *p-i* interface and by the electrons at the *i-n* interface. The majority carrier temperatures also dip slightly at the edge of the intrinsic region. These are signatures of the Peltier cooling that is occurring at these interfaces.

The simulated device characteristics, shown in Figure 2-11, also look fairly similar to the previous device. We see that as the bias is increased the margin between heat flux out through the lattice and electrical work decreases, corresponding to missing surface recombination heat. Thus we have shown that energy transfer due to surface recombination at the contacts is also missing from our diode model and must be accounted for externally.

We have learned from these three device models that energy transfer due to Joule heating, recombination and Peltier transfer within the device is modeled correctly,

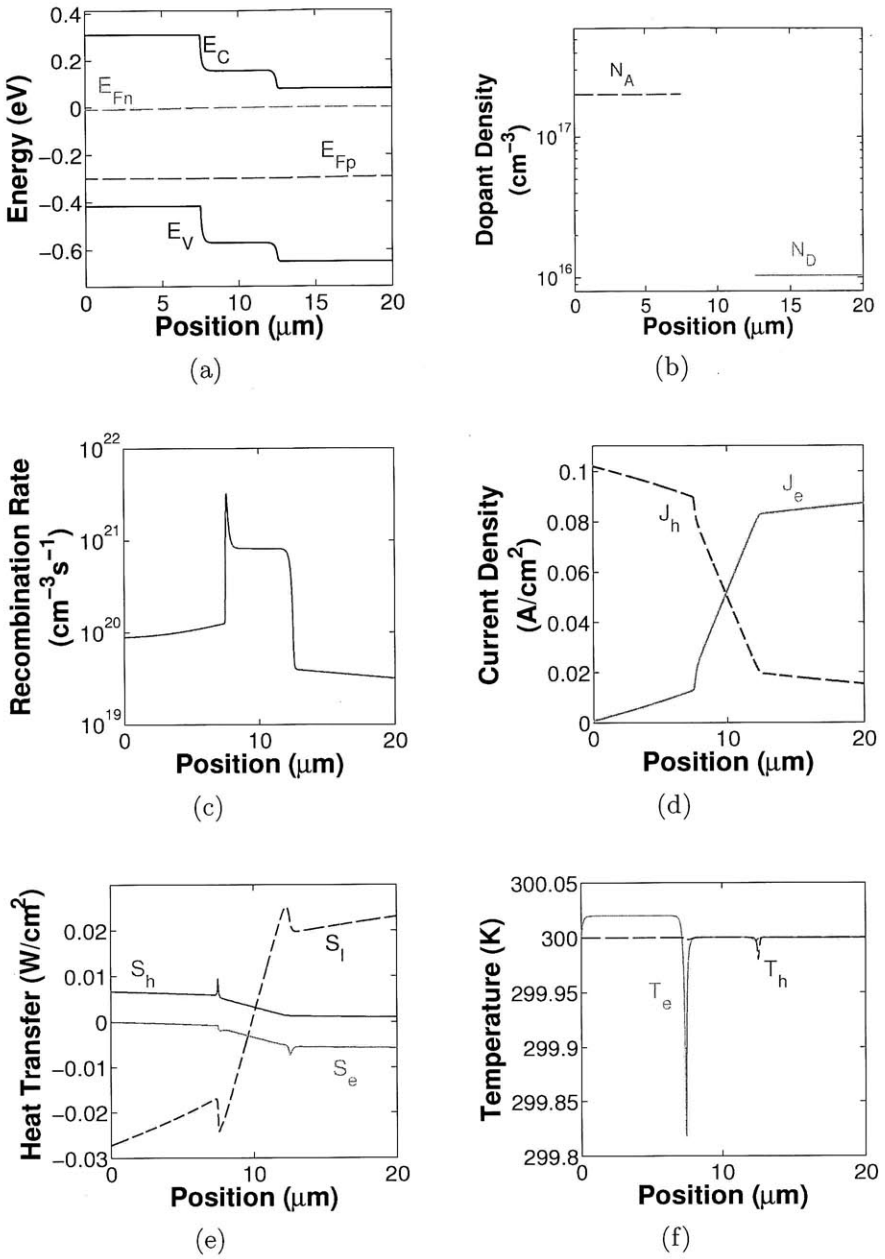

Figure 2-10: Spatial profiles of a simulated p-i-n junction at 300mV bias in 300°K ambient. (a) Band diagram indicating the relative energies of the conduction band edge E_{C}, the electron Fermi level E_{Fn}, the hole Fermi level E_{Fp} and the valence band edge E_{V}, (b) donor (N_{D}) and acceptor (N_{A}) dopant densities, (c) SRH recombination rate, (d) electron and hole current densities J_{e} and J_{h} (c) electron and hole temperatures T_{e} and T_{h}, (e) energy flux through the lattice $\vec{S}_{\mathrm{l}}$, electrons $\vec{S}_{\mathrm{e}}$ and holes $\vec{S}_{\mathrm{h}}$.

while energy transfer at the contacts due to Peltier exchange and surface recombination is not. Luckily we can readily calculate these missing quantities based on the

current flowing through the device, the average carrier energy associated with conduction, and the amount of minority carrier current that diffuses all the way across the diode.

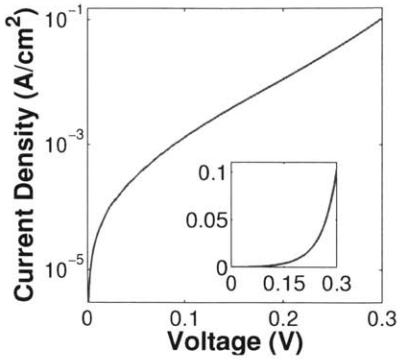

(a)

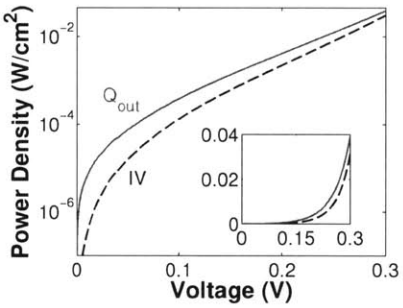

(b)

Figure 2-11: Simulated device characteristics of a *p-i-n* junction in 300°K ambient. (a) simulated J-V characteristic on a semi-logarithmic scale and on a linear scale in the inset, (b) Input electrical work IV and heat flow out Q_{out} as a function of applied voltage on a semi-logarithmic scale and on a linear scale in the inset.

2.2.4 A *p-i-n* Double-Heterojunction with Radiative Recombination

By making our *p-i-n* structure a double heteojunction and adding radiative and Auger recombination, our diode begins to closely resemble the LED presented in Section 2.1. The *p-* and *n-* regions will still be modeled as GaSb but the intrinsic region will be modeled as $In_{.15}Ga_{.85}As_{.13}Sb_{.87}$ which has a band gap approximately 75% that of GaSb (see 2.1). The dominant energy transfer processes in this diode are

shown in Figure 2-12. Minority carrier diffusion should not contribute significantly to conduction because of the large band discontinuities at the hetero-interfaces. In this version of the model energy transfered to photons by radiative recombination will not be be assumed to leave the system, corresponding to perfect optical extraction. We also include degenerate doping on the n-side of this diode.

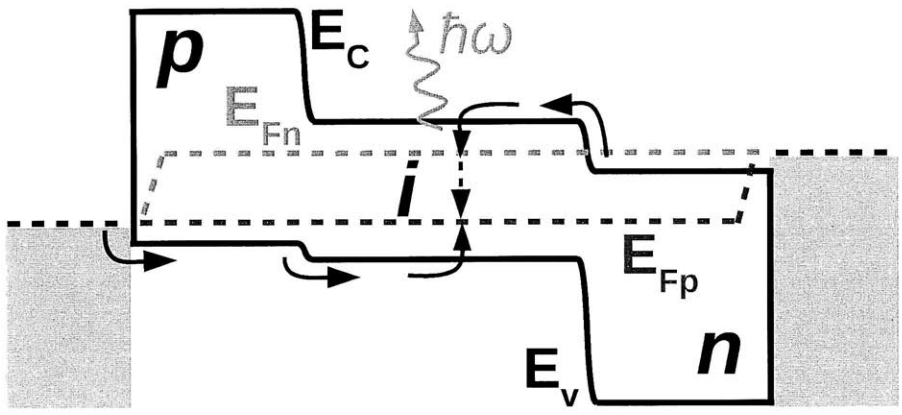

Figure 2-12: p-i-n double heterojunction. Black arrows indicate energy exchange as in Figures 2-6 and 2-9. The pink arrow indicates light-mediated energy transfer out of the device.

Figure 2-13 shows spatial profiles of various microscopic variables across the LED. This snapshot of the diode at a 100mV bias indicates that recombination happens approximately uniformly across the intrinsic region and that non-radiative SRH recombination dominates over radiative recombination by almost two orders of magnitude. By examining the energy flux diagram we observe significant cooling as both the p-i and i-n interfaces as majority carriers enter the active region.

We see in Figure 2-14 that over the bias range of interest the Peltier coefficient for cooling at the contacts, calculated using the difference between input electrical power and the total energy outflow through light and lattice heat is approximately constant over the bias range of interest. This indicates that minority diffusion current is not particularly important in this device.

Figure 2-15 shows the predicted light-current relationship for this LED. By plotting the quantum efficiency together with the average electron and hole concentrations

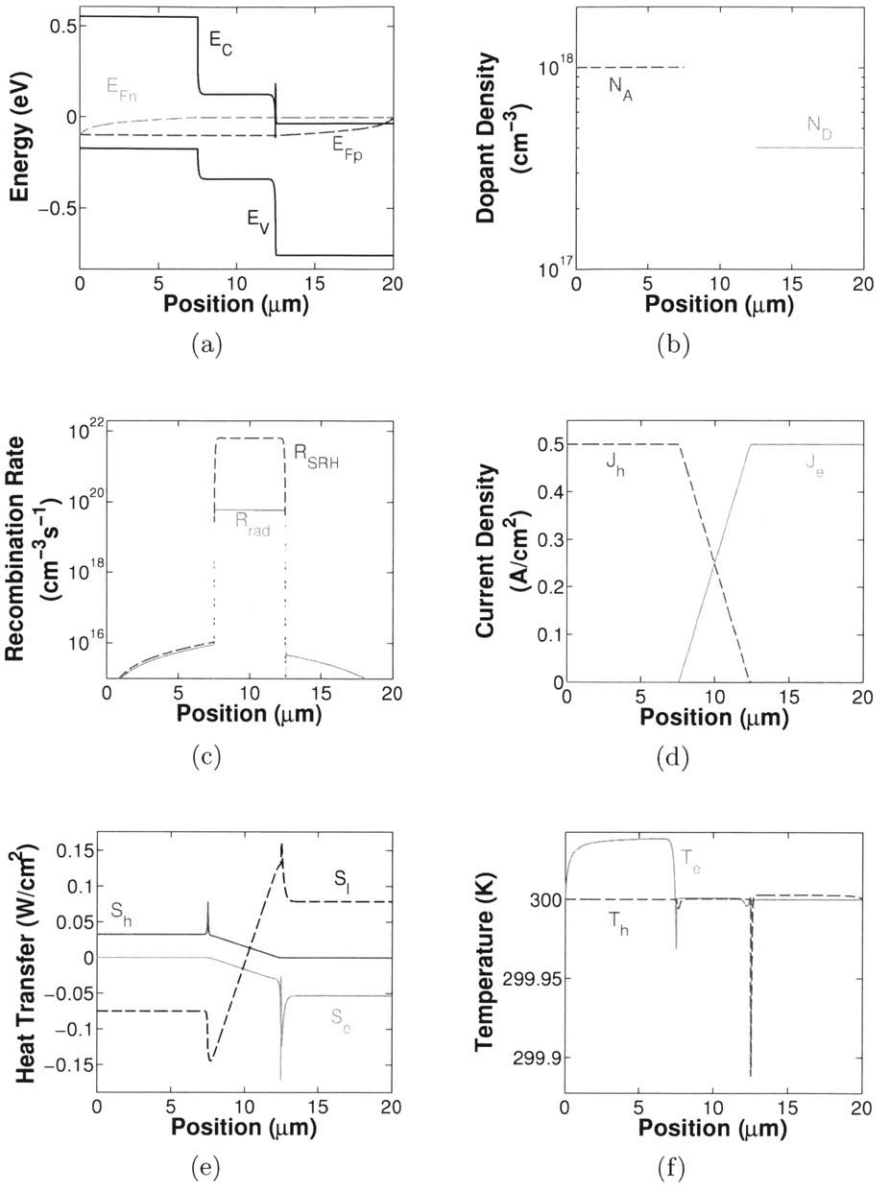

Figure 2-13: Spatial profiles of a simulated *p-i-n* double heterojunction at 100mV bias in 300°K ambient. (a) Band diagram indicating the relative energies of the conduction band edge E_{C}, the electron Fermi level E_{Fn}, the hole Fermi level E_{Fp} and the valence band edge E_{V}, (b) donor (N_{D}) and acceptor (N_{A}) dopant densities, (c) SRH recombination rate, (d) electron and hole current densities J_{e} and J_{h} (c) electron and hole temperatures T_{e} and T_{h}, (e) energy flux through the lattice $\vec{S}_{\mathrm{l}}$, electrons $\vec{S}_{\mathrm{e}}$ and holes $\vec{S}_{\mathrm{h}}$.

across the active region, we can see that quantum efficiency reaches a minimum at low injection levels once the carrier populations approach their equilibrium values. Note

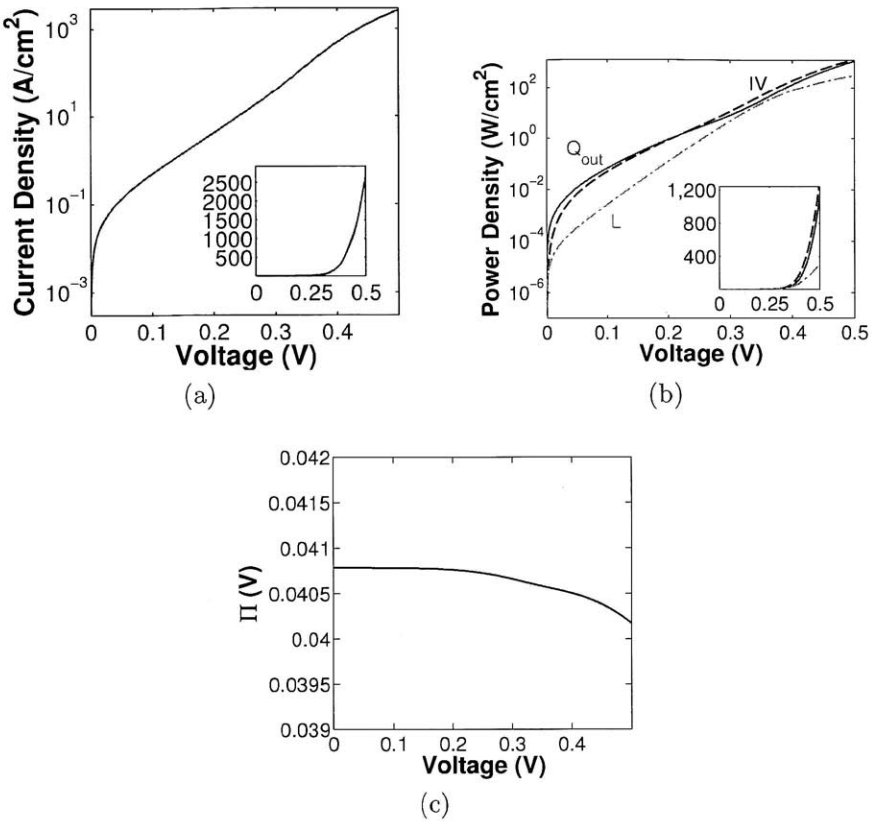

Figure 2-14: Simulated electrical characteristics of a p-i-n double heterojunction LED in 300°K ambient. (a) simulated J-V characteristic on a semi-logarithmic scale and on a linear scale in the inset, (b) Input electrical work IV and heat flow out Q_{out} as a function of applied voltage on a semi-logarithmic scale and on a linear scale in the inset, (c) calculated combined Peltier coefficient at contacts.

that the equilibrium electron and hole densities averaged across the active region vary slightly as a result of asymmetric charge screening at the p-i and i-n interfaces.

Dopant Diffusion

One structural aspect of the LED21Sr that has not yet been considered is dopant diffusion into the active region. As shown above, the low-bas quantum efficiency of the LED is affected by the carrier concentration in the active region. Dopant diffusion from the doped GaSb layers into the GaInAsSb layer could thus make a significant impact on device efficiency in this regime. The liquid-phase epitaxial growth method used to fabricate the LED21Sr generally does not result in abrupt doping profiles [57, 58, 59]. We can highlight the importance of dopant diffusion to

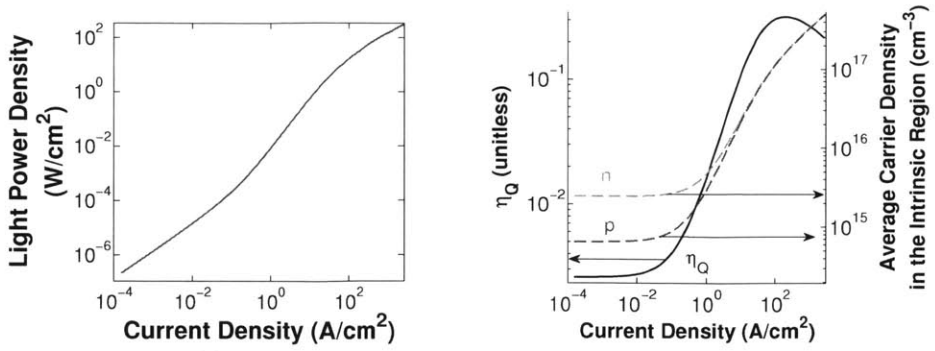

Figure 2-15: Simulated electrical-to-optical energy conversion characteristics of a p-i-n double heterojunction LED in 300°K ambient. (a) simulated L-J characteristic, (b) internal quantum efficiency η_Q and average electron and hole carrier densities n and p as a function of injected current.

the characteristics of the LED by modeling the same device with dopants diffused into the active region. Analysis of the doping profiles achieved with liquid-phase epitaxy suggest that modeling dopant diffusion across region interfaces with Gaussian profiles is more accurate [59]. Studies of dopant diffusion associated with LPE in the GaSb material system suggests that modeling diffusion with a characteristic length of approximately 100nm should be reasonable [58]. In this case we have graded the dopant densities from the constant doping values in the p and n regions to values far below the room temperature intrinsic carrier concentration at the center of the active region. The grading profile used on each side is Gaussian with a characteristic length of 100nm. Figure 2-16 shows a snapshot of the diode with dopant diffusion under the same 100mV electrical bias as in Figure 2-13. We see that dopant diffusion simultaneously reduces the relative importance of SRH recombination and increases the importance of Auger recombination across the active region of the device by raising the average carrier density.

The electrical characteristics of the LED with dopant diffusion are shown in Figure 2-14. We see that the predicted electrical characteristics of the device are not heavily affected by this change, although slightly more current is expected to flow through the device at high bias as a result of increased Auger recombination.

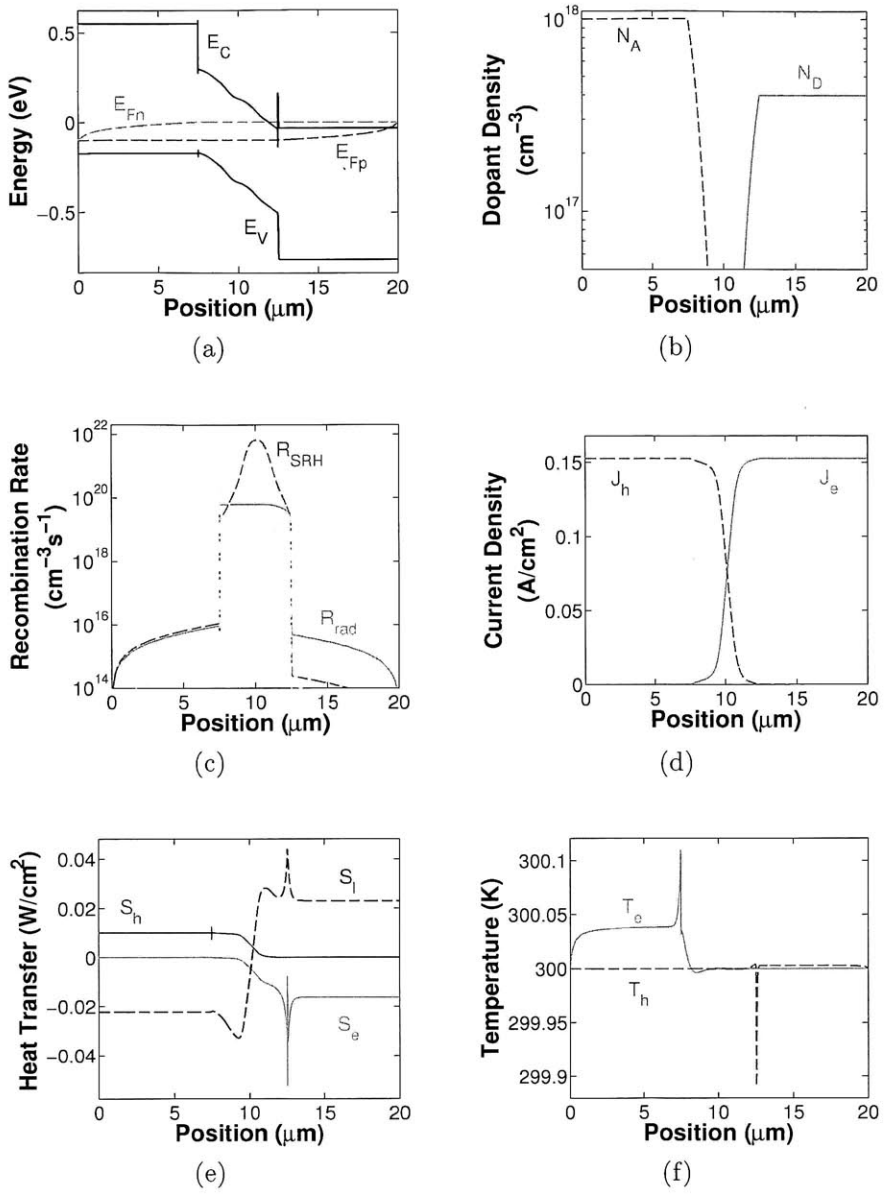

Figure 2-16: Spatial profiles of a simulated *p-i-n* double heterojunction with dopant diffusion at 100mV bias in 300°K ambient. (a) Band diagram indicating the relative energies of the conduction band edge E_{C}, the electron Fermi level E_{Fn}, the hole Fermi level E_{Fp} and the valence band edge E_{V}, (b) donor (N_{D}) and acceptor (N_{A}) dopant densities, (c) SRH recombination rate, (d) electron and hole current densities J_{e} and J_{h} (c) electron and hole temperatures T_{e} and T_{h}, (e) energy flux through the lattice $\vec{S}_{\mathrm{l}}$, electrons $\vec{S}_{\mathrm{e}}$ and holes $\vec{S}_{\mathrm{h}}$.

The simulated optical device characteristics shown in Figure 2-18 demonstrate an increase in low bias quantum efficiency from $2.6{\cdot}10^{-3}$ to $1.3{\cdot}10^{-2}$. This is a result of the

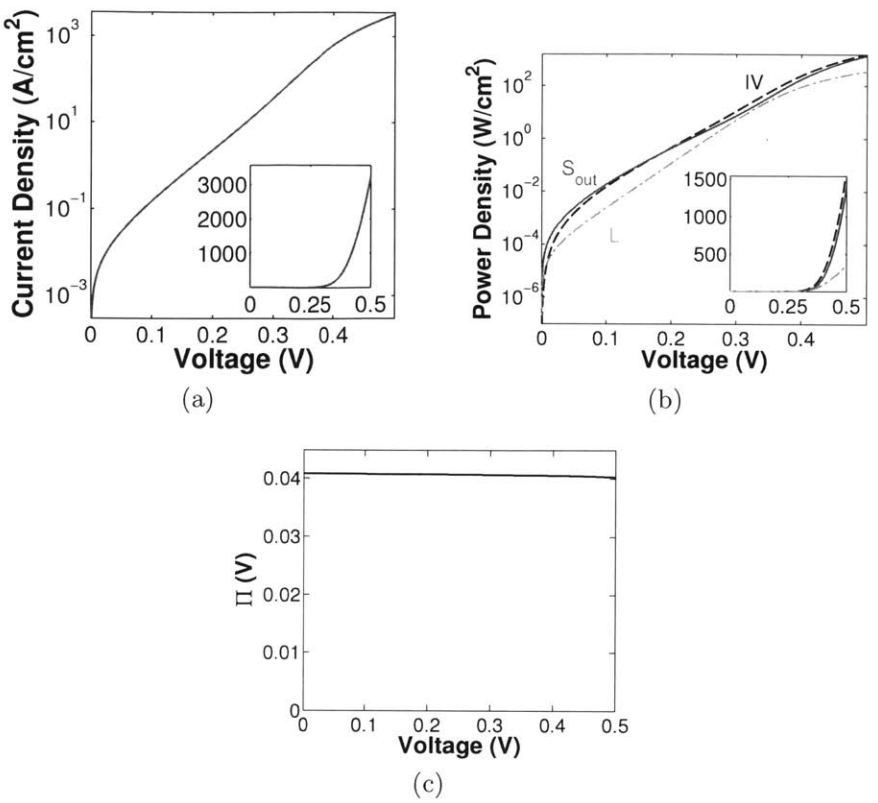

Figure 2-17: Simulated electrical characteristics of a *p-i-n* double heterojunction LED with dopant diffusion in 300°K ambient. (a) simulated J-V characteristic on a semi-logarithmic scale and on a linear scale in the inset, (b) Input electrical work IV and heat flow out Q_{out} as a function of applied voltage on a semi-logarithmic scale and on a linear scale in the inset, (c) calculated combined Peltier coefficient at contacts.

increased equilibrium carrier densities in the active region due to dopant diffusion.

Figure 2-19 shows the predicted light power density L plotted as a function of input electrical power density JV at low bias. We see that simulated light power density exceeds input electrical power density in these diodes and that it does so at a higher power level when the diode has dopants in the active region. We note however that this model does not yet consider the issue of light extraction. Even though the physical principles underlying electroluminescent cooling are not precluded by light extraction, this does mean that the power densities in this LED model do not yet reflect those expected in a real system. In the next Section we will attempt to correct for this.

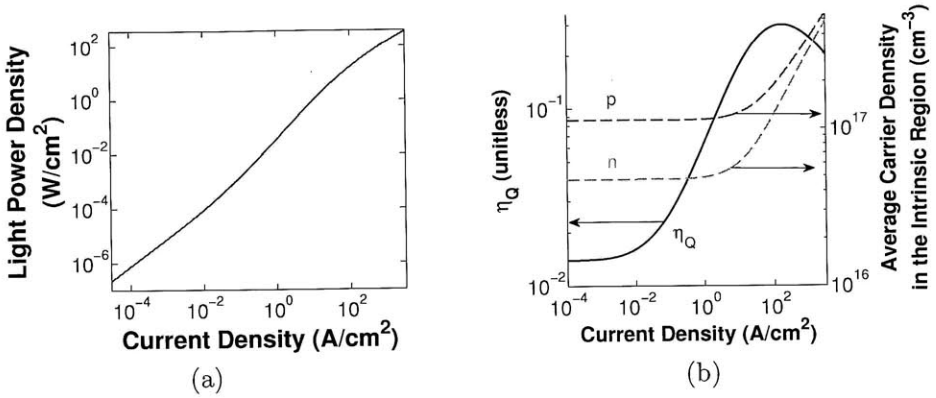

Figure 2-18: Simulated electrical-to-optical energy conversion characteristics of a p-i-n double heterojunction LED with dopant diffusion in 300°K ambient. (a) simulated L-J characteristic, (b) internal quantum efficiency η_Q and average electron and hole carrier densities n and p as a function of injected current.

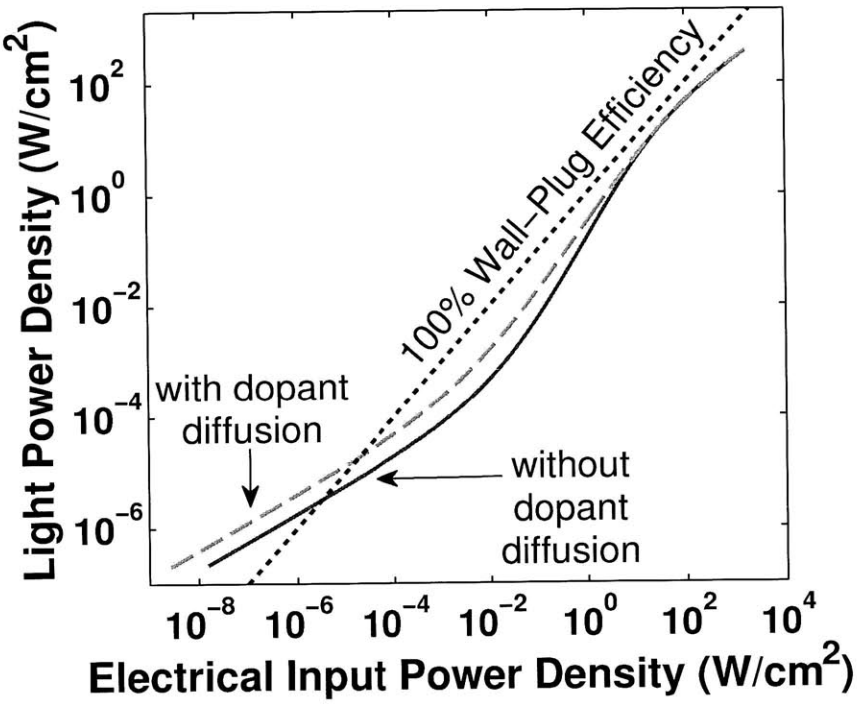

Figure 2-19: Output light power density L plotted against input electrical power density JV for p-i-n double heterojunction LEDs at 300°K with (red dashed) and without (blue) dopant diffusion into the active region. We see that electroluminescent cooling is predicted in both devices, but that it is predicted at higher power in the device with dopant diffusion. This results from a higher quantum radiative efficiency near equilibrium in the active region.

2.3 Modeling a Real LED

We now turn to the LED21Sr presented in Section 1 of this Chapter. Only a few modifications are necessary to transform the LED modeled in the previous Section into one that should resemble this existing device very closely. First we incorporate the geometry of the LED21Sr as presented in [2]. We use 4μm for the widths of the p-type GaSb and intrinsic GaInAsSb epitaxial layers and approximate the current path through the n-type region as 12μm, based on the flip-chip device geometry shown in Figure 2-1. Based on direct communication with the producers of these devices, we know that the active region of our sample is a circle approximately 280μm in diameter. Thus the transverse area of the device is taken to be $6.16 \cdot 10^{-4}$cm^2. We include the Jain-Roulston model for doping-dependent band gap narrowing [45] given in Table 2.2 in the p- and n- GaSb regions with the parameters given in Table 2.1. This model accounts for apparent shifts in band gap energy due to carrier-impurity interactions and many-body effects on carrier exchange energies [45]. We will also include non-radiative surface-SRH recombination at the GaSb/GaInAsSb interfaces. Section 2.3.1 deal with the inclusion of light extraction from the active region of the diode and photon recycling in the model. In Section 2.3.2 we will examine simulated characteristics of the LED21Sr.

2.3.1 Light Extraction and Photon Recycling

One essential piece of this model that has not yet been discussed is light extraction. Our one dimensional model for charge and energy transport across this does not calculate the probability that a photon generated by a radiative recombination event will escape the diode before being re-absorbed. We can approximate this probability by finding the average path length to the surface of a photon generated with a random trajectory at a random point in a slab as thick as the active region and using experimental absorption data for GaInAsSb at nearly the mole-fraction of our device [47].

The first step in this calculation is to generate a probability density function for

the path length of a photon generated in the active region. Given that the diameter of the active region cylinder is much greater than its thickness we neglect edge effects by approximating the the slab as infinite in the two transverse dimensions. We also assume that one face of the cylinder is highly reflective based on the experimental results presented in [2]. We will call the reflective surface the bottom of the cylinder and the non-reflective surface the top. We don't know whether reflection from the bottom surface is specular (angle preserving) or diffuse (angle randomizing), but we can bound the path length distribution by trying both assumptions.

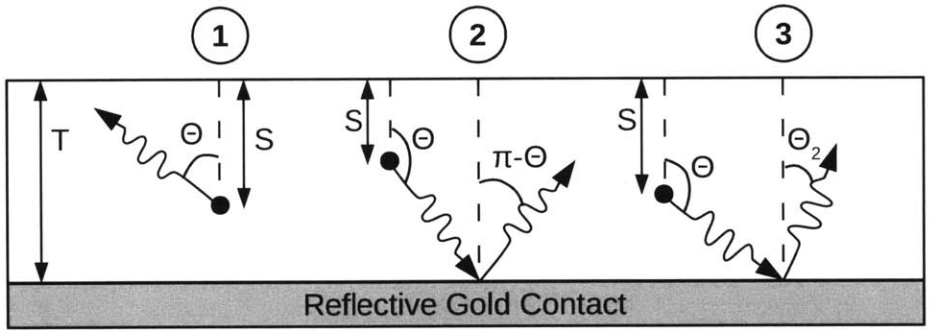

Figure 2-20: The three scenarios considered in our calculation of photon extraction from the active region are shown above. Each scenario starts with a photon emitted at a random polar angle from a random point in the slab. In Scenario 1 a photon is emitted upwards. In Scenario 2 a photon emitted downwards and then reflected off the gold contact on the back plane at angle determined by its original trajectory. This corresponds to a smooth contact surface. In Scenario 3 a photon is again emitted downwards but is reflected from the contact at a new random angle. This corresponds to contact suface roughness causing diffuse reflection. We note that the contact is separated from the active region by a p-GaSb layer in the LED21Sr, but that very little absorption should occur in this region and that the trajectory angle of a photon's second pass through the active region should not be affected by this layer.

As depicted in Figure 2-20, the path length of a photon L is a function of two random variables, the distance from the top surface S and the polar angle Θ.

$$L = \frac{S}{\cos\Theta} \tag{2.4}$$

First we consider the probability of escape if a photon is emitted upwards (in the top 2π steradians of the space of possible trajectories). Somewhat surprisingly, the

polar angle of a random trajectory is not uniformly distributed. This can be seen by considering the area of a differential ring-shaped slice of the surface area of a sphere associated with 2π radians of azimuthal angle and differential variation in polar angle $d\theta$. It is clear that the area of this differential ring grows as θ is varied from 0 to $\pi/2$ radians and then decreases as θ is varied from $\pi/2$ to π. Thus the probability distribution function f_Θ of Θ can be written

$$\begin{aligned} f_\Theta(\theta) &= \frac{dA}{A} \\ &= \frac{2\pi r^2 \sin\theta d\theta}{4\pi r^2} \\ &= \frac{\sin\theta}{2} \end{aligned} \tag{2.5}$$

Where A and dA are the surface area of a sphere and a differential element of that area respectively and r is the radius of the same sphere. Thus the cumulative distribution function F_Θ of θ can be written

$$\begin{aligned} F_\Theta(\theta) &= \int_0^\theta f_\Theta(\theta')d\theta' \\ &= \int_0^\theta \frac{\sin\theta'}{2} d\theta' \\ &= \frac{-\cos\theta}{2} + \frac{1}{2} \end{aligned} \tag{2.6}$$

Where $\frac{1}{2}$ is added as a constant of integration in the last step so that $0 \leq F_\Theta \leq 1$ for $0 \leq \theta \leq \pi$. By working with $X = \cos\Theta$ instead of Θ as a random variable, we can achieve a uniform distribution F_X.

$$F_X(x) = \frac{1-x}{2} \tag{2.7}$$

The distribution for the distance from the top of the slab $F_S(s)$ is also uniform.

$$F_S(s) = \frac{1}{T} \tag{2.8}$$

where T is the thickness of the slab. We now seek the cumulative distribution $F_L(l)$. First consider the distribution of path lengths if the photon is emitted upward. In this scenario probability is distributed uniformly over the space $S \in (0,T), X \in (0,1)$. $F_L, up(l)$ describes the area in X,S space where ${}^{s}/_{x} > l$. As shown in Figure 2-21 there are two discrete regimes, $l < T$ and $l \geq T$, which lead to a piecewise distribution $F_L, up(l)$.

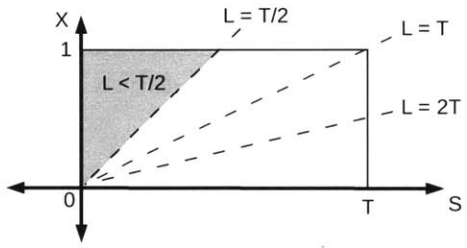

Figure 2-21: The space over which the random variables X and S are defined is depicted above. The dashed lines correspond to fixed X/S ratios and thus fixed path lengths. As shown for $L = T/2$, the probability that $L < l$ for a given l value set by the area above the line corresponding to $L = l$.

$$\begin{aligned} F_{L,up}(l) &= F_{{}^{s}/_{x}}({}^{s}/_{x}) \\ &= \begin{cases} \frac{1}{T}\frac{s}{2} & : \frac{s}{x} < T \\ \frac{1}{T}\frac{xT}{2} & : \frac{s}{x} \geq T \end{cases} \\ &= \begin{cases} \frac{l}{2T} & : l < T \\ 1 - \frac{T}{2l} & : l \geq T \end{cases} \end{aligned} \tag{2.9}$$

We know that X and S are also uniformly distributed in the space $S \in (0,T), X \in (-1,0)$. If we assume specular reflection, then $l = \frac{T-s}{x} + \frac{T}{x}$ where the first and second terms represent the path lengths before and after reflection respectively. We note that the minimum path length for emission downward is T and find the probability using an area calculation in X,S space as above:

$$F_{L,down,spec}(l) = \begin{cases} \frac{(l-T)^2}{2lT} & : T \leq l < 2T \\ 1 - \frac{3T}{2L} & : l \geq 2T \end{cases} \tag{2.10}$$

If reflection off of the back surface is diffusive, we add a third dimension $X_2 \in (0,1)$ to the X, S space in which the previous calculation was done to represent possible values of the cosine of the polar angle of reflection. The volume in X, S, X_2 space corresponding to $L < l$ can be calculated for $T < l < 2T$ to be

$$F_{L,down,diff}(l) \quad = \quad \frac{l-T}{6T} : T < l < 2T \tag{2.11}$$

We neglect the corresponding calculation for $l > 2T$ because it is significantly more complicated and these long path lengths will have little impact on this extraction calculation because extraction probability decreases exponentially with path length. We can bound the error this causes by comparing our extraction calculation results with (Equation 2.14) and without (Equation 2.13) all of the missing probability at exactly $2T$. The total path length distributions for specular and diffusive reflection at the backplane are now calculated by averaging $F_{L,up}$ with the corresponding $F_{L,down}$

$$
\begin{aligned}
F_{L,spec}(l) &= \frac{1}{2}(F_{L,up} + F_{L,down,spec}) \\
&= \begin{cases} \frac{l}{4T} & : l < T \\ \frac{1}{2} - \frac{T}{4l} + \frac{(l-T)^2}{4lT} & : T \leq l < 2T \\ 1 - \frac{T}{L} & : l \geq 2T \end{cases} \qquad (2.12) \\
F_{L,diff}(l) &= \frac{1}{2}(F_{L,up} + F_{L,down,diff}) \\
&> \begin{cases} \frac{l}{4T} & : l < T \\ \frac{1}{2} - \frac{T}{4l} + \frac{l-T}{12T} & : T \leq l < 2T \\ \frac{1}{2} - \frac{T}{4l} & : l \geq 2T \end{cases} \qquad (2.13) \\
&< \begin{cases} \frac{l}{4T} & : l < T \\ \frac{1}{2} - \frac{T}{4l} + \frac{l-T}{12T} & : T \leq l < 2T \\ 1 - \frac{T}{4l} & : l \geq 2T \end{cases} \qquad (2.14)
\end{aligned}
$$

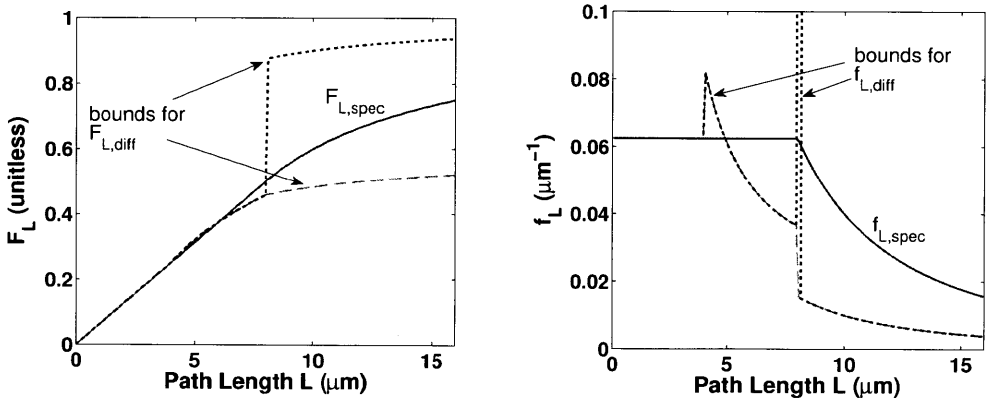

Figure 2-22: Cummulative distributions for path lengths assuming specular and diffusive reflection off of the gold contact are shown in (a), and the corresponding probability density functions are shown in (b). We bound the error due to neglecting path lengths greater than $2T$ in the diffusive reflection case by plotting the distribution functions with (black dotted lines) and without (red dashed lines) all of the missing probability at exactly $2T = 8\mu$m.

These cumulative distribution functions and their corresponding probability distribution functions are plotted for the case when T is equal to 4μm in Figure 2-22.

The expected value for extraction is then found by integrating extraction as a function of path length with the path length probability distribution function.

$$\begin{aligned} \langle \eta_e xt \rangle &= \int_0^\infty \eta_e xt(l) f_L(l) dl \\ &= \int_0^\infty e^{-\alpha l} f_L(l) dl \end{aligned} \tag{2.15}$$

where α is the material absorption averaged over the LED emission spectrum. In this case the value of α is taken to be 4000cm^{-1} [47]. The expected extraction efficiency considering lengths $0 < l < L$ is plotted in Figure 2-23. We see that any of the possible assumptions considered thus far lead to a net extraction between 14.6% and 16.2%. For simplicity we will use 15% as the expected value of extraction.

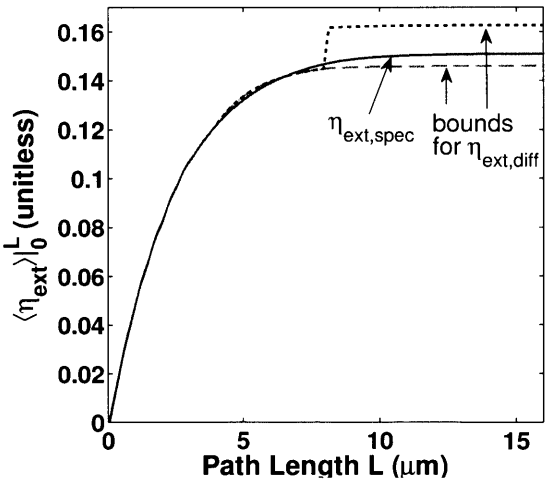

Figure 2-23: Expected net photon extraction efficiency $\langle \eta_{ext} \rangle$ as a function of the maxiumum path length considered. Path lengths greater than 8μm are shown to contribute insignificantly to extracted light.

The emission, re-absorption and subsequent re-emission of a photon in the active region of an LED is often called photon recycling [7, 60, 6, 13]. On net this process does not contribute to light emission or net recombination. Since light extraction is not simulated in our LED model it is not possible to include this effect self consistently. As a first order correction, we will reduce the bimolecular recombination coefficent of

GaInAsSb $B_{GaInAsSb}$ to equal $\langle \eta_{ext} \rangle B_{GaInAsSb}$. From a light emission standpoint this is correction is equivalent to the assumption that electron-hole pairs generated by photon re-absorption will all recombine non-radiatively. Since the modeled quantum efficiency of the LED21Sr is low in the bias range of interest ($\eta_Q < 3 \cdot 10^{-3}$ for no dopant diffusion), this is a reasonable assumption. Following the same line of reasoning we will reduce the bimolecular recombination coefficient in GaSb B_{GaSb} to zero, since the thick GaSb layers should permit very little photon extraction.

2.3.2 Simulating Device Characteristics

The last step in simulating the characteristics of an LED21Sr is to place the model in a simulated environment. In the case of modeling charge and energy transport, this amounts to setting realistic electrical and thermal boundary conditions. We will be studying the LED with the package held at a constant temperature and with an electrical bias across the anode and cathode enforced with a voltage supply. There are finite electrical and thermal resistances between the points at which temperature and voltage are controlled and the actual diode interfaces that correspond to the edges of the modeled structure. We will place the diode in an electrical and thermal circuit, as shown in 2-24 to account for these resistances. Doing so should allow for prediction of realistic experimental results through simulation. According to [1], the contacts on this LED are ohmic and each add a resistance of approximately 0.4Ω. Thus we will use an R value of 0.8Ω to account for the total series resistance. The experimental characterization results presented in Section 2.4 will show that this is very close to the measured series resistance value. The thermal resistance between the diode and the package is not given for this type of device, but based on other work thermally characterizing LED packaging [61] we assume that that R_{therm} has a value of approximately $10°KW^{-1}$.

Now that we have made adjustments to account for light extraction and placed appropriate boundary conditions on the device, we can simulate the LED21Sr. We sweep voltage bias as before, but we do so at elevated ambient temperatures so that we can see the effect of increased temperature on thermal pumping. The simulated

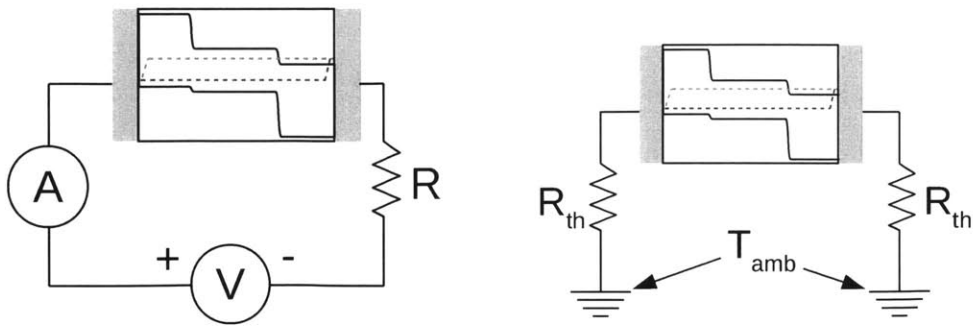

(a) (b)

Figure 2-24: Electrical (a) and thermal (b) circuit diagrams demonstrating how the environment is included in the simulation of LED characteristics.

device characteristics are shown in Figure 2-25.

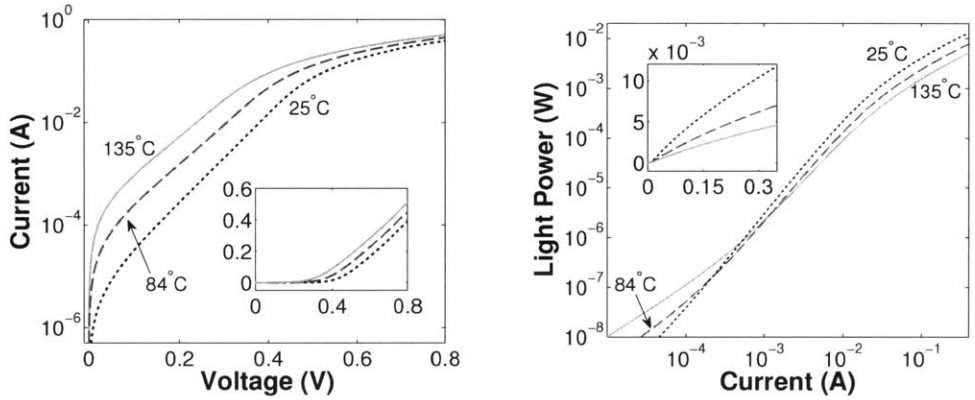

(a) (b)

Figure 2-25: Simulated I-V and L-I characteristics of the LED21Sr at three ambient temperatures. (a) shows the I-V curves on a semi-logarithmic scale and a linear scale in the inset and (b) shows the L-I curves on a logarithmic scale and a linear scale in the inset.

In Figure 2-26 η_Q and η are plotted as a function of current and light respectively at various temperatures. As before we see that the LED is predicted to achieve electroluminescent cooling at low bias. We see that the low bias quantum efficiency increases with temperature along with the light powers at which the η minimum and $\eta = 1$ are predicted.

The the predicted cooling power of the LED21Sr, defined here as the difference between optical power output and input electrical power $L - IV$, is plotted against

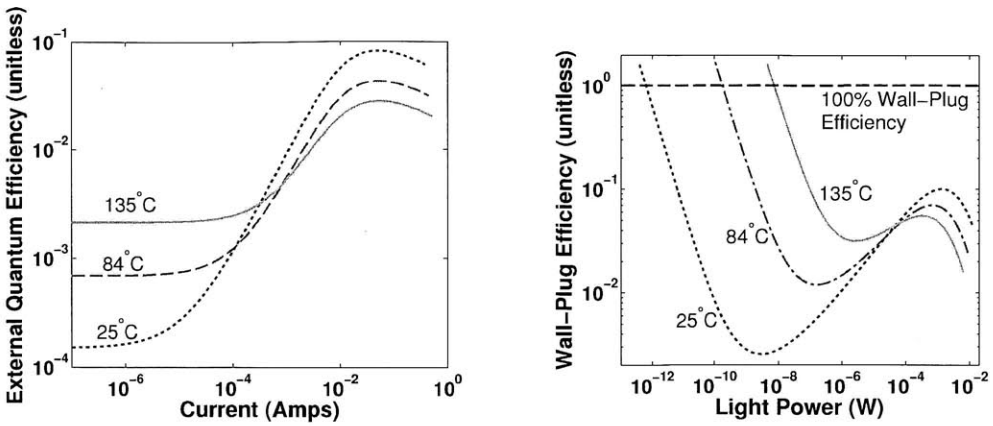

Figure 2-26: Simulated quantum and wall-plug efficiency as a function of bias for the LED21Sr at three ambient temperatures.

current in Figure 2-27. We see that although the efficiency of the LED diverges as the applied voltage goes to zero, the cooling power has a maximum value. Figure 2-28 shows the predicted temperature and energy flux profiles across the LED21Sr junction when it is operating at maximum cooling power at 135°C. We see that the electron and hole populations both cool near the heterojunctions due to Peltier exchange, but that the minimum calculated temperature in the device was approximately 2.5mK below the temperature at the boundaries. We note that only the electron and hole population temperatures are plotted because the heat capacities of these systems ($\frac{3}{2}nk_BT \approx \frac{3}{2}pk_BT \approx 4 \cdot 10^{-8}\mathrm{WK^{-1}cm^{-3}}$) are more than seven orders of magnitude smaller than that of the lattice ($\approx 1\mathrm{WK^{-1}cm^{-3}}$). Since these systems are tightly coupled by a 1ps energy relaxation time, spatial variation in lattice temperature corresponding to mK-scale variation in electron and hole temperatures is well below the numerical resolution of this calculation.

Although we have done our best to model the device characteristics of the LED21Sr based on parameters found in the literature, it is likely that these published parameters will not perfectly describe the device we are studying. Most of the experimentally determined parameters found in Table 2.1 were measured with devices grown by growth methods associated with low defect densities, while the LPE method used to grow LED21Sr usually leads to high defect densities. Thus we expect that the

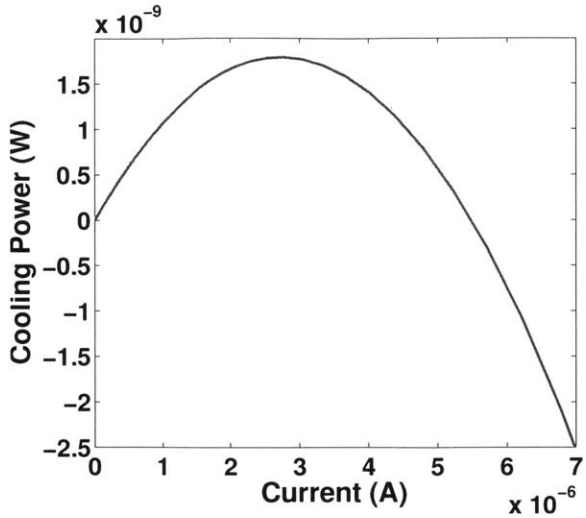

Figure 2-27: Simulated cooling power $L - IV$ of the LED21Sr for low-bias operation at 135°C.

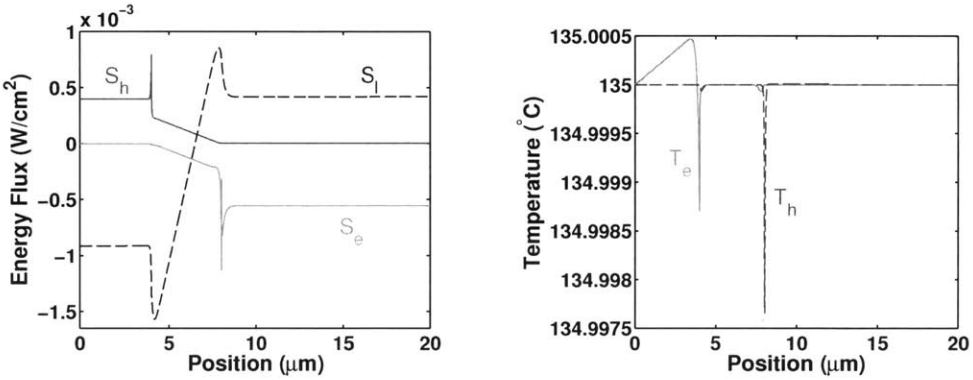

Figure 2-28: Spatial profiles of (a) Energy flux and (b) electron and hole temperature in the LED21Sr for operation at maximum cooling power at 135°C.

rate of trap-based SRH recombination in the LED21Sr may turn out to be slightly faster than suggested in this model. We also know that the series resistance caused by the contacts can be easily probed by measuring the I-V characteristic of the LED at high bias. Once we have experimental I-V data the SRH recombination lifetime τ_{SRH} and the series resistance R will be used as fitting parameters to match the simulated electrical properties to the measured data. Since the efficiency with which light is transfered to active region of the photo-detector once it escapes the active region of the LED is not known, measured light power curves will be used to determine a

collection efficiency by which to reduce the simulated light power. These will be the only three fitting parameters used to model the LED21Sr.

2.4 Experimental Device Characterization

We would like to compare our numerical model for the LED21Sr with experiment. A block diagram describing the experimental setup is shown in Figure 2-29 and a photograph of the setup is shown in Figure 2-30. This setup provides control over the voltage bias placed on the LED as well as the temperature of the LED package. The thermally isolated portion of the experiment consists of the LED21Sr, a resistive cartridge heater and two thermistors inside a copper cylinder. Thermal paste is used to thermally couple the LED and heater to the copper cylinder. One thermistor is placed in contact with the LED, while the other is placed in contact with the heater. One Wavelength Electronics LFI-3751 Temperature Controller is used with the heater and the thermistor on the heater to bring the entire thermally isolated setup to elevated steady-state temperatures, while another LFI-3751 is used with the second thermistor to measure the LED temperature. Voltage bias and current measurement are achieved with a Keithley 2635A SourceMeter. Light Power is transduced into a current signal using a Hamamatsu G5853-23 indium gallium arsenide (InGaAs) *p-i-n* photo-diode, and that current signal is then transduced into a voltage signal using a Stanford Research Systems SR570 Low-Noise Current Pre-amplifer. Note that the photo-diode is operated with zero reverse bias (photovoltaic mode). This is discussed in discussed in Section 3.3.1. Finally the voltage signal is measured using an Agilent 34401A Digital Multimeter. This setup allows for measurement of injected current and emitted light power as a function of applied voltage bias and temperature.

Although evidence of thermal pumping of LEDs is predicted by simulation to be more easily observed (i.e. at higher power) as the LED temperature is increased, there is a maximum temperature above which the LED21Sr fails. Two main types of high-temperature failure have been observed. In some cases LEDs became open circuits at temperatures above approximately 120°C. In devices where this did not

occur, an irreversible reduction in LED quantum efficiency was observed when the diodes were brought above approximately 140°C. In these cases the LED I-V curves measured after the device is taken to a lower temperature are seen not to match those taken at the same temperature before exceeding 140°C. This indicates that the device, not just the extraction efficiency, is irreversibly changing. While the exact failure modes are not known, they likely result from thermal expansion of packaging materials and melting of solder used to contact the LED. Although the spectrum of one LED was be measured at temperatures up to 195°C, LED efficiency will only be studied at temperatures up to 135°C to ensure that measurements are repeatable.

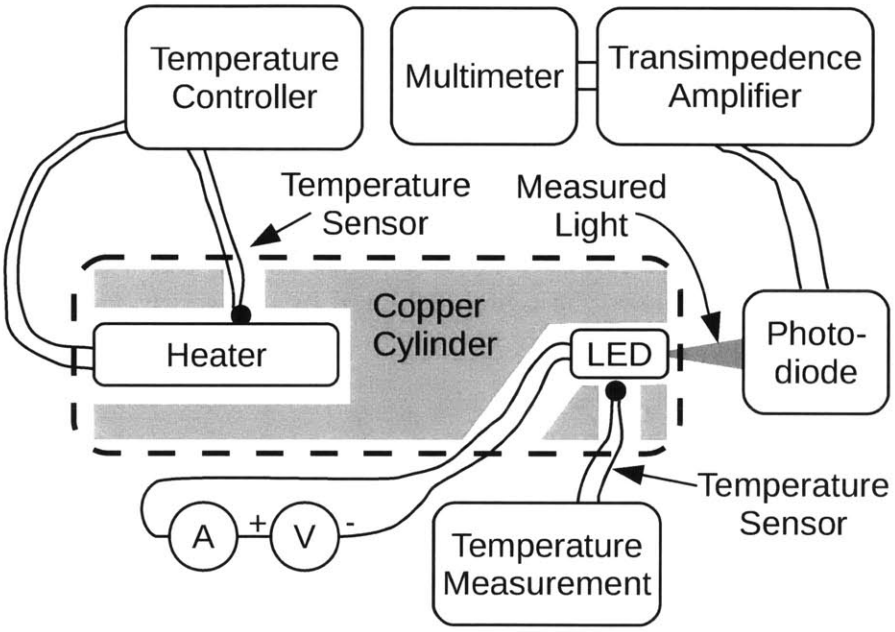

Figure 2-29: Block diagram describing the experimental setup used to characterize the LED21Sr. The dashed line indicates the portion of the setup that is brought to elevated temperatures.

I-V data measured at room temperature and two elevated temperatures is plotted with simulated characteristics at the corresponding temperatures in Figure 2-31. In Figure 2-31 (a) we see that the simulated IV characteristic predicts less current than is observed experimentally. Since SRH recombination in the active region dominates at low bias, we can adjust the SRH lifetime for GaInAsSb as a fitting parameter to improve this match. We also note a slight mismatch in the series resistance seen

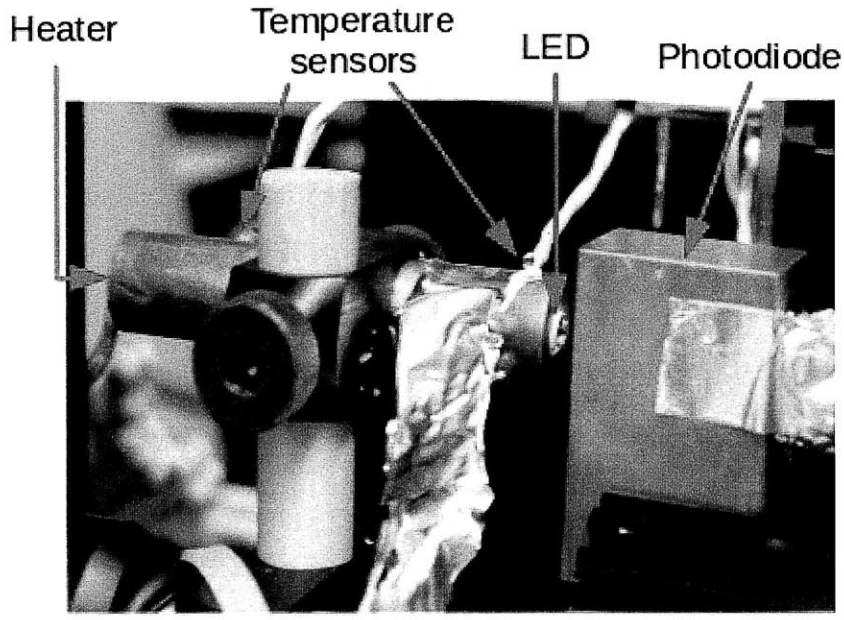

Figure 2-30: Photo of the experimental apparatus used to characterize the LED21Sr.

at high bias, which will be corrected by changing the series resistance from 0.8Ω to 0.779Ω. Figure 2-31 (b) shows the match achieved by decreasing τ_{SRH} from 125ns to 95ns.

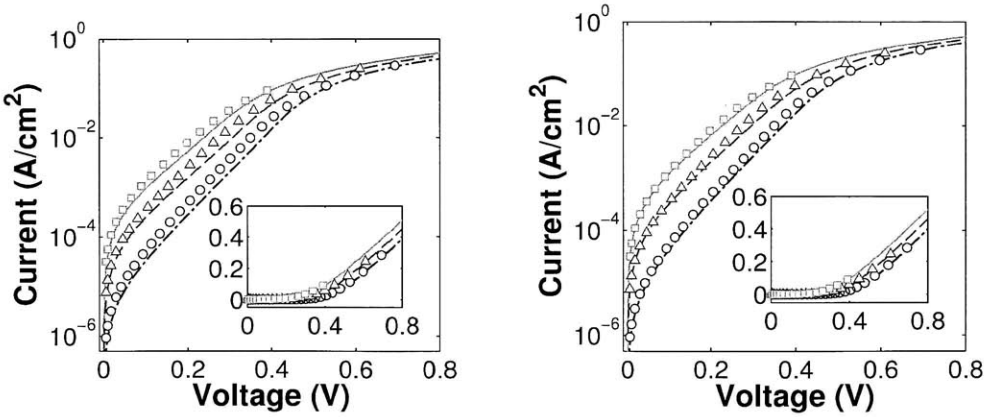

Figure 2-31: Simulated (lines) and measured (markers) I-V characteristics of the LED21Sr. (a) shows the simulation data before the SRH recombination lifetime in the active region and the series resistance were used as fitting parameters to match the curves on a semi-logarithmic scale and a linear scale in the inset. (b) shows the result of the fit on a semi-logarithmic scale and a linear scale in the inset.

Before characterizing the LED optically we must first consider the overlap between the emitted spectrum of the LED and the spectral responsivity of the photo-diode used to measure optical power. The spectrum emitted by the LED was measured with the same setup as shown in Figure 2-29, except with the photo-diode replaced by a Fourier transform infrared (FTIR) spectrometer. Spectra measured from the LED at three different temperatures are shown in Figure 2-32 (a), and their overlap with the spectral responsivity of the photo-diode [62] is shown in Figure 2-32 (b). We approximate the spectral responsivity of the photo-diode as the piecewise function shown in Figure 2-33 (a) and calculate the average responsivity of the photo-diode in Amperes per Watt optical power as a function of temperature using LED spectra measured at 15 temperatures between 25°C and 195°C (shown in Figure 2-33 (b)). To make predictions of measured optical power at different temperatures, we reduce the predicted total optical power by the ratio of average responsivity to the maximum responsivity of 1.3A/W.

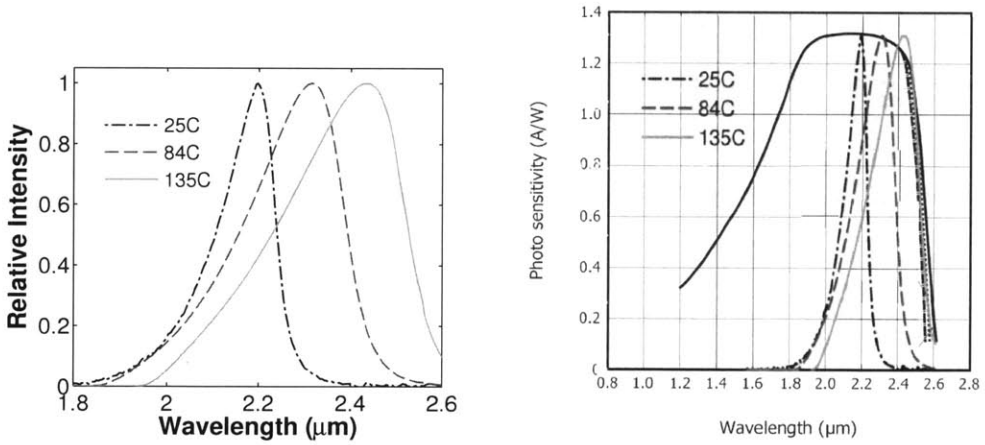

(a) (b)

Figure 2-32: (a) Emission spectra measured from the LED21Sr at three different temperatures. (b) the same emission spectra shown in (a) overlaid onto the spectral responsivity of the indium gallium arsenide (InGaAs) photo-diode used to measure optical power.

We must also establish a floor for valid light power measurements set by the noise present in the measurement system. This noise floor was determined by taking many measurements with the LED unbiased after each bias sweep and looking at their mean

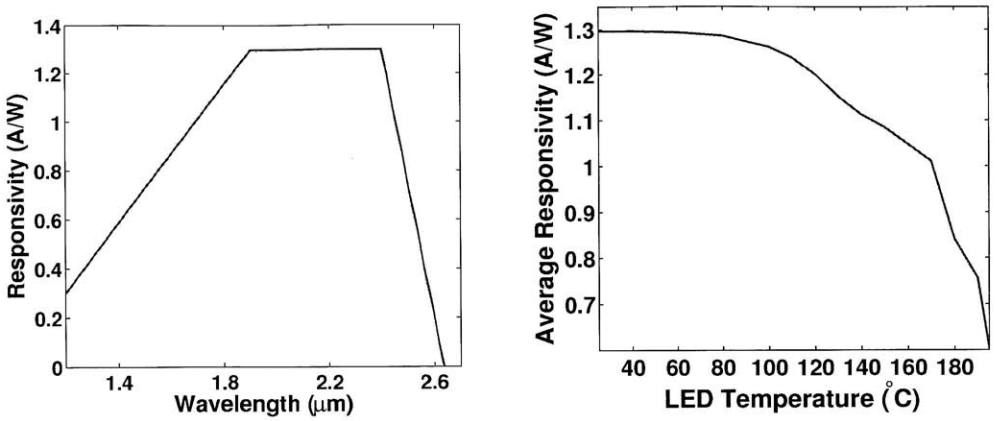

(a) (b)

Figure 2-33: (a) Piecewise approximation of the photo-diode spectral responsivity used to calculate the average responsivity over the LED21Sr emission spectrum. (b) Calculated average responsivity to the LED21Sr spectrum as a function of the LED21Sr's temperature.

and standard deviation. The mean of these measurements was subtracted from the measured light power values from that sweep and the standard deviation was taken to be the light power uncertainty. Light power uncertainties measured at the end of bias sweeps performed with the LED at 12 temperatures between 25°C and 125°C are plotted in Figure 2-34. Noise in the light power signal is seen to be approximately independent of LED temperature. This indicates that the noise is a result of a thermal process somewhere in the measurement apparatus that is not brought to elevated temperatures. It seems likely that this thermal noise originates either in the photo-diode or the transimpedance amplifier, and that the slight variations in the measured noise at different LED temperatures shown in Figure 2-34 result from minor variations in the temperature of either the photo-diode or the transimpedance amplifier. Measured light data is cut off when the uncertainty approaches 10% of the measured value, thus establishing the noise floor of approximately 100nW. Light power data at levels below this value will not be considered in this comparison.

A comparison of measured and simulated L-I curves is shown in Figure 2-35. Figure 2-35 (a) shows the measured data with simulated L-I curves that are only reduced to account for the spectral response of the detector. Figure 2-35 (b) shows the

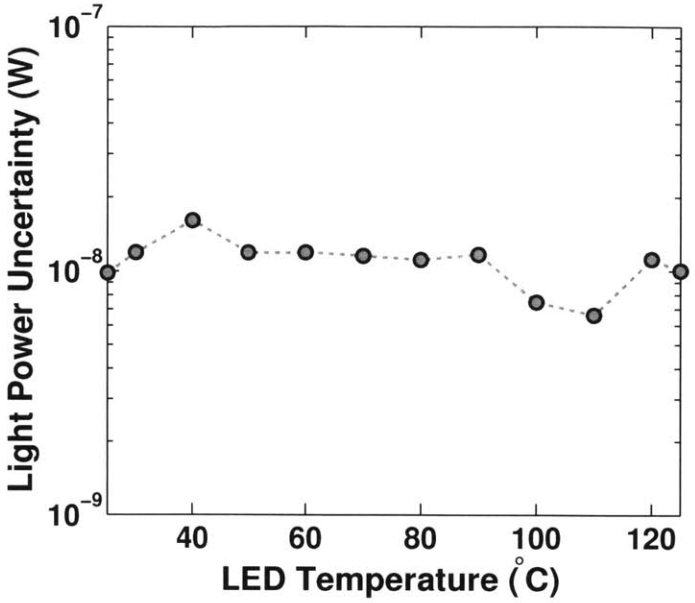

Figure 2-34: Mean and standard deviation of the light power signal measured while the LED21Sr was unbiased plotted as function of the LED21Sr temperature.

same measured data compared with simulated curves adjusted with an 14% collection efficiency. This collection efficiency acts as a fitting parameter accounting for light that exits the active region of the LED but is not absorbed in the active region of the detector.

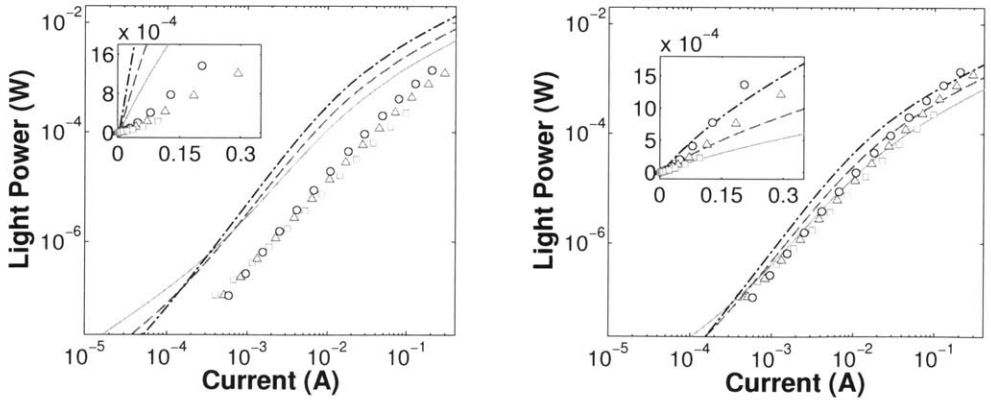

(a) (b)

Figure 2-35: Simulated (lines) and measured (markers) L-I characteristics of the LED21Sr. (a) shows the simulation data before the simulation data was reduced by a collection efficiency fitting parameter on a logarithmic scale and a linear scale in the inset. (b) shows the result of the fit on a logarithmic scale and a linear scale in the inset.

As seen in Figure 2-36, the light power noise floor prevents us from observing clear signatures of thermally assisted pumping of the LED21Sr. The measured data does not reach light levels where the external quantum efficiency approaches a low-bias minimum. As a result none of the measurements demonstrate improved wall-plug efficiency at low bias, and only the 135°C data shows a low-bias wall plug efficiency that is not significantly lower than the maximum high-bias efficiency. However some aspects of the experimental results are encouraging. We do see that external quantum efficiency falls with increasing temperature at high bias and rises with increasing temperature at low bias. We also see a wall-plug efficiency minimum at low bias at 135°C. Both of these features are predicted in the model. If the wall-plug efficiency continues to rise as predicted by numerical simulation, wall-plug efficiency in excess of 100% (and thus electroluminescent cooling) should be observable at approximately 100pW. This will require that the noise optical noise floor be lowered by at least three orders of magnitude.

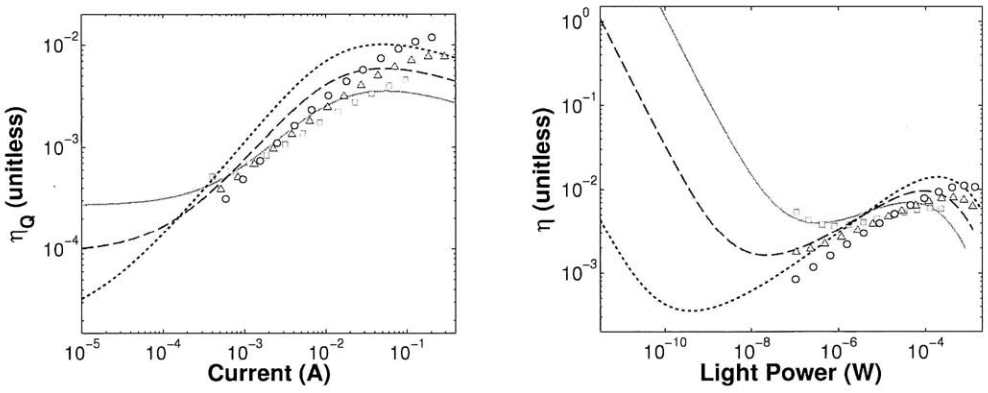

Figure 2-36: Simulated (lines) and measured (markers) quantum (a) and wall-plug (b) efficiency characteristics of the LED21Sr.

2.5 Summary and Conclusions

In Section 2.1 we introduced the LED21Sr as a useful device for studying thermal pumping in LEDs. This device was chosen because of its small active region band

gap, the fact that it was rated to survive to elevated temperatures and the fact that its structure is published, making it accessible for numerical modeling. In Section 2.2, a model for the charge and energy transport occurring in across a *p-i-n* double heterojunction diode was developed in four steps and then applied to model the LED21Sr. In the development of this model we saw that Peltier energy exchange within an LED can be modeled with hydrodynamic transport in Sentaurus, while energy exchange at the contacts cannot. Nonetheless we are able to simulate the effects of thermal pumping at low bias as and the dependence of these effects on device temperature. Predictions of the power levels at which electroluminescent cooling should be observable were given. Finally in Section 2.3 an experimental apparatus for characterizing the LED21Sr was introduced and collected data was compared with simulation results. Experimental results were used to add three fitting parameters to the model. Although some evidence of thermal pumping was seen at low bias and high temperature in the LED21Sr, the optical noise floor and maximum achievable temperature prevented the observation of electroluminescent cooling or even high efficiency. While light-power emission from an LED in excess of input electrical power is predicted in the hydrodynamic model presented, net energy flux into the device is not demonstrated by the model due to the lack of Peltier exchange at the modeled device contacts. To experimentally observe electroluminescent cooling in the LED21Sr the optical noise floor will need to be reduced to below 100pW. To this end, we will explore the use of lock-in amplification in Chapter 3.

Chapter 3

LED Characterization with Lock-In Measurements

3.1 Chapter Overview

The modeling results presented in Chapter 2 suggest that electroluminescent cooling should be measurable in the low-bias regime of a mid-IR LED at elevated temperature. Comparison between model and experiment with the LED21Sr suggests that this measurement will require the ability to measure optical power signals below 100pW. The noise present in a DC optical power measurement was shown to introduce significant (¿10%) uncertainty into power signals below approximately 100nW. In this Chapter we will seek to sufficiently lower the limit of detection of our optical power measurement system such that detection of electroluminescent cooling can be achieved. To do so we will attempt to reduce the noise power present in our measured signal by modulating the optical power output from the LED21Sr and performing phase-locked power measurement over a narrow signal bandwidth centered around the frequency of modulation. This synchronous detection technique, known as lock-in measurement will be shown to lower the optical power detection limit sufficiently to observe the effects of thermal pumping in the LED21Sr including electroluminescent cooling.

In Section 3.2 the principle of lock-in measurement will be explained. In Section 3.3 the apparatus used to characterize the LED21Sr at low bias will be described.

Challenges encountered while designing this apparatus will also be discussed. In Section 3.4 the new limit of optical power detection achieved with this apparatus will be characterized. Results of L-I-V-T characterization of the LED21Sr using lock-in measurement including evidence of electroluminescent cooling will be presented in Section 3.5. Finally a Chapter summary and conclusions will be given in Section 3.6.

3.2 Lock-In Measurement

For the purpose of optimizing the power efficiency of a light source for a measurement system, it is necessary to determine the minimum light power required for a usable signal. Generally there is some power below which the signal to be measured is lost in the presence of noise that is inherent to the system. Noise in a signal is usually associated with random processes including thermal excitations and randomly distributed arrivals of quanta such as electrons and photons. Usually noise signals in electronic systems are most spectrally dense near zero frequency because of slow averaging times associated with thermal motion of charged particles [5]. This effect is known as $1/f$ noise.

One method for recovery of a signal in the presence of significant noise is frequency and phase sensitive detection, known as lock-in measurement. In this scheme an excitation signal $e(t)$ modulates the dynamic quantity to be measured at a frequency ω_0.

$$e(t) = A\sin(\omega_0 t + \phi_1) \tag{3.1}$$

A unity amplitude reference signal $r(t)$ that is frequency and phase matched to $e(t)$ is also generated for use in lock-in process.

$$r(t) = \sin(\omega_0 t + \phi_1) \tag{3.2}$$

The system is then probed and a signal $s(t)$ which contains both the desired signal at the excitation frequency and a noise component $n(t)$ is measured.

$$s(t) = B\sin(\omega_0 t + \phi_2) + n(t) \tag{3.3}$$

Note that the signal component of $s(t)$ may have a constant phase offset from the excitation signal $\phi_2 - \phi_1$ due to reactive elements in the system being probed. Also note that $n(t)$ is a random process whose power spectral density is generally non-zero at across all frequencies. The next step in the lock-in process occurs when $s(t)$ is multiplied by $r(t)$.

$$\begin{aligned} s(t)\cdot r(t) &= [B\sin(\omega_0 t + \phi_2) + n(t)]\cdot[\sin(\omega_0 t + \phi_1)] \\ &= \frac{B}{2}\cos(2\omega_0 t + \phi_1 + \phi_2) \\ &\quad + \frac{B}{2}\cos(\phi_1 - \phi_2) + n(t)\cdot\sin(\omega_0 t + \phi_1) \end{aligned} \tag{3.4}$$

This multiplication process generates a DC component that is proportional to the desired signal amplitude B and modulates low frequency noise away from baseband. A narrow-band, low-pass filter is applied to the product of $r(t)$ and $s(t)$, leaving only the DC component $\frac{B}{2}\cos(\phi_1 - \phi_2)$. Typically a lock-in system adds an adjustable time delay to the reference signal so that the reference phase ϕ_2 can matched to the excitation phase ϕ_1. When the ϕ_2 is equal to ϕ_1 then

$$\frac{B}{2}\cos(\phi_1 - \phi_2) = \frac{B}{2} \tag{3.5}$$

and the output of the lock-in amplifier is maximized as

$$\begin{aligned} LPF * [s(t)\cdot r(t)] &= \frac{B}{2} + LPF * [n(t)\cdot\sin(\omega_0 t + \phi_1)] \\ &\approx \frac{B}{2} + \int_{-\omega_c}^{\omega_c} N(j\omega)\cdot\frac{1}{2i}e^{j\phi_1}[e^{j\omega_0 t} - e^{-j\omega_0 t}]d\omega \\ &= \frac{B}{2} + \int_{\omega_0-\omega_c}^{\omega_0+\omega_c} Im[e^{j\phi_1}N(j\omega)]d\omega \\ &\approx \frac{B}{2} + 2\omega_c Im[e^{j\phi_1}N(j\omega_0)] \end{aligned} \tag{3.6}$$

where ω_c is the cutoff frequency of the low-pass filter and $N(j\omega)$ is the Fourier transform of the autocorrelation of the noise $n(t)$. This process of selecting a very narrow band of frequencies around the excitation frequency ω_0 and counting only the signal portion in that band that oscillates with a constant phase offset from the excitation signal, $\phi_2 - \phi_1$, is called phase sensitive detection (PSD). PSD Through PSD the functional relationship $B(A)$ can be measured against a noise background much smaller than the noise present in a DC measurement.

One example of a case in which a signal must be measured amidst large background noise is infrared absorption spectroscopy. Water (H_2O), oxygen (O_2), o-zone (O_3), carbon dioxide (CO_2), methane (CH_4) and many other gases of interest have strong absorption peaks in the infrared[63, 64]. In the presence of significant background noise, a lock-in measurement may allow a system to resolve small changes in concentrations of these gases that are not discernible with a DC measurement. This is especially relevant in high temperature environments where the power of background infrared radiation becomes large.

3.3 Final LED Characterization Apparatus

We now modify the experimental apparatus used for DC L-I-V-T characterization of the LED21Sr in Chapter 2 to take advantage of lock-in. The goal of this modification is to reduce the system's optical power limit-of-detection (LOD) by at least three orders of magnitude from 10^{-7}W to less than 10^{-10}W. We must first adjust our electrical bias scheme. Based on the device modeling in Chapter 2, we expect that we will need to source a modulated bias of approximately 10^{-4}V and 10^{-7}A to achieve the desired optical power levels. Direct application of a voltage signal of this amplitude is not feasible with standard equipment [65] because thermal noise present in the amplifiers used in a function generator causes uncertainty in the output signal on this order [5]. Thus we choose to apply a current bias. This is achieved by applying a voltage bias to a series load comprised of the LED and a known resistance R that is much larger than the LED. Since the load seen by the function generator is dominated by

the constant series resistance R, when a voltage signal of amplitude V is applied a current signal approximately $\frac{V}{R}$ in amplitude flows through the LED. We perform a lock-in measurement of the voltage across the LED to find the exact amplitude of the applied electrical bias signal. We call this signal V_{LED}. Knowing V, R and V_{LED}, we can also solve for the amplitude of the applied current signal

$$I_{LED} = \frac{V - V_{LED}}{R} \tag{3.7}$$

R values of 5kΩ, 50kΩ, 500kΩ and 5MΩ can be used with voltage signal amplitudes 20mV$\leq V \leq$10V to apply currents 4nA$\leq I_{LED} \leq$2mA. As shown in Section 3.4, this current range is sufficient for reaching the light power limit of detection and overlapping with the DC data presented in Chapter 2. To measure optical power output from the LED, we perform a lock-in measurement on the voltage signal that results from output transimpedance amplification of the photo-current output from the photo-diode I_{opt}. Transimpedance amplification of this signal involves two daisy-chained amplifiers with a net gain of 10^7. The temperature control portion of this LED characterization apparatus is the same as in Chapter 2. A block diagram describing the lock-in characterization apparatus is shown in Figure 3-1.

A sinusoidal I_{LED} signal would result in a V_{LED} with significant power density at higher harmonics of the fundamental frequency because the non-linearity of the LED's I-V characteristic. Thus we choose to bias the LED with an on-off square wave modulation signal, pushing all non-linearities to the high harmonics associated with the rising and falling edges of the square wave. To choose a modulation frequency, we consider the spectral noise density and gain-bandwidth of the Stanford Research Systems SR570 transimpedance amplifier shown in Figure 3-2. The $^1/_f$ noise present in the system is seen to fall below the background thermal noise at approximately 100Hz for all gain settings. Thus to ensure avoiding $^1/_f$ noise we would like to operate at least 1kHz. Although gain bandwidth curves are not plotted for all gain settings in Figure 3-2 (b), we can surmise that at 1kHz transimpedance gain settings greater than 10^6 (1μA/V) may begin to roll off, and that for signal frequencies greater than

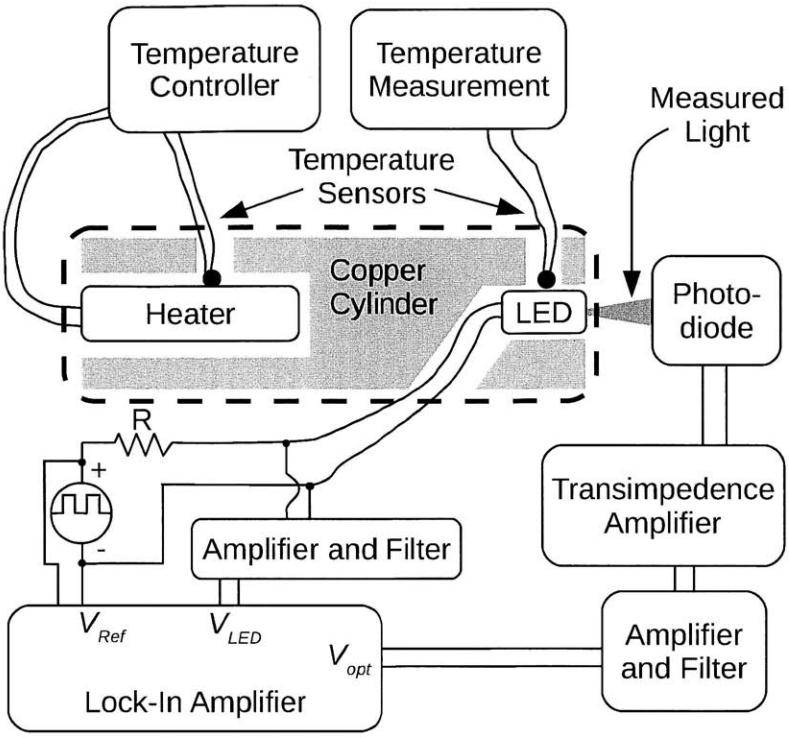

Figure 3-1: Block diagram describing the lock-in based LED characterization apparatus. This system is very similar to the apparatus used for DC characterization in Chapter 2 (shown in Figure 2-29), except that the electrical bias is now an on-off square wave current source and the optical power is measured using lock-in.

1kHz an even lower gain setting must be used to avoid roll-off. Thus we will bias the LED with a 1kHz on-off square wave current signal of varied amplitude and amplify I_{opt} with a transimpedance gain of 10^6V/A. We also add a second gain stage along optical power signal path with a gain of 10. This daisy-chain of amplification applies a net transimpedance gain of 10^7V/A to I_{opt}. Since the responsivity of the photo-diode detector is approximately 1.3A/W for the emission spectrum of LED, V_{opt} corresponding to a measured optical power signal with amplitude 10^{-10}W will be on the order of 1mV.

Although the lock-in amplifier acts as a very narrow band-pass filter around the frequency of modulation, lock-in filtering only takes place after the input analog signal is converted to a digital signal by an analog to digital converter (ADC). Filtering in the pre-lock-in amplification stages prevents overloading of the input of the ADC.

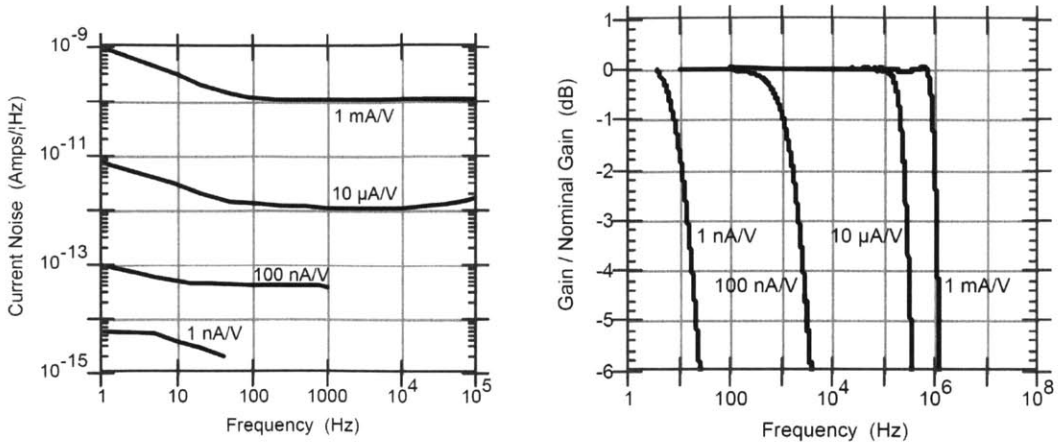

(a) (b)

Figure 3-2: (a) Plot of the spectral density of current noise in the SR570 transimpedence amplifier. (b) Plot showing the frequencies at which transimpedence gain rolls off for different gain settings on the SR570 transimpedence amplifier. Both plots taken from [4].

To this end we apply a single pole (6dB per decade) high-pass filter with a corner frequency of 30Hz and a three pole (18dB per decade) low-pass filter with a corner frequency of 30kHz using the amplifiers along the optical power signal pathway. We also add a gain stage in the V_{LED} signal pathway. This will be used to ensure that the amplitude of V_{LED} at the input to the lock-in amplifier is greater than 1mV. The gain in the V_{opt} and V_{LED} signal pathways is characterized at 1kHz in Figure 3-3. The V_{opt} pathway gain was characterized for input signals with amplitudes ranging from 3nA-300nA. We see that it is nearly ideal for a wide range of inputs and that non-ideality only appears when the output signal is on the order of 2V. We supplied a 1mV input signal to the V_{LED} amplifier by biasing the LED with a current signal corresponding to a 1mV amplitude V_{LED}. This was verified by measuring V_{LED} using the lock-in amplifier without external amplification. Then the V_{LED} signal was run through the external amplifier and several gain settings were tested. We see approximately ideal gain for gain settings between 1-1000. Non-ideality is only seen for outputs greater than approximately 500mV. We assume that for neither of these gain stages will become non-linear for signals of smaller amplitude than those used in these measurements. Based on these measured gain characteristics at 1kHz, we do

not expect significant distortion over the signal range of interest.

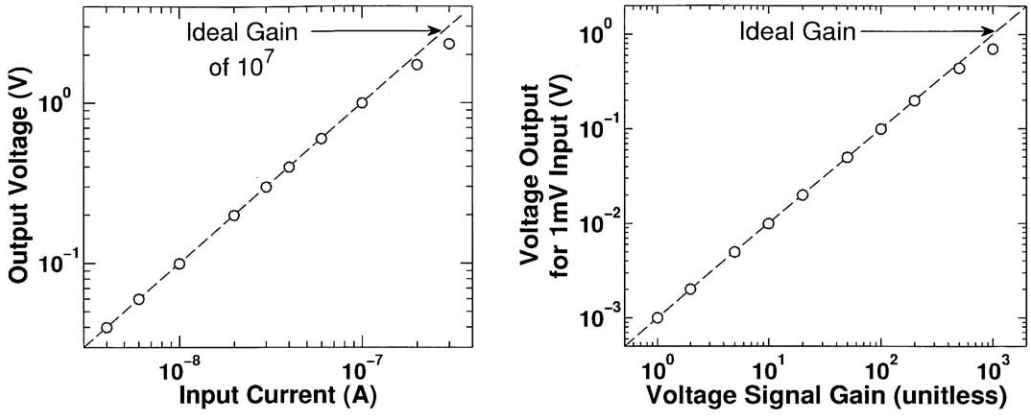

Figure 3-3: Characterization of (a) the transimpedance gain used to transduce photocurrent into a voltage signal at 10^7 and (b) the gain stage used to amplify the voltage across the LED before lock-in for gains from 1 to 1000 and an input signal of 1mV. Both characterizations were performed at 1kHz using the lock-in amplifier. We see some gain saturation for output signals greater than approximately 2V for the transimpedance amplifier or 500mV from the voltage signal amplifier.

3.3.1 Challenges Faced in Measurement

Having described the finalized measurement apparatus for low-power LED L-I-V-T characterization, it is also of interest to describe some of the pitfalls that were encountered during the design and realization process. Two of these, namely reverse biasing the photo-diode and application of a voltage bias signal with sub-millivolt amplitude, have already been alluded to. The other two issues are related to temperature measurement and control.

We initially attempted to measure optical power using the Hamamatsu G853-23 with a 1V reverse bias applied, which is given as the standard operating condition for the device [62]. We saw that shot noise in the photo-diode current resulting from the reverse bias greatly increased the noise equivalent power in our frequency range of interest and thus raised our limit of optical power detection. We learned that application of a reverse bias to this type of photo-diode is only necessary to ensure

linear responsivity for signals at frequencies or powers much greater than those we were measuring [63]. Thus we began to use our photo-diode with zero applied bias, as a photovoltaic detector.

At first we attempted to supply and on-off voltage bias signal to the LED for the purpose of lock-in measurement. Since our function generators are limited to 10mV signal amplitudes [65], we initially attempted to apply an inverse gain of 10^{-2} between the function generator output and the LED using a single-stage amplifier circuit on a bread board. This solution was shown to introduce significant noise into the LED bias signal and raise the optical power limit of detection. Although function generators that can output μV scale signals are available [66], we found that the approximate current signal bias scheme described above was more quickly realized and allowed for optical power detection limited only by current noise intrinsic to the photo-diode (shown below).

We also encountered two significant issues related to temperature measurement and control. The first generation of this measurement apparatus included only one thermistor. This thermistor was placed on the LED and was used both to measure the temperature of the LED and for feedback to the temperature controller. With this temperature control scheme we were unable to avoid temperature oscillations, which had amplitudes of approximately 5°C when the target temperature was greater than 120°C. We realized that this was a result of the long thermal time constant associated with the thermal impedence between the sensor and the heater and the thermal capacitance of the copper cylinder. To abate this issue we added a second temperature sensor in direct contact with the heater for tighter temperature control, while continuing to measure LED temperature directly on the surface of the LED package surface. We also realized that even with thermal paste coupling the LED temperature measurement thermistor to the LED, the measured temperature would increase by several degrees if the thermistor was pressed against the LED. The difference between measured temperatures with and without pressured applied increased linearly from 0°C to 8°C as the LED temperature was increased from broom 25°C to 135°C, indicating that a significant thermal impedence between the sensor and the LED. We

minimized the thermal impedence by adding a clamp to press the thermistor against the LED package.

3.4 Limit of Optical Power Detection

Now that we have a method for biasing the LED and characterized gain along the V_{opt} and V_{LED} signal pathways, we seek to establish the optical power LOD of our measurement system. We take light power signal measurements with no bias signal applied to the LED with the photo-diode at room temperature and with the photo-diode cooled to -21°C. In this measurement, a 1s time constant was used for the 12dB per decade digital band-pass filter that is implemented by the lock-in amplifier, corresponding to a noise bandwidth of approximately 250mHz. The results of these measurements are shown in Figure 3-4. We notice two things from this data. First, the spread of the measured values for no signal input is significantly dependent on the photo-diode temperature. This indicates that thermal noise in the photo-diode, which is given by the manufacturer to be approximately $16\text{pW}/\sqrt{\text{Hz}}$ [62], is setting the LOD of our detection system. Secondly we notice is that the noise is not centered around the origin. These offsets result from crosstalk between the signal and the reference signal which can happen both outside of and within the lock-in amplifier [67].

So that we can account for offsets present in our measurements, we will take measurements with no bias signal applied to the LED (zero-signal measurements (X_{Zi}, Y_{Zi})) each time a signal is applied. Each measurement will consist of 10 zero-signal measurements taken before the bias signal is applied to the LED , 10 measurements with a bias signal applied to the LED (X_i, Y_i), and 10 more zero-signal measurements after the bias signal has been turned off. Each measured data point can be considered in Cartesian coordinates (X, Y) or polar coordinates (ρ, θ). Following the strategy employed by the lock-in amplifier manufacturers [67], the offset will be dealt with in Cartesian coordinates and then the signal will be considered in polar coordinates. The average Cartesian coordinates of the zero-bias measurements

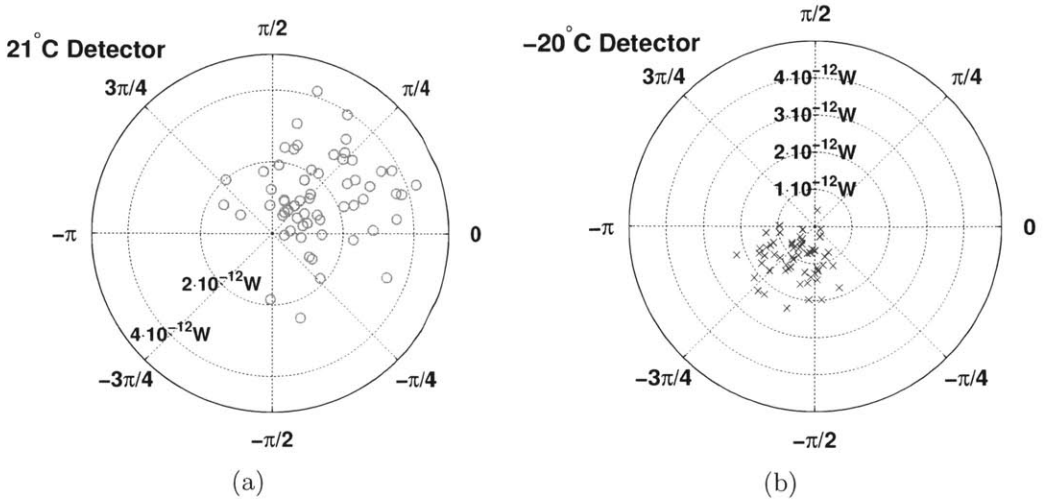

Figure 3-4: Noise measured with the photodiode detector at (a) 21°C and (b) -20°C. We see that the noise in the measured optical power signal decreases substantially. This indicates that thermal noise in the photodiode [5] sets the optical power detection limit of this measurement apparatus.

$(\langle X_Z \rangle, \langle Y_Z \rangle)$ will be taken to be the true origin of the polar measurement, and all data points measured with the bias signal on will be corrected so that they are referenced to this point.

$$(X_i', Y_i') = (X_i - \langle X_Z \rangle, Y_i - \langle Y_Z \rangle) \tag{3.8}$$

Next the average phase angle $\langle \theta' \rangle$ of the adjsuted data points is calculated.

$$\langle \theta' \rangle = \arctan \frac{\langle Y' \rangle}{\langle X' \rangle} \tag{3.9}$$

The the line from the origin to each adjusted point is then projected onto the radial line associated with $\langle \theta' \rangle$ and the length of this projection is taken to be the signal magnitude for that data point ρ_i.

$$\rho_i = X' \cos\langle \theta \rangle + Y' \sin\langle \theta \rangle \tag{3.10}$$

The mean of these magnitudes $\langle \rho \rangle$ is taken to be the measured value, and the standard deviation σ_ρ

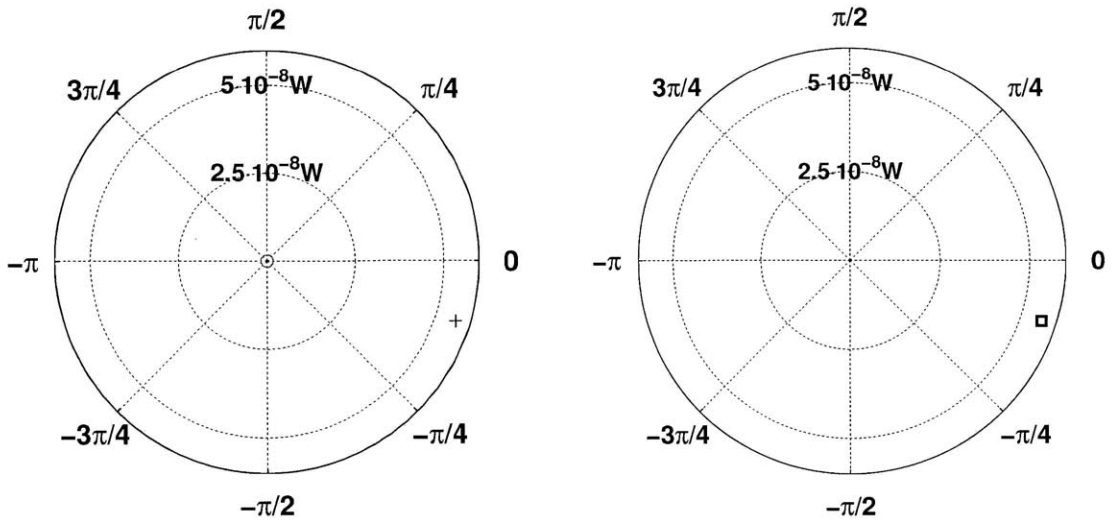

Figure 3-5: Optical power signal with SNR $\gg 1$ with the detector at -20°C. In (a) the blue crosses indicate (X_i, Y_i) values and red circles indicate (X_{Zi}, Y_{Zi}) values. In (b) the black square shows $(\langle\rho\rangle, \langle\theta'\rangle)$. For a signal to noise ratio this large (X_{Zi}, Y_{Zi}) are indistinguishable from $(\langle\rho\rangle, \langle\theta'\rangle)$ on a polar plot and thus are not shown. This ceases to be true for smaller SNR's. See Figures 3-6 and 3-7.

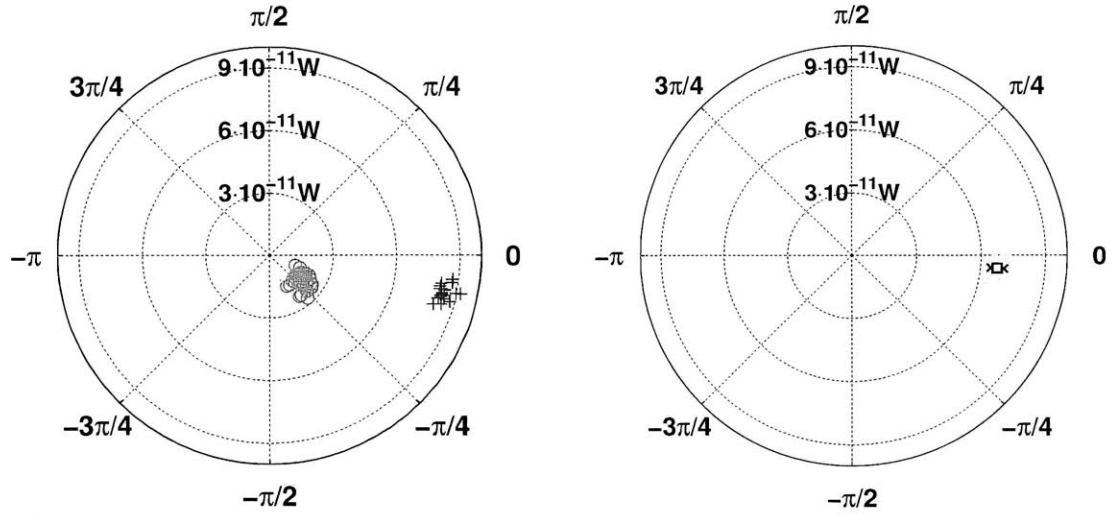

Figure 3-6: Optical power signal with SNR ≈ 10 with the detector at -20°C. In (a) the blue crosses indicate (X_i, Y_i) values and red circles indicate (X_{Zi}, Y_{Zi}) values. In (b) the green crosses show the corresponding (X', Y') values, the black square shows $(\langle\rho\rangle, \langle\theta'\rangle)$, and the black x's indicate $(\langle\rho\rangle \pm \sigma_\rho, \langle\theta'\rangle)$.

$$\sigma_\rho = \langle \rho^2 \rangle - \langle \rho \rangle^2 \tag{3.11}$$

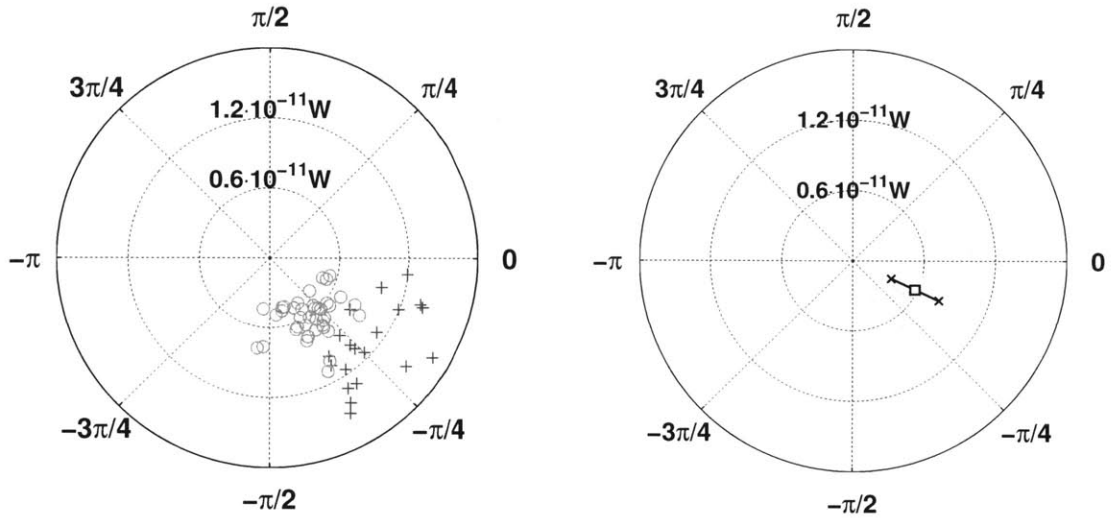

Figure 3-7: Optical power signal with SNR ≈ 1 with the detector at -20°C. In (a) the blue crosses indicate (X_i, Y_i) values and red circles indicate (X_{Zi}, Y_{Zi}) values. In (b) the green crosses show the corresponding (X', Y') values, the black square shows $(\langle \rho \rangle, \langle \theta' \rangle)$, and the black x's indicate $(\langle \rho \rangle \pm \sigma_\rho, \langle \theta' \rangle)$.

This process of removing the zero offset $(\langle X_Z \rangle, \langle Y_Z \rangle)$ and calculating signal magnitude $\langle \rho \rangle$ and uncertainty σ_ρ is shown for signals with signal to noise ratios (SNRs) of approximately 10^4, 10, and 1 are shown in Figures 3-5, 3-6, and 3-7 respectively. The uncertainty in lock-in optical power measurements is approximately 5pW, meaning that the optical power limit of detection has been lowered approximately four orders of magnitude from that of the DC measurement system in Chapter 2. Note that the V_{LED} signal can be measured with a very high SNR even at bias signal amplitudes corresponding to the optical power LOD, so the uncertainty associated with the LED bias always negligible. We can now apply this optical power measurement scheme to the L-I-V-T characterization of the LED21Sr at low bias.

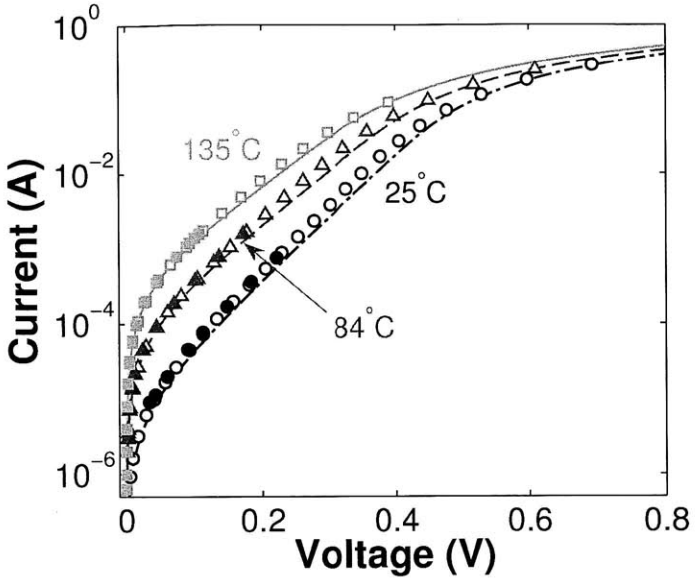

(a)

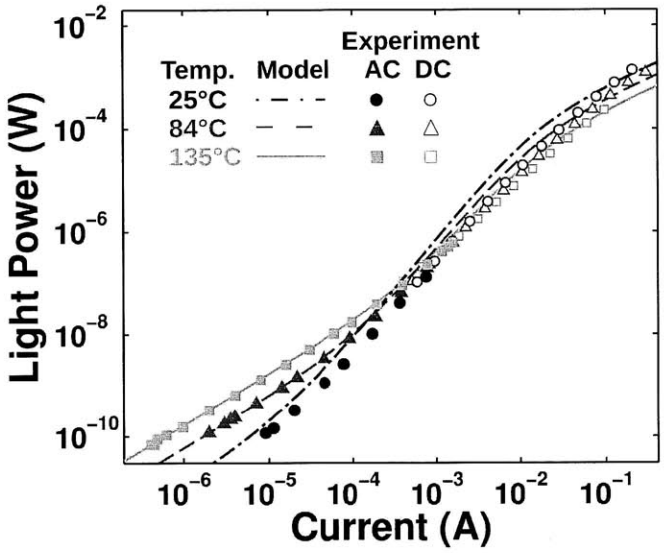

(b)

Figure 3-8: Comparison of the I-V (a) and L-I (b) characteristics of the LED21Sr as predicted by the model developed in Chapter 2 (lines), as measured using the DC characterization apparatus used in Chapter 2 (markers with white area) and as measured using the lock-in apparatus described in this Chapter (filled markers).

3.5 Lock-In LED Characterization Results

I-V-T and L-I-T characteristics with the simulation results and DC experimental data presented in Chapter 2 and new data measured with the lock-in system discussed

above are presented in Figure 3-8. We see that the lock-in and DC I-V and L-I experimental data overlap well at all temperatures. Note that the modeled device characteristics are the same as those presented at the end of Chapter 2, including the fitting parameter values.

Figure 3-9 shows η_Q-I and η-L characteristics from the L-I-V-T data presented in Figure 3-8. We see that η_Q approaches a constant value at low bias, that this value rises with temperature, and that the predicted $\eta \sim V^{-1}$ relationship is well replicated by experiment. Most notably we see that three data points taken at 135°C demonstrate $\eta > 1$ with uncertainties too small to suggest that these are spurious results. Note that several other data points with $\eta > 1$ were measured at temperatures between 84°C and 135°C. We view this as conclusive evidence of electroluminescent cooling. To our knowledge this is also the first experimental evidence of this phenomenon.

The measured electoluminescent cooling power is plotted in Figure 3-10. We see that cooling power rises linearly with current at low bias before heating due to inefficiency in the device that has a quadratic dependence on current begins to dominate and eventually brings the LED into the more familiar net-heating regime. We also note that the maximum cooling power rises with increasing temperature. We can quantitatively encapsulate the enhancement seen in the thermal pumping effects at elevated temperatures in two values, the low-bias quantum efficiency $\lim_{V\to 0}\eta_Q$ and the zero-bias resistance R_{zb}. While $\lim_{V\to 0}\eta_Q$ is familiar from Chapter 1, we have not yet encountered R_{zb}. R_{zb} describes the linear relationship between the applied voltage and the injected current in the low-bias regime. For a small applied voltage bias V, insignificant leakage occurs in an LED and current is determined by the net recombination rate in the active region [5, 13]. In the LED21Sr we assume SRH recombination dominates at low bias.

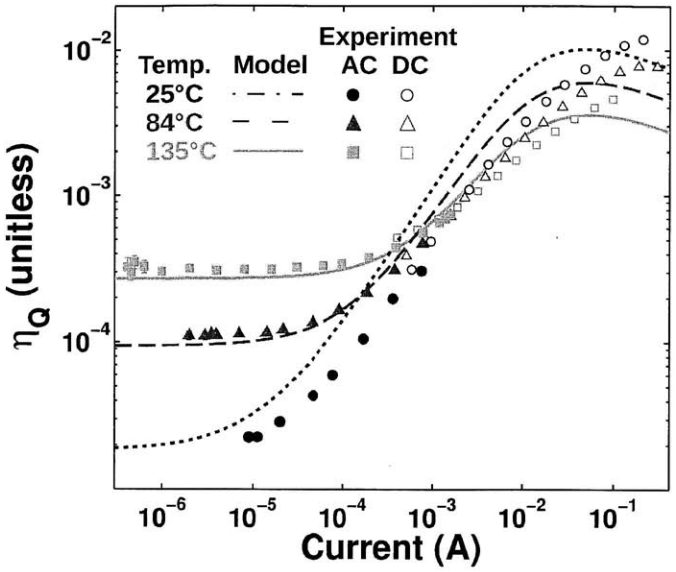

(a)

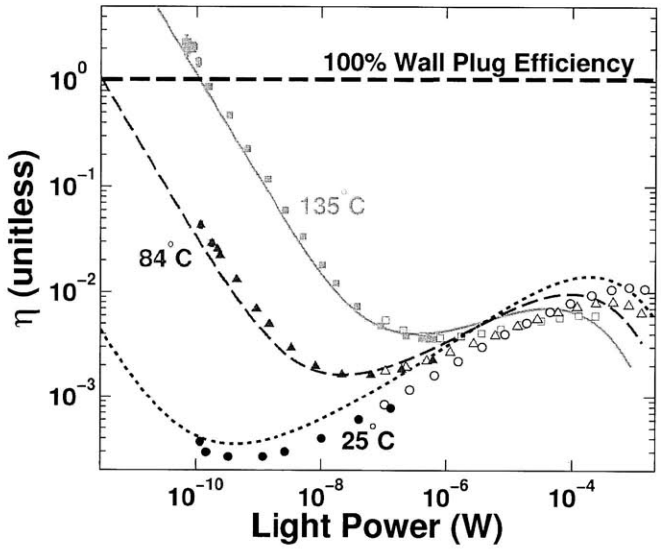

(b)

Figure 3-9: Comparison of the η_Q-I (a) and η-L (b) characteristics of the LED21Sr as predicted by the model developed in Chapter 2 (lines), as measured using the DC characterization apparatus described in Chapter 2 (markers with white area) and as measured using the lock-in apparatus described in this Chapter (filled markers). Electroluminescent cooling is demonstrated in (b).

$$
\begin{aligned}
I &\approx t\frac{1}{4n_i\tau_{SRH}}n_i^2(e^{\frac{qV}{k_BT}}-1) \\
&\approx \frac{tn_i}{4\tau_{SRH}}\frac{qV}{k_BT} \\
\rightarrow R_{zb} &= \frac{V}{J} \\
&\quad \frac{4k_BT\tau_{SRH}}{}
\end{aligned}
$$

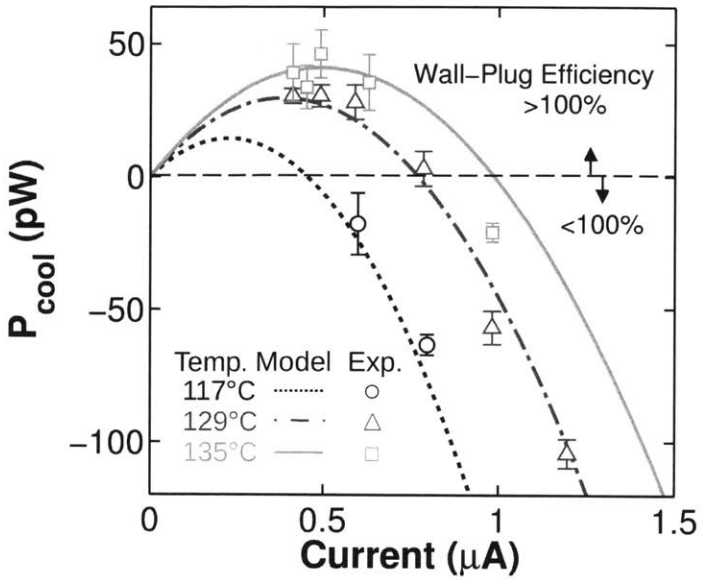

Figure 3-10: Electroluminescent cooling power as a function of current in the LED21Sr at 117°C, 129°C and 135°C as predicted by the model developed in Chapter 2 (lines) and measured using the lock-in apparatus described above (markers). Negative values indicate that net heating is occurring due to inefficiencies in the LED.

We assume in deriving Equation 3.12 that qV is on the order of k_BT, thus allowing the approximation $e^{\frac{qV}{k_BT}} - 1 \approx \frac{qV}{k_BT}$ by Taylor expansion. Physically we interpret this approximation as equivalent to assuming that the deviation from equilibrium ($V = 0$) is small enough to give rise to a linear response from the diode. We see that R_{zb} decreases with increasing temperature as a result of an increasing intrinsic carrier density in the active region. This means that for a fixed applied voltage in the low-bias regime, increasing the diode temperatures will increase the current that flows, and thus the light that is emitted (since the η_Q in this regime is approximately constant). A more complete treatment of the temperature dependencies of R_{zb} and η_Q will be presented in Chapter 4. Figure 3-11 shows simulated and measured values of $\lim_{V\to 0}\eta_Q$ and R_{zb} as a function of LED temperature. We see that the modeled temperature dependencies of these values matches experiment well. We also see that over the range of temperatures measured, which corresponds to 37% increase in k_BT from 25°C to 135°C, $\lim_{V\to 0}\eta_Q$ and R_{zb} improved (increased and decreased respectively) by approximately one and a half orders of magnitude.

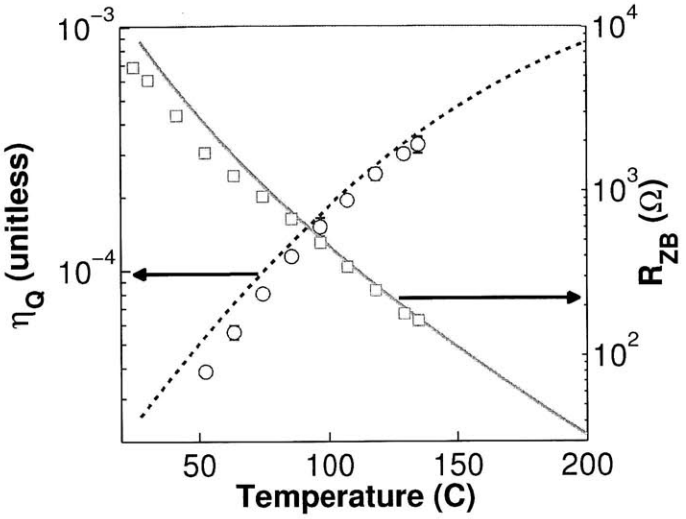

Figure 3-11: Low-bias η_Q and R_{zb} as a function of temperature predicted by the model developed in Chapter 2 and measured at 12 temperatures between 25°C and 135°C using the lock in technique described above.

3.6 Summary and Conclusions

In Section 3.2 lock-in measurement was discussed in detail. In Section 3.3 measurement apparatus designed to use lock-in amplification for low-bias L-I-V-T LED characterization was presented. In Section 3.4 the optical power limit of detection was shown to be approximately 5pW, an improvement of nearly four orders of magnitude in comparison with the DC characterization technique employed in Chapter 2. In Section 3.5 we presented L-I-V-T characteristics of the LED21Sr collected using this lock-in measurement apparatus. We showed that this data included demonstration of electroluminescent cooling at low-bias as predicted by the model developed in Chapter 2.

We have experimentally confirmed the theoretical prediction that an LED can act as a heat pump at low bias, emitting light with $\eta > 1$, and that this effect grows strongly as the temperature of the LED is increased. To demonstrate this phenomenon, it was necessary to resolve picowatt-scale optical power signals emitted from a LED emitting in the mid-infrared at elevated temperature. This was achieved using a precision frequency- and phase-sensitive lock-in measurement. While this

result is conceptually interesting, it seems likely that the optical power levels achievable at high efficiency due to thermal pumping will need to be increased significantly before this effect can be of practical interest. In Chapter 4 we will use the modeling framework developed in Chapter 2 to explore potential design strategies to enhance thermal pumping in an LED and give quantitative predictions of potential improvement in the achievable optical power at unity efficiency $L_{\eta=1}$ as a function of band gap and device temperature.

Chapter 4

Design for Thermal Pumping in LEDs

4.1 Chapter Overview

Generation of optical power with $\eta \geq 1$ by a thermally pumped LED can only have applications at the system level if sufficient light power can be achieved in the thermal pumping regime. We can use the optical power generated with unity wall plug efficiency $L_{\eta=1}(T)$ as a figure of merit to describe thermal pumping in an LED at temperature T. In Chapter 3 we demonstrated experimentally that $L_{\eta=1}(135°\text{C}) \approx 10^{-10}$W for the LED21Sr. We now seek to give quantitative predictions of improvement in $L_{\eta=1}(T)$ that could be achieved in a double-heterojunction LED in the GaInAsSb/GaSb material system. In Section 4.2, the methods of maximizing $L_{\eta=1}$ of a GaInAsSb/GaSb LED for a given operating temperature T and relevant design constraints will be discussed. In Section 4.3 we will consider the different factors that determine $L_{\eta=1}$ and how they depend on temperature and LED structure. We will develop a comprehensive model for $L_{\eta=1}$ and optimize it within our specified design constraints. In Section 4.4 the optimized design will be simulated using the approach presented in Chapter 2, and predictions of device characteristics in the thermal-pumping regime will be given. Section 4.5 will include a summary of the Chapter and conclusions.

4.2 Material Constraints for GaInAsSb/GaSb LEDs

As discussed in Chapter 1, for fixed recombination parameters τ_{SRH}, B and C, $L_{\eta=1}$ should increase exponentially as the ratio of the active region band gap to the thermal energy $-\frac{E_{gap}}{k_BT}$ approaches zero. τ_{SRH}, B and C have polynomial dependencies on E_{gap} and T that cause the quantum efficiency η_Q at fixed carrier density to decrease with $\frac{E_{gap}}{k_BT}$. However the exponential dependence of the intrinsic carrier concentration n_i on $-\frac{E_{gap}}{k_BT}$ causes $L_{\eta=1}$ to increase as $-\frac{E_{gap}}{k_BT}$ approaches zero even though η_Q is decreasing. Thus we seek to minimize $\frac{E_{gap}}{k_BT}$. In practice, the minimum achievable band gap $E_{gap,min}$ and the maximum achievable temperature T_{max} will be set by material constraints.

The minimum achievable band gap in the GaInAsSb quaternary material system lattice-matched to GaSb is approximately 300meV at molefractions near $Ga_{.13}In_{.87}As_{.88}Sb_{.12}$ [68, 69]. However heterojunctions between GaSb and GaInAsSb near this mole-fraction form broken-gap type II interfaces which exhibit either large-barrier Schottky-like electrical characteristics (n-GaSb/n-GaInAsSb, p-GaSb/p-GaInAsSb, n-GaSb/p-GaInAsSb) or inter-band-tunneling-dominated electrical characteristics (p-GaSb/n-GaInAsSb) [69]. Although there is potential for the use of such interfaces in LEDs, designing with these electron transport effects and modeling effects like nonlocal recombination that occur at these interfaces goes beyond the scope of this thesis. A miscibility gap exists in which GaInAsSb will not form for mole fractions that correspond to band gaps between approximately 0.32eV and 0.5eV [69], although growth of metastable alloy in this miscibility gap with a room temperature band gap of 0.45eV on GaSb has been demonstrated [70]. Thus we will set $E_{gap,min}$ to be 0.45eV in undoped GaInAsSb at room temperature.

The melting point of GaSb, 712°C (985°K) [71], is lower than that of GaInAsSb, 1100°C (1373°K) [53]. However the melting point of GaSb will only be the limiting factor that determines T_{max} if GaSb can be metalized with a contact that can survive above 712°C. GaSb-based devices contacted with gold in the same fashion as the LED21Sr exhibit diffusion of gold into the GaSb at temperatures near 180°C [42]. Low resistance, thermally stable contact methods to n- and p-type GaSb have

recently become a topic of great interest [72, 73, 74, 75]. State of the art ohmic contacts in this material show significant atomic diffusion at the contact interface above approximately 350°C [72, 73, 74], however the annealing procedures used to probe the thermal stability of these structures were never longer than 400 hours. Lead contacts on n-GaSb intended to create Schottky barriers have shown low-resistance metallurgical junction formation for anneal temperatures above 450°C [76]. Recently Schottky contacts to n-GaSb with effective barriers of 70meV have been demonstrated with thin dielectric layers of titanium dioxide (TiO_2) between aluminum (Al) and GaSb [75]. While the thermal stability of these contacts was not presented, the melting temperatures of Al (660°C [77]) and TiO_2 (1870°C [78]) suggest that such a structure may survive to temperatures above 600°C. It is unclear which GaSb contact method would set T_{max} of an LED in this material system, so we will consider device characteristics as functions of temperature T between 25°C and 600°C.

4.3 LED Optimization for Thermal Pumping

Our goal in this Chapter is to maximize the optical power output of a thermally pumped GaInAsSb LED at 100% wall plug efficiency. Our first step is to maximize η_Q in the low-bias regime. The simplest approach to this problem is dope the active region such that the likelihood of radiative recombination at low-bias is only dependent on the concentration of one diffusing minority carrier species rather than two. The effect this has on the quantum efficiency of an LED at low bias was demonstrated in Section 2.2.4, and has been explored in the literature [79, 6, 13]. We choose to n-dope the active region to avoid possible reduction in η_Q due to light-hole to heavy-hole or split-off-hole to heavy-hole free-carrier absorption caused by p-doping the active region. Following the analysis presented in [6], we expect optimized quantum efficiency in a double-heterojunction LED for a dopant density $N_{D,opt}$

$$N_{D,opt} = (\tau_{SRH} C)^{-\frac{1}{2}} \tag{4.1}$$

Based on recent review of challenges faced in growth of GaInAsSb [80], we expect

that at present the minimum achievable background impurity density is $\approx 10^{16}\text{cm}^{-3}$. This sets a minimum viable doping level for the active region of an LED in this material system. Before we calculate dopant density for the active region of our LED, we must consider the dependencies of τ_{SRH} and C on material band gap and temperature. As we will show, these dependencies dictate that the optimal doping level $N_{D,opt}$ is will depend on the target operation temperature for the device.

Based on experimental and theoretical studies of Auger processes in this material system [81, 82], we expect that the dominant Auger mechanism in GaInAsSb with $E_{gap} = 0.45\text{eV}$ is either a **C**onduction band electron scattering interacting with two **H**eavy holes to result in one **L**ight hole (**CHHL**) or two **C**onduction band electrons interacting with a **H**eavy hole resulting in one **C**onduction band electron (**CHCC**), since at this mole-fraction the band gap is smaller than the energy gap between the valence band edge and the split-off hole band edge Δ_0 [69] which precludes Auger processes where one **C**onduction band electron and two **H**eavy holes generate one **S**plit-off hole (**CHHS**).

For electron non-degenerate electron populations we expect the Auger recombination parameter C to have the following dependence on temperature T and band gap E_{gap} [83]:

$$C \sim C_0\sqrt{T}E_{gap}^{-\frac{5}{2}}e^{-\frac{(1-\mu_i)E_{gap}}{k_BT}} \tag{4.2}$$

$$\mu_{CHHL} = \frac{2m_H + m_C}{2m_H + m_C - m_L} \tag{4.3}$$

$$\mu_{CHCC} = \frac{2m_C + m_H}{m_C + m_H} \tag{4.4}$$

where μ_i in Equation 4.2 is a reduced mass term whose values for **CHHL** and **CHCC** processes are given in Equations 4.3 and 4.4 in terms of the effective masses for heavy holes m_H, light holes m_L and electrons m_C. The values $m_H \approx 0.46m_0$, $m_L \approx .055m_0$ and $m_C \approx .03m_0$ for GaInAsSb at our mole fraction (m_0 is the electron rest mass) can be calculated with the ab initio band structure parameters presented in [84]. Note that we ignore the temperature dependence of these parameters in this

calculation.

We calculate E_{gap} using the phenomenalogical temperature-dependent band gap relationship of GaSb [1, 44].

$$E_{gap}(T) \approx 0.536 - \frac{3.78 \cdot 10^{-4} T^2}{T + 94} \tag{4.5}$$

Including the dependence of E_{gap} on the dopant density in the active region would require that $N_{D,opt}$ be calculated iteratively, so we ignore this dependence here for simplicity. The SRH recombination lifetime will be modeled as only having a temperature dependence set by the average thermal velocity of charge carriers v_{therm} in the Boltzmann limit:

$$\tau_{SRH} \sim v_{therm}^{-1} \sim T^{-\frac{1}{2}} \tag{4.6}$$

Equation 4.6 implies that the density and scattering cross sections of the impurities that cause SRH recombination are independent of band gap and temperature. We note that values of room temperature τ_{SRH} in GaInAsSb reported in the literature for devices grown by organometallic vapor phase epitaxy (OMVPE) are 1μs [48], approximately one order of magnitude longer than the value used as a fitting parameter to model the LED21Sr in Chapter 2. Since the purpose of this design exercise is to give quantitative predictions of achievable improvements in LEDs in this material system, we will use $\tau_{SRH}|_{300K} = 1\mu$s to model devices in this Chapter. C and τ are plotted as functions of temperature in Figure 4-1. The room temperature value of τ in this plot is from the literature [48]. The room temperature value of C, C_0 is calculated by adjusting a value given in the literature [48] for a different alloy composition of GaInAsSb using Equation 4.2 and the two reported room temperature band gap energies [70, 48]. The values at elevated temperatures are calculated using Equations 4.5, 4.6 and 4.2. We note that there is experimental evidence [82] suggesting that Auger recombination is dominated by the **CHHS** process for the GaInAsSb composition in [48]. In this case, our extrapolated C value may be far too large since **CHHS** processes are not allowed in $Ga_{.68}In_{.32}As_{.28}Sb_{.72}$, where the split off gap Δ_0

is greater than E_{gap}. To account for this we will calculate optimal doping levels and quantum efficiencies for C_0 calculated with the measured value from [48], as well as for room temperature C values $0.1C_0$ and $0.01C_0$.

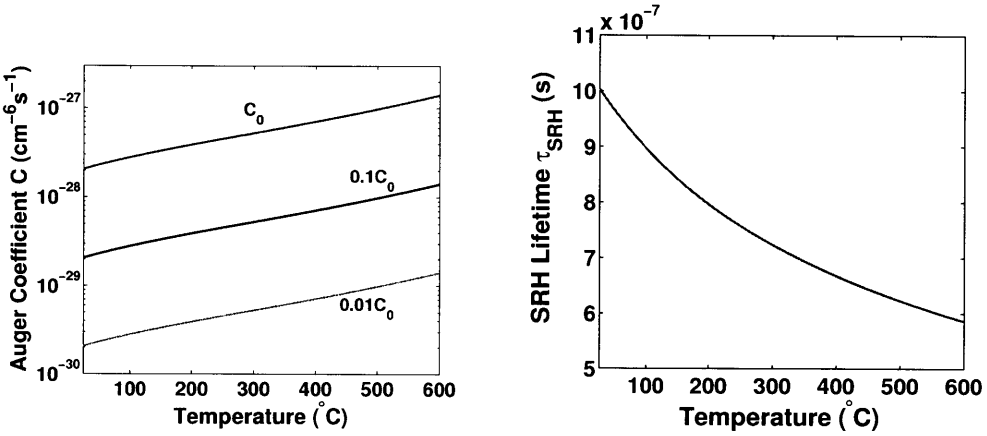

(a) (b)

Figure 4-1: Calcuated values of the Auger recombination coefficient C and the SRH recombination lifetime in the $Ga_{.68}In_{.32}As_{.28}Sb_{.72}$ active region of a GaInAsSb/GaSb LED as functions of temperature. C is calculated for three possible room temperature values.

We can now calculated $N_{D,opt}$ according to Equation 4.1 as a function of T. Note that Equation 4.1 was derived with the assumption that the dopant density will be greater than the intrinsic carrier concentration and would thus affect carrier density n and quantum efficiency η_Q [6]. Thus it is also of interest to compare the intrinsic carrier concentration n_i with the calculated value of $N_{D,opt}$. n_i is calculated iteratively according to Fermi-Dirac statistics by enforcing these three conditions [5]

$$n_i = p_i \tag{4.7}$$

$$n_i = 2\frac{2}{\sqrt{pi}}\left(\frac{2\pi m_C k_B T}{h^2}\right)^{\frac{3}{2}} \mathbf{F}_{\frac{1}{2}}\left(\frac{E_F - E_C}{k_B T}\right) \tag{4.8}$$

$$p_i \approx 2\left(\frac{2\pi m_C k_B T}{h^2}\right)^{\frac{3}{2}} e^{\frac{E_V - E_F}{k_B T}} \tag{4.9}$$

where we assume because of the strong asymmetry in the conduction and valence

band curvatures that the electron population will become degenerate and the hole population will stay in the Boltzmann limit as the temperature increases. The calculated values of $N_{D,opt}$ and n_i are plotted as functions of temperature in Figure 4-2. We see that for a given value of C, n_i surpasses $N_{D,opt}$ for sufficiently high temperature. We can assume then that doping will not improve η_Q in this high temperature regime.

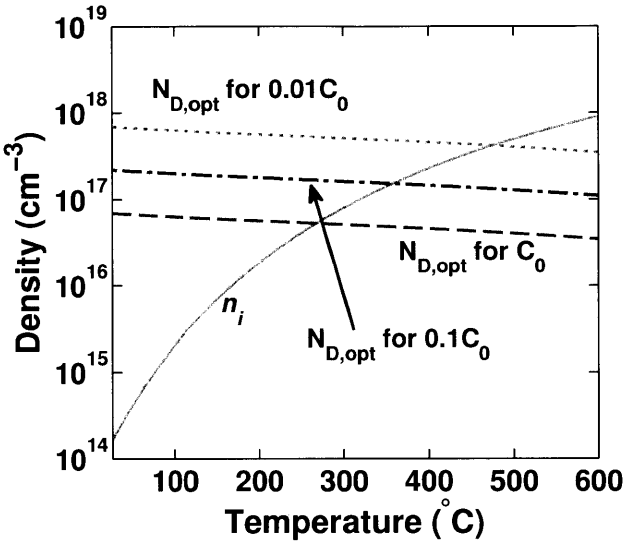

Figure 4-2: Calcuated values of intrinsic carrier concentration n_i in the active region of a $Ga_{.68}In_{.32}As_{.28}Sb_{.72}$ LED and the optimal dopant density $N_{D,opt}$ calculated following Heikkila [6]. $N_{D,opt}$ is calculated for three possible room temperature values of C.

To calculate the low-bias η_Q as a function of temperature it is also necessary to consider how current leakage from the active region and the bimolecular recombination coefficient B changes with increasing temperature. The dependence of the bimolecular recombination coefficient B on E_{gap} and T is calculated following the van Roosbroek-Shockley model for direct radiative transitions near parabolic band edges [7, 83]

$$B \sim T^{-\frac{3}{2}} E_{gap}^2 \tag{4.10}$$

Equation 4.10 does not account for the temperature dependence of the carrier effective masses. We note that the temperature dependencies of C and B expressed in Equations 4.2 and 4.10 respectively are only valid in the Boltzmann limit. In the

low-bias regime, leakage current is approximately proportional to the square of the intrinsic carrier concentration in the active region [6]. We can approximate the carrier leakage rate with a leakage coefficient D

$$\begin{aligned} R_{leak} &= \frac{J_{e,p} + J_{h,n}}{qt} \\ &\approx = \frac{1}{t}\left[\frac{k_B T \mu_{e,p}}{x_p N_A} + \frac{k_B T \mu_{h,n}}{x_n N_D}\right] e^{-\frac{\Delta E_{gap}}{k_B T}} \frac{N_{V,GaSb} N_{C,GaSb}}{N_V N_C} np \qquad (4.11) \\ &= Dnp \qquad (4.12) \end{aligned}$$

where t, x_n and x_p are the thicknesses of the GaInAsSb active region, the p GaSb layer and the n GaSb layer respectively, $\mu_{e,p}$ and $\mu_{h,n}$ are the minority electron mobility in p-GaSb and the hole mobility in n-GaSb, $N_V, GaSb$ and $N_C, GaSb$ are the effective densities of states at the band edges in the GaSb, N_A and N_D are the doping levels in the p- and n-GaSb respectively, ΔE_{gap} is the band gap difference between GaSb and the GaInAsSb in the active region, and N_V, N_C, n and p are the effective densities of states at the band edges and the carrier concentrations in the GaInAsSb active region. Note that Equation 4.11 is derived in the appendix of [6]. Here we take t, x_n and x_p to be 4μm, as in the LED21Sr. We note that the values of new values of t, x_n and x_p can be found to optimize η_Q by reducing leakage and maximizing η_{IQE} for significant photon recycling, but this will be left to future work. D is especially useful because it has the same units as B and thus the two can be directly compared. B and D are plotted as functions of temperature in Figure 4-3. As with C, an experimental value of B from the literature measured with a GaInAsSb sample of a different alloy composition [48] is adjusted according to Equation 4.10 to estimate the room temperature value in our device. Then Equation 4.10 is used to calculate the temperature dependence. D is calculated according to according to Equation 4.11.

The low-bias limit of η_Q calculated in Section 1.2.2 no longer applies to the LED design being considered since the carrier concentration in the active regions is now high enough for significant Auger recombination. It is of interest to know the expected

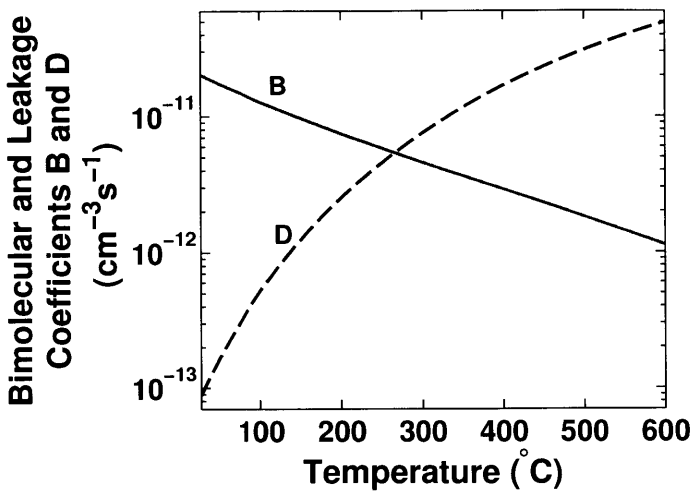

Figure 4-3: Calcuated values of the bimolecular recombination coefficient B and leakage coefficient D as functions of temperature.

low-bias quantum efficiency at the temperatures being considered, since it can be used to optimize the thickness of the active region. We now modify Equation 1.15 from Section 1.2.2 to include Auger recombination and to only calculate low-bias η_{rec} rather than low-bias η_Q for an LED with an intrinsic active region.

$$\begin{aligned} \lim_{V\to 0} \eta_{rec} &= \frac{R_{bimol}}{R_{SRH} + R_{bimol} + R_{Aug} + R_{leak}} \\ &= \frac{B}{[4n_i\tau_{SRH}]^{-1} + B + 2n_iC + D} \end{aligned} \tag{4.13}$$

We approximate the low-bias $\eta_{rec}|_{N_{D,opt}}$ of an LED with a doped active region the same way, summing the intrinsic carrier concentration with the calculated optimal dopant density $N_{D,opt}$.

$$\lim_{V\to 0} \eta_{rec}|_{N_{D,opt}} = \frac{B}{[(4n_i + N_{D,opt})\tau_{SRH}]^{-1} + B + (2n_i + N_{D,opt})C + D} \tag{4.14}$$

η_{rec} is plotted against temperature for devices intrinsic (solid lines) and doped (dashed lines) active regions for three values of C in Figure 4-4. We see that doping

the active region increases η_{rec} substantially near room temperature, but that at an elevated temperature when n_i gets within an order of magnitude of $N_{D,opt}$ the quantum efficiency of the LED is slightly reduced by doping the active region. As the temperature continues to rise and n_i grows larger than $N_{D,opt}$, η_{rec} is virtually unaffected by the doped active region.

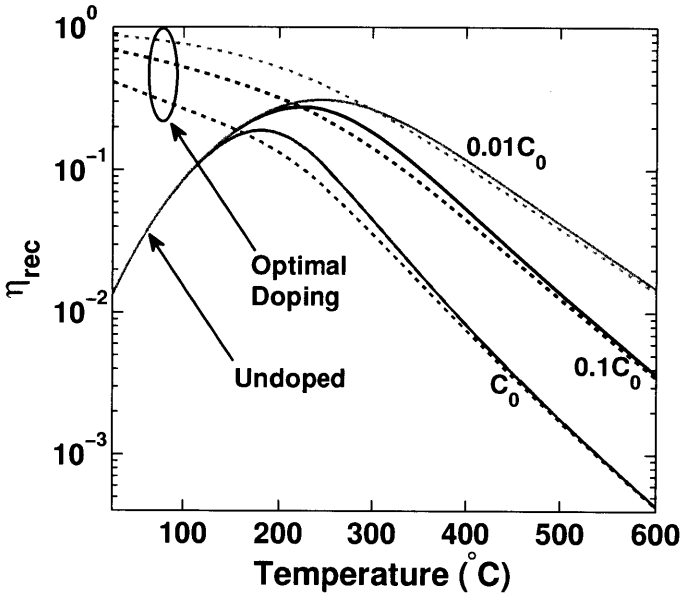

Figure 4-4: Calculated recombination efficiency η_{rec} as a function of temperature for three possible value of the Auger recombination coefficient C. The dashed lines indicate η_{rec} calculated for optimal doping.

We can now maximize $L_{\eta=1}$ as function of active region thickness t and temperature T. Recalling Equation 1.16

$$V_{\eta=1} = \frac{\langle \hbar\omega \rangle}{q} \eta_Q(t,T)$$

where we have noted the dependence of η_Q on t and T, we can approximate $V_{\eta=1}$ as

$$V_{\eta=1} = \frac{\langle \hbar\omega(T) \rangle}{q} \frac{\eta_{rec}(t,T)\eta_{act}(t)}{1-(1-\eta_{act}(t))\eta_{rec}(t,T)} \tag{4.15}$$

where $\eta_{rec}(t,T)$ calculated using Equation 1.14. We point out here that the dependence of η_{rec} on active region thickness t results from the dependence of the leakage

rate coefficient D on t. We also note that we do not include an extraction efficiency in η_Q here, as this would be determined by the specific geometry and packaging of the LED. To estimate the portion of this applied voltage $V_{\eta=1}$ that will be dropped across the active region rather than across the specific resistance at the ohmic contacts, we calculate the zero bias specific resistance (in Ωcm^2) of the LED junction in similar fashion to Equation 3.12.

$$\begin{aligned} J &\approx t\left[\frac{1}{(4n_i+N_{D,opt})\tau_{SRH}}+B+(2n_i+N_{D,opt})C+D\right]n_i^2(e^{\frac{qV}{k_BT}}-1) \\ &\approx t\left[\frac{1}{(4n_i+N_{D,opt})\tau_{SRH}}+B+(2n_i+N_{D,opt})C+D\right]n_i^2\frac{qV}{k_BT} \\ \rightarrow R_{zb} &= \frac{V}{J} \\ &= \frac{k_BT}{qtn_i^2\left[\frac{1}{(4n_i+N_{D,opt})\tau_{SRH}}+B+(2n_i+N_{D,opt})C+D\right]} \end{aligned} \tag{4.16}$$

where t is the active region thickness. The specific resistance at the ohmic contacts R_Ω is taken to be $4.8{\cdot}10^{-4}\Omega\text{cm}^2$, which corresponds to the 0.78Ω series resistance measured from an LED21Sr with a mesa area of approximately $6.2{\cdot}10^{-4}\text{cm}^2$. R_Ω is assumed to result from tunneling processes at the metal-GaSb interfaces that are approximately temperature independent [22]. We calculate $L_{\eta=1}$ in similar fashion to Equation 1.19, using the voltage divider $\frac{R_{zb}}{R_{zb}+R_\Omega}$ to calculate the voltage dropped across the junction

$$\begin{aligned} L_{\eta=1} &\approx \eta_{act}\langle\hbar\omega\rangle tR_{bimol} \\ &= \eta_{act}\langle\hbar\omega\rangle tBn_i^2(e^{\frac{R_{zb}}{R_{zb}+R_\Omega}\frac{qV_{\eta=1}}{k_BT}}-1) \end{aligned} \tag{4.17}$$

We note that that $L_{\eta=1}$ will not increase linearly as a function of t once t is on the order of the diffusion length x_{diff} of a carrier across the active region [7, 16]. However we assume here that $t \ll x_{diff}$.

We now calculate $L_{\eta=1}(t,T)$ accoring to Equation 4.17 for $t \in (0,6)\mu$m and $T \in (25,600)^\circ$ C for each value of the Auger coefficient C being considered. We then find the the $L_{\eta=1}(t,T)$ maxima in this space. Figure 4-5 shows contour plots indicating the locations in the (t,T) plane of the $L_{\eta=1}(t,T)$ maxima for three different values of C, as well contours on which $L_{\eta=1}(t,T)$ is 98% and 95% respectively of the maximum value. We see that for the two reduced Auger coefficients $0.1C_0$ and $0.01C_0$ there are local maxima both at room and elevated temperature. The room temperature maxima arise because η_{rec} and hence η_Q are especially high at room temperature in these devices (see Figure 4-4). Since the corresponding large voltage biases would take the LED far from equilibrium (invalidating Equation 4.14), these calculated maxima are not considered to be physical.

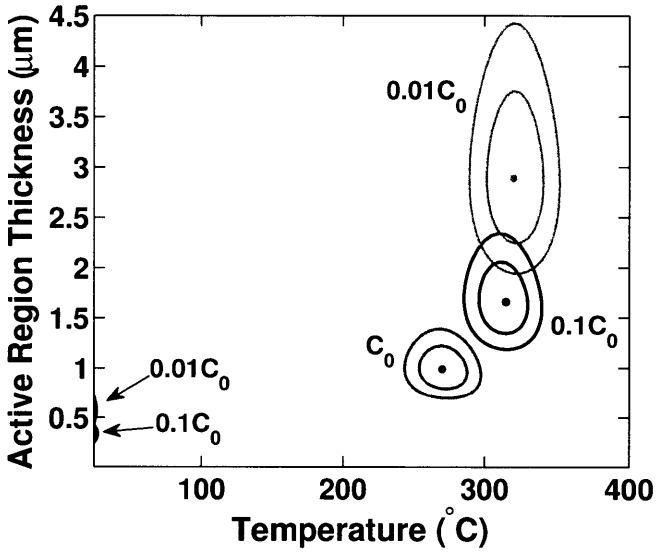

Figure 4-5: Locations of $L_{\eta=1}$ maxima for the three C values being considered. The contours around each maxima indicate the boundaries within which $L_{\eta=1}$ is at least 98% and 95% of the maximum.

We have determined the optimal doping level, active region thickness and operating temperature for a $Ga_{.68}In_{.32}As_{.28}Sb_{.72}/GaSb$ LED for three possible values of the Auger coefficient. The calculated LED characteristics at these maxima are given in Table 4.1. Next we simulate these devices using the hydrodynamic charge and energy transport model presented in Chapter 2 to predict the optimized output light power

density from such an LED.

	$C \sim C_0$	$C \sim \frac{C_0}{10}$	$C \sim \frac{C_0}{100}$
Temperature T (°C)	270	315	320
Band gap E_{gap} (eV)	0.361	0.344	.343
Peak Emission Wavelength λ_{peak}	2	4	4
Active Region Thickness t (μm)	0.99	1.64	2.89
Optimal Active Region Doping $N_{D,opt}$ (cm^{-3})	$5.2{\cdot}10^{16}$	$1.6{\cdot}10^{17}$	$5{\cdot}10^{17}$
η_{act}	.42	.3	.19
η_{rec}	.05	.09	.19

Table 4.1: Attributes of the LED structures corresponding to the three maxima shown in Figure 4-5 for different values of the Auger parameter C_0.

4.4 Simulated Characteristics of Optimized LEDs

Based on the results in Section 4.2, we can model the LEDs with the characteristics given in Table 4.1 using the 1 dimensional hydrodynamic approach presented in Chapter 2. In this case since we are studying $L_{\eta=1}$, we only simulate the LEDs in the bias voltage range were we expect to see significant thermal pumping effects.

We use the same transverse area and extraction efficiency to model the optimized LEDs as was used to model the LED21Sr to facilitate direct comparison. We assume that a different photo-detector that has a more appropriate spectral responsivity would be used to measure optical power output from the optimized LEDs, and thus do not reduce their optical power by the spectral responsivity of the InGaAs photodiode used for characterization in Chapters 2 and 3. Simulated L-I-V characteristics of the optimized LEDs are plotted in Figure 4-6 along with L-I-V-T charactersitics from the LED21Sr from Chapters 2 and 3. We see that the L-I characteristic of the LED optimized for an Auger parameter corresponding to C_0 at 270°C is very similar to that of the LED21Sr at 135°C. We see from the I-V characteristics however that significantly less applied voltage is required to drive the same current in the optimized devices.

The LED wall plug efficiency η simulated in LEDs optimized for three values

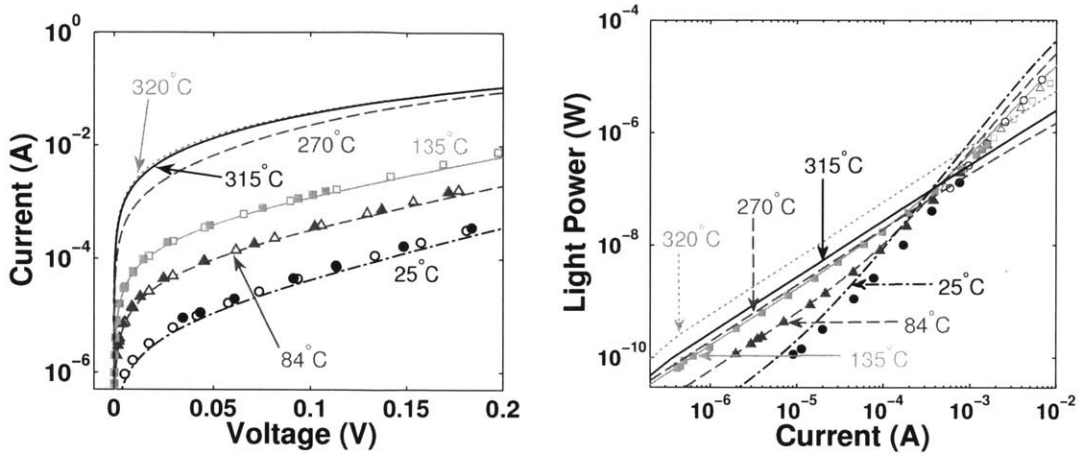

(a) (b)

Figure 4-6: (a)I-V and (b)L-I characteristics of the LED21Sr (model and experiment) at 25°C, 84°C and 135°C, and modeled characteristics of optimized $Ga_{.68}In_{.32}As_{.28}Sb_{.72}$/GaSb LEDs. Devices were optimized for Auger parameters corresponding to C_0, $0.1C_0$ and $0.01C_0$ at 270°C, 315°C and 320°C respectively. Optimized LEDs are modeled using the same transverse area ($6.2{\cdot}10^{-4}$cm^2) and extraction efficiency (14%) used to model the LED21Sr.

of the Auger coefficient are plotted as function of optical power L in Figure 4-7, along with η-L data collected from the LED21Sr in Chapters 2 and 3. The three modeled values of $L_{\eta=1}$ are approximately $2{\cdot}10^{-4}$Wcm^{-2}, 10^{-3}Wcm^{-2} and $6{\cdot}10^{-3}$Wcm^{-2} for Auger coefficients corresponding to C_0, $C_0/10$ and $C_0/100$ respectively. These power densities correspond to optical powers of $1{\cdot}10^{-7}$W, $6{\cdot}10^{-7}$W and $4{\cdot}10^{-6}$W in a mesa with area equivalent to the LED21Sr. Although it unclear what the maximum practical operating temperature is for a GaInAsSb/GaSb LED, the method presented in Section 4.3 can be used to find the optimal doping level and active region thickness for such an LED given any maximum temperature value. Sentaurus can then be used to simulate the device characteristics, as we have shown here.

4.5 Summary and Conclusion

In Section 4.2, we examined the material constraints associated with GaInAsSb LEDs. These constraints gave us a space within which we could engineer an LED to output

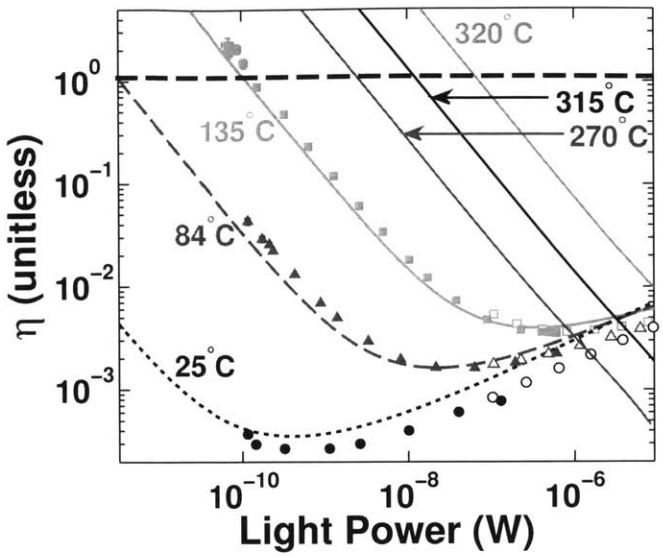

Figure 4-7: Wall plug efficiency η plotted against light power L of the LED21Sr (model and experiment) at 25°C, 84°C and 135°C, and modeled characteristics of optimized $Ga_{.68}In_{.32}As_{.28}Sb_{.72}$/GaSb LEDs. Devices were optimized for Auger parameters corresponding to C_0, $0.1C_0$ and $0.01C_0$ at 270°C, 315°C and 320°C respectively. Optimized LEDs are modeled using the same transverse area ($6.2{\cdot}10^{-4}cm^2$) and extraction efficiency (14%) used to model the LED21Sr.

maximized optical power at 100% wall plug efficiency η. In Section 4.3 we presented a method for calculating the optimal active region dopant density for a thermally pumped GaInAsSb LED as a function of temperature and then approximated the quantum efficiency as a function of active region thickness and temperature. Finally we calculated the applied voltage $V_{\eta=1}$ and emitted light power density $L_{\eta=1}$ at 100% wall plug efficiency from the LED within t,T space and chose optimal values of these parameters. In Section 4.4 we presented simulation results predicting characteristics of devices optimized according to the results presented in Section 4.3. We saw that many orders of magnitude of improvement in $L_{\eta=1}$ could be achieved just by following the optimization algorithm presented in this Chapter.

While the focus of this Chapter was on optimization of a GaInAsSb LED, the approach presented here is general can could be used to similarly optimize an LED in another material system or even under entirely different constraints. The simulation results presented in Section 4.3 demonstrate that commercial semiconductor device

TCAD software is not only capable of modeling thermal pumping in LEDs but also useful for designing devices for enhanced thermal pumping.

Chapter 5

Conclusions and Future Work

The work presented here is a general study of thermal pumping in LEDs. We started in Chapter 1 by examining the various factors that determine the efficiency of an LED. We noted that the feeding efficiency η_f of an LED can be greater than one. We then showed that for sufficiently high quantum efficiency η_Q the wall plug efficiency η of an LED can also be greater than one. We discussed that in this scenario electrons and holes are absorbing energy and entropy from the lattice and then depositing it in photons which can escape the device before being reabsorbed, causing the lattice to cool. We explained this by considering the Peltier energy exchange as charge carriers traverse bipolar semiconductor devices. We showed that this phenomenon should occur in every LED for sufficiently low voltage bias and we derived a few simple relations to estimate the optical power output at which electroluminescent cooling should occur, based on material parameters, light extraction and temperature. We then introduced a numerical model for hydrodynamic charge and energy transport which can used to model this effect.

In Chapter 2 we introduced a prototypical LED, the LED21Sr, that we expected to exhibit strong thermal pumping effects at low bias. We were especially interested in this device because sufficient information was available to study it with modeling and it was also available for experiment. We built up a hydrodynamic model thermal pumping in an LED step-by-step, and ultimately modeled thermal pumping in the LED21Sr. Next we introduced an experimental apparatus for measuring the L-I-V-T

characteristics of an LED and used it to characterize the LED21Sr. By comparing our modeling and experimental results we were able to validate and fine-tune our model, but we were unable to gather conclusive evidence of thermal pumping experimentally.

In Chapter 3 introduced a lock-in measurement apparatus that served to lower the limit of optical power detection of our L-I-V-T characterization apparatus by four orders of magnitude. In doing so, we were able to sufficiently improve the sensitivity of our system to achieve the first ever experimental demonstration of electroluminescent cooling.

In Chapter 4 we considered LED design strategies for enhanced thermal pumping. We set out to design an LED in the GaInAsSb/GaSb material system with maximized optical power output at 100% wall plug efficiency. We showed that by simply doping the active region and changing its alloy composition, we could increase the optical power at unity efficiency by three or four orders of magnitude from that observed in the LED21Sr. The design strategies presented in Chapter 4 are general, and could be useful for designing LEDs under other constraints or with other materials.

5.1 Future Work

A great deal of work remains to be done in the study of thermal pumping and electroluminescent cooling in LEDs.

In the short term a few interesting results might be achieved with minor modifications to the experimental and modeling framework presented here.

Coupling a GaInAsSb/GaSb LED with a smaller active region band gap energy than the LED21Sr to a multi-mode fiber transmissive in the mid-infrared (e.g. fluoride or chalcogenide fiber) could allow for detection with much smaller area photo-diode. If the coupling efficiency of the LED to the fiber does not negate the reduction in the limit of optical power detection of the system, this could open up a realm of possibilities for demonstration of efficient communication and detection. By operating the system with a maximized temperature difference between a hot LED and cold detector, it seems likely that a record could be set for low energy cost per bit in a

fiber optic communication system. Appropriate choice of the LED's active region band gap and operating temperature could also optimize the system for transmission measurement of methane or carbon dioxide concentration.

One opportunity for demonstration of a system-level benefit from thermal pumping in LEDs in the short term is apparent. LED-based pulse oximetry systems have been demonstrated that can detect photo-current signals with amplitudes of order 50nA with SNR $>$ 1000 while dissipating a total of 4.5mW to drive the LED, and amplify and process the signal [85]. Currently the total power consumption of such systems is dominated by LED input power, and these systems are expected to achieve detection of 1nA amplitude photo-current signals with the same SNR and sub-milliwatt total power dissipation in the near future. Optical power levels corresponding to these photo-current signal amplitudes were achieved at wall plug efficiencies greater than 10% using the LED21Sr in Chapter 3. It seems likely that LEDs optimized for thermal pumping as outlined in Chapter 4 could be combined with such an efficient detection system to further improve the low-power limits of pulse-oximetry. First though, it might be possible to demonstrate record-breaking low-power detection of several gases with absorption lines in the mid-infrared using heated commercial LEDs (as in Chapters 2 and 3) and amplifying the photo-current signal with this type of system.

The potential for design of LEDs optimized for thermal pumping could be greatly improved in the short term by expanding the hydrodynamic modeling of charge and energy transfer used in Chapters 2 and 4 to 3-dimensions, and by including light propagation for self-consistent modeling of photon recycling effects. Experimental characterization of recombination parameters in GaInAsSb and other material systems of interest at elevated temperatures would also allow for more accurate modeling.

Potential long-term research topics related to thermal pumping in LEDs can be divided up into three categories.

5.1.1 LEDs in Other Material Systems

The work presented here focused on thermal pumping in GaInAsSb/GaSb LEDs because the relatively small band gaps that can be achieved in this material system made it possible to observe electroluminescent cooling in a device that was not designed to for thermal pumping. A logical next step would be to use the same approach to calculate the limits to the efficiency and power density achievable through thermal pumping as functions in many optoelectronic material systems. Wide band gap semiconductors that can survive in very high temperature environments would be especially interesting, since the ultraviolet LED community is still searching for means improve wall plug efficiency in devices generally designed for low-power applications [9]. It would also be interesting to study thermal pumping LEDs with active region band gap energy on the order of the thermal energy k_BT. This has been suggested a means to maximizing electroluminescent cooling power [32], however it is unclear whether the strongly interacting nature of the electron gas in a narrow gap semiconductor like mercury cadmium telluride (HgCdTe) would enhance or diminish thermal pumping.

5.1.2 LED Self-Heating for "Phonon Recycling"

The work in this thesis highlighted the fact that thermal pumping in LEDs is enhanced at elevated temperatures. It is not however strictly necessary for a thermally pumped LED to operate in a high temperature environment. If a sufficiently thermally insulating package can be designed for an LED, it should be possible to operate an LED at high temperature in a room temperature environment. In this regime, waste heat that results from non-radiative recombination and other parasitic inefficiencies can be retained and used to thermally pump the LED. We call this effect "phonon recycling" because suppression of thermal conduction pathways away from the LED increases steady state excitation levels of the lattice vibrational modes for a fixed input heat due to non-radiative recombination. This in turn increases electron-hole pair generation rates and causes the steady state excited carrier population to grow. For a

fixed low bias input current, the voltage (and thus the electrical work) required to drive the current will decrease as the temperature of the LED increases. If the quantum efficiency does not change, the wall plug efficiency will increase as the voltage decreases. We have already shown that LED structures can be optimized to achieve high quantum efficiency at a target temperature, and thus we think it is possible to design a self-heating device for operation in ambient environment. We envision the package as looking much like a light bulb, where long thin wires are used to to inject current into an emitter in a vacuum so that conduction and convection are suppressed. This design work would probably require comprehensive three dimensional modeling of conductive, convective and radiative heat transfer away from the LED and packaging.

Experimental study of self-heating in LEDs for thermal pumping would also be interesting. Specifically, operating an LED at low bias in an evacuated chamber and showing an improvement in wall plug efficiency resulting from thermal isolation could act as a proof-of-concept motivating the design of compact and thermally insulating LED packaging for low-power applications.

5.1.3 Nanostructured LEDs for High Quantum Efficiency

Only a few simple design strategies for enhancing thermal pumping in LEDs were considered in Chapter 4. Nanostructure-related strategies for improving the quantum efficiency or even the feeding efficiency of an LED at a given temperature and electrical bias remain to be explored. These include the use of doped quantum wells or quantum dots in the active region to improve the chances of an electron and a hole finding one another for a given carrier concentration. Super-lattice structures made up of type-II heterojunctions have been shown to allow for generation of low-energy photons through non-local electron-hole recombination. This type of structure may allow for enhanced thermal pumping at room temperature since the radiation emitted from the device is close to being in thermal equilibrium with the environment, which increases the Carnot limit for the wall plug efficiency. Sentaurus is capable of modeling recombination and transport in these types of nanostructured devices, so

this pursuit seems like a logical next step in LED thermal pumping research.

Bibliography

[1] N.V. Zotova, N.D. Ilinskaya, S.A. Karandashev, B.A. Matveev, M.A. Remennyi, N.M. Stus, and A.A. Shlenskii. The flip-chip InGaAsSb/GaSb LEDs emitting at a wavelength of 1.94μm. *Semiconductors*, 40(3):356–361, 2006. 10, 44, 45, 74, 111

[2] A.L. Zakageim, N.D. Ilinskaya, S.A. Karandashev, B.A. Matveev, M.A. Remennyi, A.E. Cherniakov, and A.A. Shlenskii. Emission distribution in GaInAsSb/GaSb flip-chip diodes. *Semiconductors*, 43(5):662–667, 2009. 10, 44, 45, 67, 68

[3] Data Sheet for Ioffe LED, Ltd. Model LED21Sr. 10, 44, 46

[4] Stanford Research Systems, 1290-D Reamwood Avenue Sunnyvale, California, USA 94089. *SR570 Low-Noise Current Preamplifier*, 1997. 16, 93

[5] S. M. Sze. *Physics of Semiconductor Devices.* Wiley & Sons, Inc., New York, 1981. 17, 26, 30, 34, 88, 90, 97, 101, 112

[6] O. Heikkilä, J. Oksanen, and J. Tulkki. Ultimate limit and temperature dependency of light-emitting diode efficiency. *J. Appl. Phys.*, 105:093119, 2009. 18, 25, 33, 73, 109, 112, 113, 114

[7] E. Schubert. *Light-Emitting Diodes.* Cambridge University Press, Cambridge, 2006. 23, 24, 28, 29, 73, 113, 117

[8] S.-J. Bae et al. Fabrication and theoretical analysis of ga*n*-based vertical light-emitting diodes with SiO2 current blocking layer. *Semicond. Sci. Tech.*, 26:095008, 2011. 24

[9] M. Shatalov, J. Yang, Yu. Bilenko, M. Shur, and R. Gaska. High power III-nitride UV emitters. *Conference on Lasers and Electro-Optics/Laser Applications to Photonic Applications, OSA Technical Digest*, 2011. 24, 126

[10] C. G. Moe et al. Current-induced degradation of high performance deep ultraviolet light-emitting diodes. *Appl. Phys. Lett.*, 96:213512, 2010. 24

[11] W. Schmid and M. Scherer. Efficient light-emitting diodes with radial outcoupling taper at 970 and 630 nm emission wavelength. *Annual Report of the Optoelectronics Department, University of Ulm*, 2000. 24

[12] G. Yu. Sotnikova, G. A. Gavrilov, S. E. Aleksandrov, A. A. Kapralov, S. A. Karandashev, B. A. Matveev, and M. A. Remennyy. Low voltage CO2 gas sensor based on III-V mid-IR immersion lens diode optopairs: Where we are and how far we can go? *IEEE Sensors*, 10:225–234, 2010. 24

[13] Oskari Heikkila, Jani Oksanen, and Jukka Tulkki. The challenge of unity wall plug efficiency: The effects of internal heating on the efficiency of light-emitting diodes. *J. Appl. Phys.*, 107(3):033105, 2010. 25, 31, 33, 34, 73, 101, 109

[14] J. Tauc. The share of thermal energy taken from the surroundings in the electro-luminescent energy radiated from a *p-n* junction. *Czechoslovak Journal of Physics*, 7(3):275276, 1957. 25, 33

[15] M. Weinstein. Thermodynamic limitation on the converstion of heat into light. *JOSA*, 50(6):597–602, 1960. 25, 33

[16] S.-T. Yen and K.-C. Lee. Analysis of heterostructures for electroluminescent refrigeration and light-emitting without heat generation. *J. Appl. Phys.*, 107:054513, 2010. 25, 33, 117

[17] S. Yu, D. Ding, J. Wang, S. R. Johnson, and Y. Zhang. Electroluminescence refrigeration in semiconductors. In *Conference on Lasers and Electro-Optics/Quantum Electronics and Laser Science Conference and Photonic Applications Systems Technologies, OSA Technical Digest* , 2006. 25

[18] P. Han, J. Jin, Y. L. Zhou, X. Wang, Z. S. Ma, S. F. Ren, A. G. Mal'shukov, and K. A. Chao. Analysis of optothermionic refrigeration based on semiconductor heterojunction. *J. Appl. Phys.*, 99:074504, 2006. 25

[19] P. Han, J. Jin, Y. L. Zhou, H. B. Lu, and G. Z. Yang. Numerical designing of semiconductor structure for optothermionic refrigeration. *J. Appl. Phys.*, 101:014506, 2007. 25, 33

[20] J. Oksanen and J. Tulkki. Thermophotonic heat pump: a theoretical model and numerical simulations. *J. Appl. Phys.*, 107(9):093106093106, 2010. 25, 33

[21] J. Oksanen et al. Thermophotonic cooling: Effects of photon transport, emission saturation and reflection losses on thermophotonic cooling and status of the experimental work. Presented at SPIE Photonics West Conference, San Francisco, CA, January 2011. 25

[22] S. Tiwari. *Compound Semiconductor Device Physics.* Academic Press, Inc., San Diego, CA, 1992. 29, 117

[23] S. Watanabe, N. Yamada, M. Nagashima, Y. Ueki, C. Sasaki, Y. Yamada, T. Taguchi, K. Tadatomo, H. Okagawa, and H. Kudo. Internal quantum efficiency of highly-efficient $In_xGa_{1-x}N$-based near-ultraviolet light-emitting diodes. *Appl. Phys. Lett.*, 83(4):4906–4908, 2003. 32

[24] T. Baba, K. Inoshita, H. Tanaka, J. Yonekura, M. Ariga, A. Matsutani, T. Miyamoto, F. Koyama, and K. Iga. Strong enhancement of light extraction efficiency in GaInAsP 2-D-arranged microcolumns. *J. Lightwave Tech.*, 17(11):23113–23120, 1999. 32

[25] M. Boroditsky and E. Yablonovitch. Light-emitting diode extraction efficiency. *Proc. SPIE*, 119:3002, 1997. 32

[26] S. Pimputkar, J. S. Speck, S. P. DenBaars, and S. Nakamura. Prospects for LED lighting. *Nature Photonics*, 3:180–182, 2009. 32

[27] J. Wierer, A. David, and M. Megens. III-nitride photonic-crystal light-emitting diodes with high extraction efficiency. *Nature Photonics*, 3:163–169, 2009. 32

[28] Y. Narukawa, M. Sano, T. Sakamoto, T. Yamada, and T. Mukai. Successful fabrication of white light-emitting diodes by using extremely high external quantum efficiency blue chips. *Phys. Stat. Sol. A*, 205:1081–1085, 2008. 32

[29] K. Lehovec, C. A. Accardo, and E. Jamgochian. Injected light emission of silicon carbide crystals. *Physical Review*, 83(3):603, 1951. 33

[30] W. Bradley. Electronic cooling device and method for the fabrication thereof. U.S. Patent 2,898,743, August 1959. 33

[31] G. C. Dousmanis, C. W. Mueller, H. Nelson, and K. G. Petzinger. Evidence of refrigerating action by means of photon emission in semiconductor diodes. *Phys. Rev*, 133(1A):A316A318, 1964. 33

[32] P. Berdahl. Radiant refrigeration by semiconductor diodes. *J. Appl. Phys.*, 58(3):13691374, 1985. 33, 126

[33] K. P. Pipe. *Bipolar Thermoelectric Devices.* Ph.D. thesis, Massachusetts Institute of Technology, Department of Electrical Engineering and Computer Science, February 2004. 36, 52, 53

[34] P. Santhanam. Generalized drift-diffusion for microscopic thermoelectricity. Master's thesis, Massachusetts Institute of Technology, Department of Electrical Engineering and Computer Science, May 2009. 36, 41, 54

[35] A. Fischer, A. Allerman, M. Crawford, K. Bogart, S. Lee, R. Kaplar, W. Chow, S. Kurtz, K. Fullmer, and J. Figiel. Room-temperature direct current operation of 290 nm light-emitting diodes with milliwatt power levels. *Appl. Phys. Lett.*, 84(17):3594–3596, 2004. 37

[36] S.-H. Yen, B.-J. Chen, M.-L. Chen, Y.-K. Kuo, Y.-A. Chang, and H.-C. Kuo. Fabrication and simulation of ultraviolet AlGaInN light-emitting diodes. *Proc. SPIE*, January 2006. 38

[37] J. Stęszewski, A. Jakubowski, and M. Korwi*n*-Pawlowski. Comparison of 4H-SiC and 6H-SiC MOSFET I-V characteristics simulated with Silvaco ATLAS and Crosslight APSYS. *J. Telecom. Inform. Tech.*, 3:93–95, 2007. 38

[38] Synopsys. *Sentaurus Device User Guide*, d-2010.03 edition, March 2010. 38

[39] Mark Lundstrom. *Fundamentals of Carrier Transport.* Cambridge University Press, Cambridge, U.K., second edition, 2000. 38, 41, 54

[40] R. Stratton. Diffusion of hot and cold electrons in semiconductor barriers. *Physical Review Letters*, 126(6):2002–2014, 1962. 38, 41

[41] R. Stratton. Semiconductor current-flow equations (diffusion and degeneracy). *IEEE Trans. Elec Dev.*, 19(12):1288–1292, 1972. 40, 41

[42] Private communications with Professor Boris Matveev, principle investigator of the Mid-IR Diode Optopair Group (MIRDOG), regarding the LED21Sr. 44, 108

[43] F. Karouta, H. Mani, J. Bhan, F.J. Hua, and A. Joullie. Croissance par épitaxie en phase liquide et caractérisation d'alliages GaInAsSb à paramètre de maille accordé sur celui de GaSb. *Revue Phys. Appl.*, 22:1459–1467, 1987. 47

[44] M.C. Wu and C.C. Chen. Photoluminescence of highquality GaSb grown from ga and sbrich solutions by liquidphase epitaxy. *J. Appl. Phys.*, 72(9):4275–4280, 1993. 47, 111

[45] S. C. Jain, J. M. McGregor, and D. J. Roulston. Band-gap narrowing in novel III-V semiconductors. *J. Appl. Phys.*, 68(7):3747, 1990. 47, 67

[46] G. Stollwerck, O.V. Sulima, and A.W. Bett. Characterization and simulation of GaSb device-related properties. *IEEE Trans. Elec. Dev.*, 47(2):448–457, 2000. 47

[47] S. Anikeev, D. Donetsky, G. Belenky, S. Luryi, C.A. Wang, J. M. Borrego, and G. Nichols. Auger and radiative recombination coefficients in 0.55-eV InGaAsSb. *Appl. Phys. Letters*, 83(16):3317–3319, 2003. 47, 67, 73

[48] R.J. Kumar, J.M. Borrego, P.S. Dutta, R.J. Gutmann, C.A. Wang, and G. Nichols. Auger and radiative recombination coefficients in 0.55-eV InGaAsSb. *J. Appl. Phys.*, 97:023530, 2005. 47, 111, 112, 114

[49] V. Bhagwat, Y. Xiao, I. Bhat, P. Dutta, T. Refaat, M.N. Abedin, and V. Kumar. Analysis of leakage currents in mocvd grown GaInAsSb based photodetectors operating at 2 μm. *J. Elec. Mat.*, 35(8):1613–1617, 2006. 47

[50] K. P. Pipe, R. J. Ram, A. K. Goyal, and G. W. Turner. Electrical and thermal analysis of heat flow in λ=2.05μm GaInAsSb/AlGaAsSb lasers. *Conference on Lasers and Electro-Optics/Quantum Electronics and Laser Science Conference, Technical Digest*, pages 1825–1827, 2003. 47

[51] Hyung Jae Lee and John C. Woolley. Electron transport and conduction band structure of GaSb. *Canadian Journal of Physics*, 59(12):1844–1850, December 1981. 47

[52] J.P. Prineas, J. Yager, S. Seyedmohamadi, and J.T. Olesberg. Leakage mechanisms and potential performance of molecular-beam epitaxially grown GaInAsSb 2.4 μm photodiode detectors. *J. Appl. Phys.*, 103:104511, 2008. 47

[53] M. Levinshtein, S. Rumyantsev, and M. Shur. *Handbook on Semiconductor Parameters*, volume 2, pages 180–205. World Scientific, London, 1999. 47, 108

[54] M. Levinshtein, S. Rumyantsev, and M. Shur. *Handbook on Semiconductor Parameters*, volume 1, pages 125–146. World Scientific, London, 1996. 17

[55] W. Both, A. Bochkarev, A. Drakin, and B. Sverdlov. Thermal resistivity of quaternary solid solutions InGaSbAs and GaAlSbAs lattice-matched to GaSb. *Elec. Lett.*, 26(7):418–419, 1990. 17

[56] K. Kash, P. A. Wolff, and W. A. Bonner. Nonlinear optical studies of picosecond relaxation times of electrons in nGaAs and nGaSb. *Appl. Phys. Letters*, 43(2):173–175, 1983. 48

[57] T. Parodos et al. Effect of dislocations on VLWIR HgCdTe photodiodes. *J. Elec. Materials*, 36:1068–1076, 2007. 62

[58] S. Sridaran, A. Chavan, and P. S. Dutta. Fabrication and passivation of GaSb photodiodes. *J. Crystal Growth*, 310:1590–1594, 2008. 62, 63

[59] P.-Y. Emelie. *HgCdTe Auger-Suppressed Infrared Detectors Under Non-Equilibrium Operation.* Ph.D. thesis, University of Michigan, Department of Electrical Engineering, 2009. 62, 63

[60] J.-B. Wang, S. R. Johnson, D. Ding, S.-Q. Yu, and Y.-H. Zhang. Influence of photon recycling on semiconductor luminescence refrigeration. *J. Appl. Phys.*, 100(4):043502, 2006. 73

[61] Robert Karlicek. High-power led packaging. In *Conference on Lasers and Electro-Optics/Quantum Electronics and Laser Science and Photonic Applications Systems Technologies, OSA Technical Digest.* Optical Society of America, 2005. 74

[62] Hamamatsu Corp., Solid State Division, 1126-1 Ichino-cho, Hamamatsu City, 435-8558 Japan. *InGaAs PIN Photodiodes: G8423/G8373/G5853 series*, June 2009. 81, 94, 96

[63] Hamamatsu Corp., Solid State Division, 1126-1 Ichino-cho, Hamamatsu City, 435-8558 Japan. *Technical Information SD-12: Characteristics and Use of Infrared Detectors*, November 2004. 90, 95

[64] P .Werle, F. Slemr, K. Maurer, R. Kormann, R. Mücke, and B. Jänker. Near- and mid-infrared laser-optical sensors for gas analysis. *Optics and lasers in engineering*, 37(2-3):101114, 2002. 90

[65] Agilent Technologies, Inc. *Agilent 33210A 10 MHz Function/Arbitrary Waveform Generator User's Guide*, 2008. 90, 95

[66] Stanford Research Systems, 1290-D Reamwood Avenue Sunnyvale, California, USA 94089. *DS360 Ultra-low distortion function generator datasheet.* 95

[67] AMETEK Advanced Measurement Technology, Inc., 801 South Illinois Avenue Oak Ridge, TN USA 37831-2011. *Model 7280 Wide Bandwidth DSP Lock-in Amplifier Instruction Manual*, 2005. 96

[68] M. A. Afrailov, A. N. Baranov, A. P. Dmitriev, M. P. Mikhailova, Yu.-P. Smorchkova, I. N. Timchenko, V. V. Sherstnev, Yu. P. Yakovlev, and I. N. Yassievich. *Sov. Phys. Semicond.*, 24:876, 1990. 108

[69] M. P. Mikhailova and A. N. Titkov. Type II heterojunctions in the GaInAsSb/GaSb system. *Semiconductor Science and Technology*, 9:1279, 1994. 108, 110

[70] M. J. Cherng, G. B. Stringfellow, D. W. Kisker, A. K. Srivastava, and J. L. Zyskind. GaInAsSb metastable alloys grown by organometallic vapor phase epitaxy. *Appl. Phys. Lett.*, 48:"419–421", 1986. 108, 111

[71] Otfried Madelung. *Semiconductors - Basic Data.* Springer, 2nd revised ed. edition, April 1996. 108

[72] J. A. Robinson and S. E. Mohney. A low-resistance, thermally stable ohmic contact to n-GaSb. *J. Appl. Phys.*, 98:033703, 2005. 109

[73] S. Arafin, A. Bachmann, K. Kashani-Shirazi, S. Priyabadini, and M.-C. Amann. Low-resistive sulphur-treated ohmic contacts to n-type InAsSb. *IET Optoelectronics*, 3(6):259263, 2009. 109

[74] E. Mairiaux, L. Desplanque, X. Wallart, and M. Zaknoune. Improvement of ohmic contacts to $In_{.65}Ga_{.35}Sb$ using mo refractory metal and surface preparation for 6.3 angstrom heterojunction bipolar transistors. *J. Vac. Sci. Technol. B*, 28(1):17–20, 2010. 109

[75] Z. Yuan, A. Nainani, Y. Sun, J.-Y. Lin, P. Pianetta, and K. C. Saraswat. Schottky barrier height reduction for metal/n-GaSb contact by inserting tio2 interfacial layer with low tunneling resistance. *Appl. Phys. Lett.*, 98:172106, 2011. 109

[76] Y. K. Su, N. Y. Li, and F. S. Juang. The affect of annealing temperature on electrical properties of Pd/n-GaSb schottky contacts. *J. Appl. Phys.*, 68:646–648, 1990. 109

[77] R. Hultgren, R. L. Orr, P. D. Anderson, and K. K. Kelly. *Selected Values of Thermodynamic Properties of Metals and Alloys.* Wiley, 1963. 109

[78] T.B. Massalski. *Binary Alloy Phase Diagram*, volume 3. The Material Information Society, 1990. 109

[79] D. Ban et al. Optimized GaAs/AlGaAs light-emitting diodes and high efficiency wafer-fused optical up-conversion devices. *J. Appl. Phys.*, 96:5243–5248, 2004. 109

[80] F. M. Mohammedy and M. J. Deen. Growth and fabrication issues of GaSb-based detectors. *J. Mater. Sci.: Mater. Electron.*, 20:1039–1058, 2009. 109

[81] G. Benz and R. Conradt. Auger recombination in GaAs and GaSb. *Physical Review B*, 16(2):843, 1977. 110

[82] K. O'Brien, S. J. Sweeney, A. R. Adams, S. R. Jin, C. N. Ahmad, B. N. Murdin, A. Salhi, Y. Rouillard, and A. Joulli. Carrier recombination mechanisms in mid-infrared GaInAsSb quantum well lasers. *Phys. Stat. Sol. B*, 244(1):203–207, January 2007. 110, 111

[83] A. V. Dmitriev and M. Mocker. Recombination and ionization in narrow gap semiconductors. *Physics Reports*, 257(2):85–131, June 1995. 110, 113

[84] M. Krijn. Heterojunction band offsets and effective masses in III-V quaternary alloys. *Semiconductor Science and Technology*, 6:27, 1991. 110

[85] M. Tavakoli, L. Turicchia, and R. Sarpeshkar. An ultra-low-power pulse oximeter implemented with an energy-efcient transimpedance amplier. *IEEE Transactions on Biomedical Circuits and Systems*, 4(1):27–37, February 2010. 125